The Effect of Network Geometry on Electron Transport in a TiO_2 photoanode of a Dye-sensitized Solar Cell

by

SONIA SUSAN MATHEW

A Dissertation submitted to the Graduate Faculty in Engineering in Partial Fulfillment of the Requirements for the Degree of Doctor of Philosophy, The City University of New York

2013

This manuscript has been read and accepted for the Graduate Faculty in Engineering in satisfaction of the dissertation requirement for the degree of Doctor of Philosophy.

_____ _____

Date Prof. Ilona Kretzschmar

Chair of Examining Committee

_____ _____

Date Prof. Ardie Walser

Executive Officer

Prof. Alexander Couzis

Prof. James Gilchrist

Prof. Daniel Steingart

Prof. Raymond Tu

Supervisory Committee

THE CITY UNIVERSITY OF NEW YORK

Abstract

The Effect of Network Geometry on Electron Transport in a TiO_2 photoanode of a Dye-sensitized Solar Cell (DSSC).

by

Sonia S. Mathew

Advisor: Ilona Kretzschmar

The dye sensitized solar cell (DSSC) is a photoelectrochemical cell that has garnered considerable attention because of its high efficiencies and potentially low production costs. The technology is based on a layer of mesoscopic TiO_2 particles, which significantly increases the optical path of the incident light that is harvested by the surface-anchored sensitizer molecules, whilst keeping an efficient contact with the electrolytic solution. The solar cell configuration that first achieved a high efficiency (~7.5%) had a randomly connected network of titania nanoparticles, ruthenium polypyridyl complexes as the sensitizer, and an iodide/triiodide redox couple dissolved in an organic electrolyte.

While the disordered nanoparticle network has a high surface area which maximizes the photogenerated electron density, the nanostructure also has a large number of surface states. These surface states act as traps and are known to limit the transport of electrons within such electrodes thereby hindering progress in achieving higher efficiencies. The structural disorder at the contact between two crystalline nanoparticles leads to enhanced scattering of free electrons, thus reducing electron mobility. An interconnected photoanode architecture offers the potential for improved electron transport by reducing the degree of disorder.

This Thesis investigates the effect of the TiO_2 network geometry on electron movement within the DSSC. In this regard, inverse opal structures with hexagonally close-packed pores and macroscopic (~μm) order are synthesized and evaluated qualitatively and quantitatively (via FFT) with respect to their degree of interconnectedness. An inverse opal TiO_2 electrode possesses advantages that supplement those of current disordered electrodes: (a) high surface area for dye adhesion, (b) large area contact between the sensitizer and the electrolyte, which aids electron transfer reactions, and (c) scattering of incident radiation due to the inherent diffraction properties of the structures, which increases the path length.

The TiO_2 inverse opals are fabricated via self-assembly of colloidal particles and subsequent infiltration of the colloidal assembly with a TiO_2 precursor. Heat treatment at elevated temperatures (450 °C) leads to crystalline TiO_2 formation and removal of the templating colloids. Several methods of fabrication are evaluated to determine the best methods of fabrication for inverse opals of different pore sizes (0.5 μm to 10 μm). Optimum fabrication methods are determined for each particle size in the range studied.

The TiO_2 inverse opals (0.1 μm to 1 μm) are exposed to an aqueous electrolyte to evaluate their electrochemical behavior. The number of surface traps is found to scale with the surface area per unit volume of the inverse opal electrodes. Compared to the standard disordered nanoporous electrode, the inverse opals show better conductivity and are less prone to recombination. The TiO_2 inverse opals (0.1 μm to 1 μm) are also tested within a DSSC configuration, and illuminated with light from a compact fluorescent bulb to mimic lighting conditions ranging from indoor to outdoor conditions. The power output of the inverse opal electrodes is almost three times higher than the nanoparticle analog at low-light intensities, indicating the advantage of the interconnected nanostructure of the inverse opal electrodes under indoor light conditions. In contrast, the

disordered nanoporous electrode wins out in outdoor light conditions, providing evidence that inverse opal structured electrodes have their market in indoor applications.

Acknowledgements

I would like to express my gratitude to my advisor, Prof. Ilona Kretzschmar, for her guidance and support throughout my research work. Prof. Kretzschmar has been and will continue to be an invaluable asset to me. In addition to her guidance on the Thesis work, she has taught me several things about myself. She has taught me how to successfully develop an idea, how to persevere, and how to stay positive when research hits the characteristic snag. Over the course of this PhD, my life has been constantly changing. She was the mentor, who I needed her to be at each point. She was understanding and a gentle taskmaster, who helped this project to where it is today. She helped me grow as an individual, and as a mother, by making me push my limits. In short, she has been the perfect mentor to me.

I thank Prof. Alex Couzis, Prof. James Gilchrist, Prof. Dan Steingart and Prof. Raymond Tu, the members of my PhD committee, for providing the necessary feedback and guidance throughout my Thesis. I appreciate the generous guidance provided by Prof. Steingart and Dr. Joshua Galloway for understanding the electrochemical aspects of this project. Further, I would like to thank all of the professors, who believed in me as a graduate student. Having returned to academics after three years of work, I was unsure of my ability to do well. The fostering mentality of the professors in our department went a long way to restore confidence in my abilities.

I would like to thank PSC-CUNY (#69038-0038, -0039 & -0040) and the NSF IGERT program (#0221589) for early funding of this Thesis. Also, I thank CENSES (NSF #0833180), especially Diane Beckford and Danh Nguyen, for their encouragement and support. The latter part of this Thesis work was supported by the CCNY Energy Institute. I am thankful for their support because it was an opportunity to apply the concepts learned during this work to a completely different field.

The work environment within our lab group was enriched by my colleagues and friends. I thank my undergraduate research assistants: Stephen Ma and Marta Dulko, who were responsible for data collection while I was on maternity leave. Needless to say, without their hard work and input I would not have been able to complete this Thesis to my satisfaction. Further, I am thankful for my lab mates, Kevin, Amar, Jingqin, Hsin-yu, Bin, Zhengping, Roger, Sepideh, Naomi, Dane, Evgeyniya, Mamadou, and Chat for interesting conversations about research and life in general.

I would like to thank Dr. Mita Chattoraj for her guidance and encouragement. She was responsible for getting started on this path. I thank my parents, George and Leela Mathew, for their love, encouragement, and unflinching support. I also thank my in-laws, Thomas and Santha Kurian. for supporting my decision and encouraging me to achieve higher goals in life.

Finally, I dedicate this Thesis to three people without whose love, cooperation, and understanding, I would not be where I am today: my husband and son, Kiran and Aaron Thomas, and my sister, Sherina Mathew. Kiran and Sherina helped me shoulder my responsibility to Aaron, while working on this Thesis. I am truly blessed to have such people in my life.

Table of Contents

List of Figures

List of Tables

1 *Photovoltaics: the future of energy technology*

Global energy consumption has increased by 150 quadrillion Btus in the last twenty years, and is expected to continue an exponential rise for the foreseeable future.[1] According to a 2012 report by the International Energy Agency, the climate goal of limiting global warming to 2 °C is becoming more difficult with each passing year due to our dependence on fossil fuels.[2] Amidst such concerns, much interest has been devoted to the search for alternative energy sources.[3] The ideal alternative

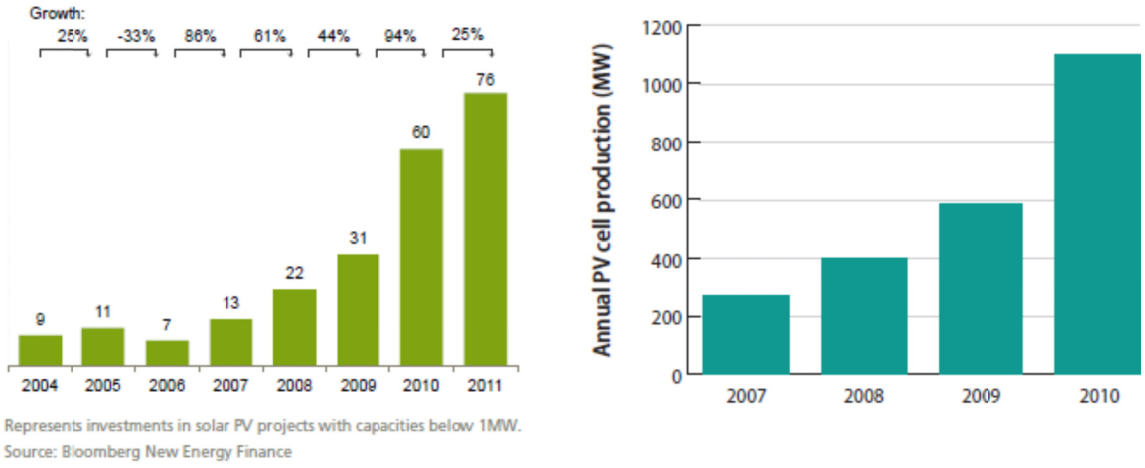

Figure 1.1 Annual investment in PV technologies worldwide (left)[6] and within the U.S. (right)[7]

energy source would be renewable and cheap to compete with current sources. There are several contenders that hope to replace fossil fuels: wind, solar, water, and geothermal energy. Despite being cheap and plentiful, these alternatives have remained at the periphery of the energy market mainly because of their inability to compete with current fossil-fuel based technology.

Of these alternative energy sources, solar energy has made significant inroads. Several advances in photovoltaic technology have helped to close the price gap. The photovoltaic (PV)

effect was first described in 1839 by Edmond Becquerel, a French physicist.[4] The development of the Czochralski process in the early 1950s was the next major step towards commercializing PV or solar cells.[5] Despite these advances, photovoltaic technology in the 1970s was still too expensive for most commercial purposes. However, the world oil crisis of the mid-1970s renewed interest in making PV technology more affordable. Most recently (2000s), the fluctuating price of oil coupled with production stagnation has reinvigorated the search for a cheap and reliable renewable resource. Accordingly, the federal government, industry, and research organizations have invested hundreds of millions of dollars in research, development, and production (Fig. 1.1).[6,7]

1.1 Photovoltaic Effect

The operating principle behind all solar cells is the photovoltaic effect. The light-to-energy conversion is done in two stages: (i) photogeneration of charge carriers (electrons and holes) in a semiconductor, and (ii) separation of the charge carriers to a conductive contact that will transmit the electricity. These two fundamental processes are still the basis of all inorganic solar cells today.

Photogeneration of charge carriers happens when photons of appropriate energy excite the electrons of a semiconductor. The absorption of photons with energy in excess of the semiconductor band gap energy drives the excitation of free electrons from the valence band into the conduction band. An electron-hole pair is created as a result. The presence of the positively charged hole initiates the movement of bonded electrons located at neighboring atoms. The recombination of the hole and the new electron creates a new hole. The two modes of charge carrier separation in a solar cell are (i) drift due to an electric field applied across the device and (ii) diffusion due to a gradient of electrochemical potential.[8] Thus, electrons flow freely through the material, producing an induced photocurrent, which can be used to power a load.

1.2 Solar Cells – Classical Systems

Modern solar cells were patented in 1946 by Ohl,[9] and demonstrated in 1954 by Chapin, Fuller, and Pearson at Bell Laboratories.[10] Their cell, which employed a single-crystal Si wafer for light absorption and a p-n junction for charge separation, operated with an efficiency of ~5%. Although the efficiency of solar cells has been improving steadily since 1954, the majority of today's commercial solar cells still resemble the Bell Laboratories cell.[8]

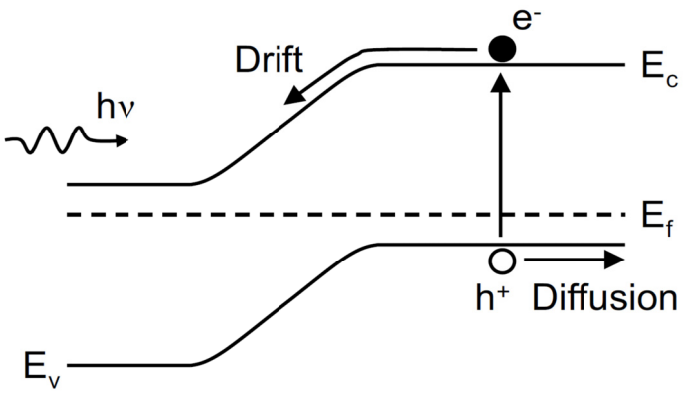

Figure 1.2 Principle of wafer-Si solar cell junction.

The photovoltaic response of a traditional solar cell is due to the effect of the junction between p-doped and n-doped silicon. When n-type silicon doped with phosphorus, is connected to p-type silicon typically doped with boron, a planar interface is formed between the two regions. Excess electrons in the n-region, driven by a difference in chemical potential, will diffuse across the interface, recombining with holes in the p-region. As a result, a potential difference is established between the two sides, opposing further diffusion of majority carriers. This region is called the depletion region, due to the depletion of mobile carriers. When a photon is absorbed within the depletion region, the generated electron-hole pair is separated by the force of the electric field (Fig.1.2). Once separated, the free carriers drift through the material and are collected at an electrode, thus yielding a photocurrent through an external path.

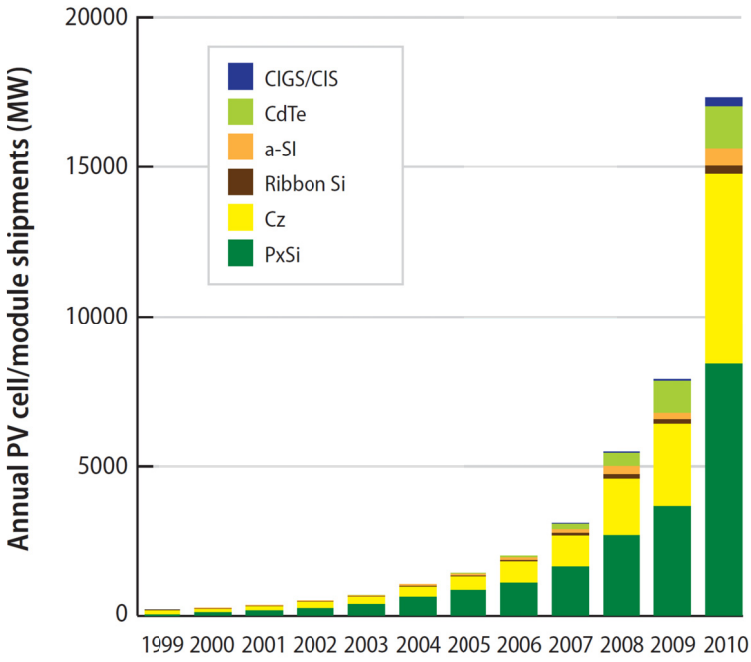

Figure 1.3 Global annual PV cell and module shipments by PV technology for 2011.

The first generation of solar cells consisted of large-area, high quality, and single p-n junction devices made of Si wafers. The directional and strong covalent bond in Si makes silicon wafers hard to process, thus making wafer-Si production costly and energy-intensive. A second generation of materials was developed to address the energy requirements and production costs of the first generation devices. The most successful second generation materials are cadmium telluride (CdTe), copper indium/gallium diselenide (CIGS), amorphous silicon (a-Si), and microcrystalline silicon (μc-Si). These materials are applied in a thin film to a supporting substrate, thus reducing material costs. A third generation of photovoltaic materials is based on multiple layers of p-n junction diodes. Each layer is designed to absorb a successively longer wavelength of light, thus absorbing more of the solar spectrum and increasing the amount of electrical energy produced. These devices aim to improve the efficiency of second generation cells, while maintaining the low production costs. These multi-junction cells, also known as tandem cells, consist of multiple thin films deposited on a supporting substrate produced using molecular beam epitaxy. A triple-junction cell, for example, stacks three p-n junctions made of $Ga_xIn_{1-x}As$ or $Ga_yIn_{1-y}P$, where x and y

represent the different compositions. Today, 90% of the solar cell market is still dominated by silicon. Figure 1.3 depicts the 2007 breakdown of market shares of different solar cell technologies. Polycrystalline silicon (poly-Si) is leading the way at 53%, followed by single-crystal silicon (sc-Si) at 33%. The thin-film technologies constitute only 11% of the market. Over the last ten years, the market share for poly-Si cells has expanded significantly, cutting into the market shares of a-Si as well as sc-Si. With shortage of Si material in recent years, the market shares of CdTe and CIGS are also expanding.[7]

Efficiency and cost are the two often cited parameters for terrestrial solar cells. Figure 1.4 shows the evolution of efficiency for various solar cell technologies over the last three decades. The efficiency of the sc-Si cell has reached 25%, while that of poly-Si cells is 20.3%. A multi-junction cell holds the record efficiency for all solar cell technologies at 44%. Besides wafer Si, several thin-film solar cell technologies have been commercialized, including silicon in either amorphous (a-Si) or

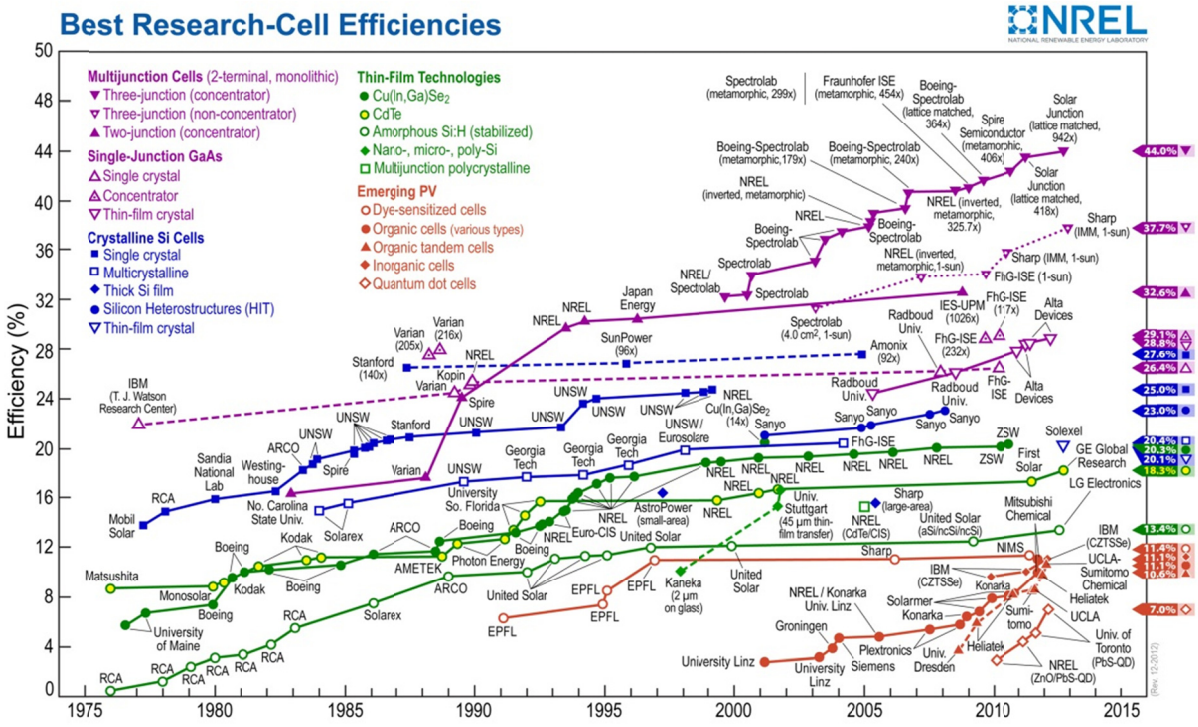

Figure 1.4 Evolution of best laboratory efficiency for different solar cell technologies.[11]

microcrystalline (μc-Si) form and metal chalcogenides (CdTe and $CuIn_xGa_{1-x}Se_2$/CIGS). Their record efficiencies range between 13% and 21%. While the progress in efficiencies of these laboratory-size solar cells has been remarkable, commercial-size cells and modules are typically one-half to two-thirds of these efficiencies.[11] Typically efficiency improvements are accompanied by additional costs, which suggest that the efficiency-cost ratio is a good figure of merit to determine the market success of a solar technology.

1.3 Dye-sensitized Solar Cell (DSSC)

The dye-sensitized solar cell is classified as an emerging PV technology. DSSCs are usually processed from appropriate solutions. Unlike traditional solar cells, their dominant mode of charge separation is diffusion due to an electrochemical gradient.

Dye-sensitized solar cells possess certain qualities that make them especially attractive. These solar cells are comparatively less labor and capital intensive. The photoanode is composed of titanium dioxide, which is a material that is easily sourced. TiO_2 is a cheap, readily available material that has a wide range of industrial applications. Additionally it is a non-toxic material that is advantageous in the present era of ecological and environmental consciousness. Cheap, natural dyes derived from fruits have been used to sensitize the TiO_2.[12] These solar cells are also amenable to roll-to-roll processing.[13] An advantage of the DSSC is that the photon absorption and charge separation processes are performed by two different materials, which provides a barrier toward electron recombination.

At 12%, DSSCs are among the most efficient of the emerging solar technologies available. Other thin-film technologies are typically around 8%, and traditional low-cost commercial silicon panels operate between 12% and 15% efficiency. This efficiency makes DSSCs attractive as a replacement for existing technologies in "low density" applications like rooftop solar collectors where the efficiency / cost ratio is important. They may not be as attractive for large-scale

deployments where expensive, more efficient cells are more viable. Unlike traditional solar cells, which suffer from low charge-carrier mobility in low-light situations, DSSCs are able to function in such ambient light conditions due to the significantly lower probability of electron recombination. As a result, they have been proposed for indoor use, collecting energy for small devices from the incandescent, fluorescent, and LED lights in the house.[14]

1.4 Objective of this work

Titanium dioxide (TiO_2 or titania) is the most commonly used semiconductor in a DSSC. The most widely tested configuration of a DSSC has a random, nanoporous network of titania nanoparticles. It serves as the photoanode, which transmits photo-excited electrons from the dye molecules to the external circuit. Electron transport is a limiting factor in the performance of these electrodes. The structural disorder at the contact between two TiO_2 nanoparticles leads to enhanced scattering of free electrons, thus reducing electron mobility. Instead, an ordered and strongly interconnected microstructure would promote electron transport, thus leading to higher efficiencies. Colloidal self-assembly is a straightforward method of preparing ordered, interconnected porous structures. In addition to lowering production costs, the method allows for a high degree of control over the TiO_2 microstructure. It offers control over the pore size and a high surface-to-volume ratio. The increased surface area enables better light absorption and more current resulting in a higher power output.

The aim of this thesis is to synthesize and characterize ordered porous inverse opal electrodes and compare their efficiency to the traditional randomly nanostructured electrode. The study sheds light on the charge transport mechanism that occurs within the inverse opal TiO_2 electrode when it is exposed to light. In addition, control of the inverse opal pore size enables us to study the effect of pore size and ordered structure on electron transport inside a DSSC. The following chapter, Chapter 2, broadly outlines the current state of research on DSSCs. Chapter 3 provides an

overview of the structural, electrochemical, and photoelectrochemical methods used for the characterization of electrodes and DSSCs, whereas Chapter 4 describes our approach to the synthesis of inverse opal electrodes with different pore sizes of comparable quality. The electrochemical characterization of the inverse opal TiO_2 electrodes is presented in Chapter 5, followed by results from photoelectrochemical experiments performed on DSSCs build with inverse opal electrodes in Chapter 6. Chapter 7 concludes with an overall summary of the Thesis work and an outlook section outlining future experimental directions.

2 A Review on the State-of-the-art of Dye-sensitized Solar Cells

Dye-sensitized solar cells (DSSCs) represent the current generation of solar cell research that focuses on affordability. These solar cells are synthesized from solutions and electron movement is initiated and guided by an electrochemical gradient.

2.1 Brief History of Dye-sensitized Solar Cells

The concept of dye-sensitized separation of electrons came as a result of years of improvement in photography. Like photography, photoelectrochemistry also relies on photo-induced charge separation at a liquid-solid interface. Following Vogel's work in 1873, the first panchromatic film able to render the image of a scene realistically into black and white was based on halide semiconductor grains and associated dyes. The first sensitization of a photoelectrode by Moser followed shortly thereafter, using a similar idea. Since the 1960s, it was clear that the operating mechanism in both photography and photoelectrochemistry was by injection of electrons from photo-excited dye molecules into the conduction band of the n-type semiconductor substrate. In subsequent years, the idea developed that the dye could function most efficiently if chemisorbed on the surface of a semiconductor. Next, photoelectrodes with high surface roughness were employed to maximize the contact between the dye and the semiconductor. Gradually, titanium dioxide became the semiconductor of choice since it had many advantages for sensitized photoelectrochemistry. It was a low cost, widely available, non-toxic and biocompatible material that was used in health care products and domestic applications such as paint pigmentation. The standard dye used at the time was tris (2,2'-bipyridyl-4,4'-carboxylate) ruthenium (II), where the

carboxylate group binds the dye molecule to the oxide substrate. The conversion efficiency of this semiconductor-dye combination was a synergy of structure, substrate roughness and morphology, dye photophysics, and electrolyte redox chemistry. Currently, the conversion efficiency for DSSCs is at 12 %.[15,16]

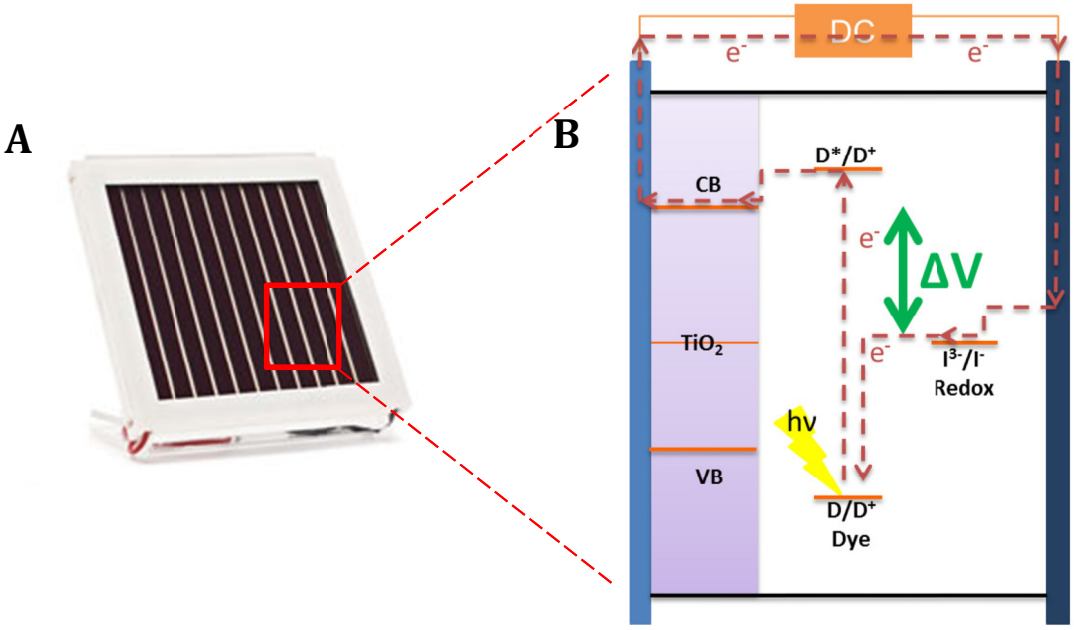

Figure 2.1 (A) Monolithically integrated dye solar cell module from Solaronix (MIMO 1010M11). (B) Electron Movement within a DSSC. ΔV is the theoretical maximum voltage that can be extracted.

2.2 Components of DSSCs

A dye-sensitized solar cell is a photoelectrochemical cell. It converts light energy to electrical work by precipitating electron transfer at the appropriate liquid-solid interfaces. The DSSC is composed of five main components: an electrically conductive glass substrate (TCO), a porous nanocrystalline semiconductor (TiO_2), a dye (D^*/D^+), an electrolyte ($I_3-/I-$), and a counter electrode. Light absorption is performed by a monolayer of dye chemisorbed on the semiconductor surface. The excited dye expends this photonic energy by injecting electrons into the conduction band (CB) of the TiO_2. Traditionally, the TiO_2 layer is a randomly connected network of

nanoparticles. Electron transport in this layer occurs by diffusion of the electrons to the conductive glass substrate (TCO) where it becomes part of the external circuit. The original state of the dye is restored by electron donation from the electrolyte, usually an organic solvent containing a redox system such as iodide (I^-) / triiodide (I_3^-). The process is called dye regeneration. The regeneration of the dye by iodide intercepts the recapture of the conduction band electron by the oxidized dye. The iodide is regenerated in turn by the reduction of triiodide at the counter electrode, the circuit being completed via electron migration through the external load. The theoretical maximum voltage (ΔV) that such a device could deliver corresponds to the difference between the redox (Nernst) potential of the mediator and the quasi-Fermi level of the electron in the semiconductor (Fig. 2.1B). The various parts of the DSSC work together to convert solar energy to electrical energy. The selection of each part has a bearing on the overall efficiency of the solar cell. The following sub-sections outline the prerequisite parameters of these components.

2.2.1 Titania precursors and synthesis methods

In the most common and efficient devices to-date, the TiO_2 photoanode is composed of 10-20 nm diameter nanocrystals that have been spread on a transparent, conducting oxide substrate and sintered to form a ~16 μm thick film.

The performance of a DSSC is intimately linked to the chemical composition, structure, and morphology of the titania (TiO_2) layer. TiO_2 is a wide-bandgap semiconductor (E_{bg} = 3.2 eV) that absorbs in the UV region of the light spectrum. Rutile, anatase, and brookite are the three most common crystalline polymorphs of titania. Rutile is the thermodynamically most stable polymorph. The anatase to rutile transformation occurs in the temperature range of 700-1000 °C depending on the crystallite size and impurity content. Several studies have examined the influence of film composition on electron transport. It has been found that electron transport in rutile TiO_2 layers is about an order of magnitude slower than transport in anatase. This difference in transport rate is

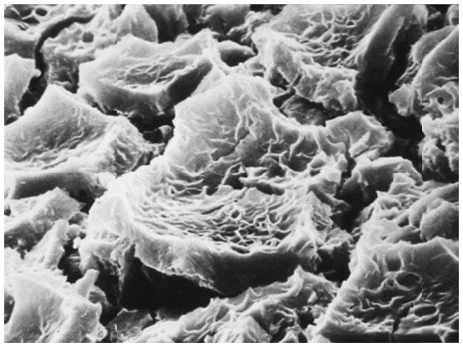

Figure 2.2 SEM image of the fractal TiO_2 film used in the first embodiment of the DSSC.[18]

attributed to a smaller number of interconnects between particles owing to the more open rod-like morphology of the rutile layers.[17]

TiO_2 films can be produced by various techniques such as sol-gel, chemical vapor deposition (CVD), physical vapor deposition (PVD), or electrochemical anodization of Ti foils. The first embodiment of the dye-sensitized solar cell employed a TiO_2 film prepared by a sol-gel method (Fig. 2.2).[18] After much optimization, the present TiO_2 layer is the result of a hydrothermal technique,[19] that produces a much more reproducible and controlled porous, high-surface texture. The synthesis involves the hydrolysis of a titanium alkoxide precursor followed by peptization in acid or alkaline water (low water/Ti ratio) to produce a sol.

Hydrolysis: $(RO_3)—Ti—O—R + H_2O \rightarrow (RO_3)—Ti—O—H + R—OH$

Condensation: $2(RO_3)—Ti—O—H \rightarrow (RO_3)—Ti—O—Ti—(OR)_3 + H_2O$

The sol is subjected to hydrothermal Ostwald ripening in an autoclave. The resulting TiO_2 particles consist of anatase or a mixture of anatase and rutile, depending on the reaction conditions.

In a randomly connected network of titania nanoparticles, the average pore size is dependent on the average size of the crystalline aggregates that are formed during peptization. The pore size distribution can be altered by adding various amounts of binder or by varying the sintering temperature and time, thus promoting pore coarsening. Controlling the pore size distribution ensures a good diffusion of the electrolyte and increases the efficiency of the cell. If the pores are too small (≤4nm), a degradation in the performance of the solar cell is observed. By controlling the density and the surface area of the nanocrystalline film, one also controls the amount of dye that is

adsorbed within the electrode. This quantity is directly linked to the electron injection and the current that is produced by the corresponding solar cell. The current can be further enhanced by treating the TiO_2 electrode with $TiCl_4$, which results in inter-particle neck growth and facilitates the electron percolation through the TiO_2 backbone.

2.2.2 Dye Addition

The dye plays the role of light absorber. The ideal dye of choice for converting standard global AM 1.5 (defined as the solar irradiance incident at angle 48.7° relative to the normal to the earth's surface) sunlight to electricity should absorb all light below a threshold wavelength of about 920 nm. In addition, the dye must also carry functional groups such as carboxylate or phosphonate to be able to bind to the semiconductor oxide surface. Upon excitation the dye should inject electrons into the solid with a quantum yield of unity. The energy level of the dye's excited state should be well matched to the lower bound of the conduction band of the oxide to minimize energetic losses during the electron transfer reaction. The dye's redox potential should be sufficiently positive that it can be regenerated via electron donation from the redox electrolyte. Finally, the dye should be stable enough to withstand 10^8 turnover cycles corresponding to about 20 years of exposure to natural light.[18]

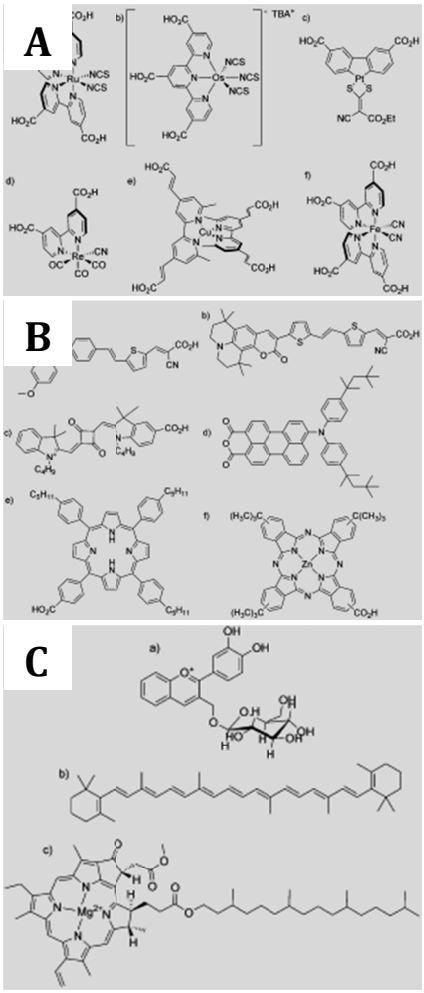

Figure 2.3 (A) Metal-containing complexes. (B) Organic dyes. (C) Natural dyes.

Dye compounds investigated for DSSC applications can be divided into three major groups: metal containing complexes,[20] organic dyes,[21] and natural compounds (see Fig. 2.3 for examples).[22] Mononuclear and polynuclear transition-metal

ions (such as Ru^{II}, Os^{II}, Pt^{II}, Re^{I}, Cu^{I}, or Fe^{II})[23-29] coupled with different anchoring ligands and different chromophoric groups have been widely studied as photosensitizers. However, the most used dyes by far in DSSCs are ruthenium-based complexes.

Organic dyes offer several advantages relative to their metal-containing analogues such as higher molar extinction coefficients and a large variety of chromophoric groups. Porphyrins,[30] phthalocyanines,[31] perylenes,[32] squaraines,[33] conjugated donor-acceptor moieties,[34] etc. have been explored with varying success. Although the efficiencies obtained with devices prepared with organic dyes are still lower than ruthenium-based DSSCs, recent publications have reported efficiencies of up to 10% with organic photosensitizers.[35] The main unfavorable characteristics of metal-free dyes are (i) the narrow absorption bands (phthalocyanines), which results in poorer sunlight harvesting, (ii) the tendency to form aggregates (perylenes), which prevents electron injection into the TiO_2 conduction band, and (iii) a lower stability relative to metal complexes (squaraines).

Natural photosensitizers are pigments extracted from plants, flowers, and fruits that have been used mainly for educational purposes as a fast, low-cost, and environmentally friendly source for the preparation of DSSCs.[12,22,36] The most studied dyes are anthocyanins contained in blueberries and cranberries, but the overall efficiency of this kind of dye is generally much lower than that of organic or metal complex sensitizers.

2.2.3 Electrolyte Choice

The function of the electrolyte is to regenerate the oxidized dye and to transport the positive charges to the counter-electrode. The redox potential of the ideal electrolyte should be more negative than the upper bound of the oxidized dye, so that dye regeneration is thermodynamically favorable. The electrolyte must have a high conductivity to permit fast electron transfer from the counter to the working electrode. For the same reason, the ionic species must also have a high

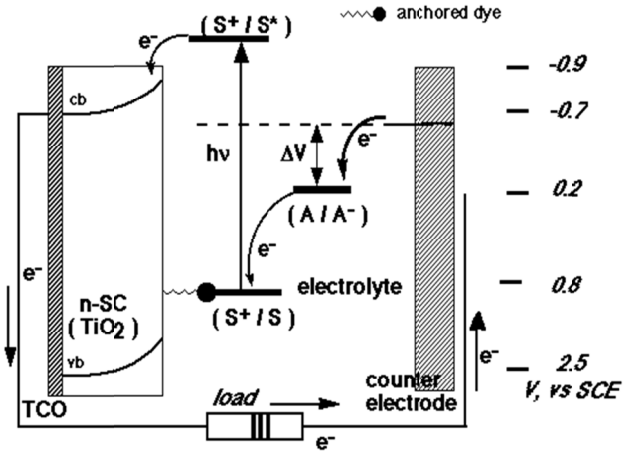

Figure 2.4 Voltage mismatch with I^-/I_3^-

diffusion coefficient. The electrolyte should also be thermally, optically, chemically, and electrochemically stable to avoid dye degradation or desorption from the metal oxide surface.

The most widely used redox system for DSSCs based on the ruthenium complex sensitization is the iodide (I^-) / triiodide (I_3^-) couple dissolved in an organic electrolyte or an ionic liquid. Although this combination has the advantage to provide efficient, highly reproducible and stable cell performance, it does suffer from a mismatch between the redox level of the I^-/I_3^- (~0.15 V vs. SCE) and that of the ground state of the N3 dye (cis-[Ru(4,4'-COOH)$_2$-2,2'bipyridine(NCS)$_2$], 0.85 V vs. SCE). As a consequence, the regeneration of the dye consumes about 0.7 eV. Referring to Fig. 2.4, it is obvious that the ΔV of the cell increases as the redox potential of the electrolyte becomes more positive. Since cell efficiency is directly proportional to ΔV, this energy mismatch constitutes the main loss factor in the operation of the DSSC. The dye regeneration reaction is further complicated by the fact that the conversion of I^- to I_3^- involves the transfer of two electrons. Hence, a large driving force is necessary to carry out the primary oxidation step from I^- to atomic iodine.

The use of a liquid electrolyte is a major disadvantage of the DSSC design due to stability problems. At low temperatures the electrolyte can freeze, ending power production and potentially leading to physical damage. Higher temperatures cause the liquid to expand, making sealing of the panels a serious problem. Another major drawback is the electrolyte solution, which contains volatile organic solvents that must be carefully sealed in. This, along with the fact that the solvents

permeate plastics, has precluded large-scale outdoor application and integration into flexible structures.[37] Chemical corrosive reactions between iodide and various metals is another common problem of the I^-/I_3^- couple, especially when trying to make modules, where metallic collector stripes are mandatory to collect the electrons generated by the cells.

Replacing the liquid electrolyte with a solid has been a major ongoing field of research. Recent experiments using solidified melted salts have shown some promise, but currently suffer from higher degradation during continued operation, and are also not flexible.[38]

Room temperature ionic liquids are attractive candidates as nonvolatile solvents for electrolytes, too. They are formed from aromatic or non-aromatic cations such as imidazolium, pyridinium or quarternary ammonium ions and are also used as source for iodide.[39] Ionic liquids possess good chemical and thermal stability, very low vapor pressure, non-flammability, high ionic conductivity, and wide electrochemical windows, which are useful properties for long-lived electrochemical devices. However, their high viscosity usually limits the transport of the redox shuttle components, which occurs by diffusion, and dye regeneration is therefore not as good as for organic solvent based electrolytes.

Quasi-solid-state electrolytes are gel-based materials with dispersed amounts of liquid electrolyte.[40] This type of electrolyte has the cohesive property of a solid electrolyte and the ion diffusion characteristics of a liquid electrolyte. Quasi-solid-state electrolytes are prepared by physical or chemical polymerization of a gel, inorganic material, or monomer that incorporates a large amount of liquid electrolytes.

Solid-state electrolytes can be divided into either hole-transport materials (HTM) or redox couple containing solid electrolytes. The first group requires a layer of an organic or inorganic large band gap HTM to be deposited from solution or by vacuum deposition. Inorganic HTMs such

as CuI, CuBr, or CuSCN have been used in DSSCs but show low stability. On the other hand, one of the most used organic HTMs is spiro-OMeTAD (2,2',7,7'-tetrakis-[N,N-di-*p*-methoxyphenylamine] 9,9'-spirobifluorene). The performance of DSSCs that use solid electrolytes is reduced because of the low hole mobility, increased charge recombination between the semiconductor and the HTM, and low interfacial contact surface between the dye molecules and the solid electrolyte, which results from incomplete percolation of electrolyte into the pores of the nanoporous electrodes. Redox-containing solid electrolytes incorporate a redox couple, usually I^-/I_3^-.

2.2.4 Transparent Conductive Substrates as Electrodes

Conventional DSSCs are based on rigid substrates such as glass with a conductive FTO (fluorine-doped tin oxide) layer. The conductive glass is an ideal substrate because of its transparency, which allows the light to excite the sensitized semiconductor. Since the titania layer needs to be annealed at high temperatures (~400 – 450 °C), the conductive layer must be able to withstand these conditions while maintaining its optical transparency. An FTO glass is also used as the counter electrode. Such electrodes are known to be a poor choice for efficient reduction of triiodide. To reduce the overvoltage losses, a very fine Pt-layer (or islands of Pt) is deposited onto the conducting glass electrode. This ensures high exchange current densities at the counter-electrode and thus the processes at the counter electrode do not become rate-limiting in the energy harvesting process.[41]

Current research is aimed toward developing flexible substrates. Substrates based on organic polymers offer flexibility and can be used in roll-to-roll printing techniques for mass production of organic electronics. Roll-to-roll printing represents a low cost method of manufacturing, which would go a long way to establishing DSSC solar cells in mainstream energy production.[16,18]

2.3 Electron Transfer Dynamics

As mentioned before, the heart of a DSSC is a semiconductor (SC) photoanode sensitized by a dye (D). Upon light absorption, the excited dye (D*) readily injects an electron into the conduction band of the semiconductor. Charge injection has been found to occur in the femtosecond (fs) time frame for numerous efficient systems, thus competing effectively against deactivation of the excited dye molecule. The electron back transfer from the conduction band to the dye cation takes place in the micro-to millisecond range. In the presence of a redox mediator (M), this interfacial charge recombination competes kinetically with the reaction of the oxidized dye. Charge transport by the electrolyte in the pores of the semiconductor film to the counter electrode and that of injected electrons within the nanocrystalline film to the back contact should be fast enough to compete efficiently with the electron recapture reaction. Table 2.1 summarizes the characteristic timescales of the electron transfer dynamics within a typical DSSC.

Table 2.1 Timescale of Electron Transfer Process within the DSSC.

Electron Transfer Process		**Timescale (s)**
Excitation	D |SC + hν → D*|SC	Femtosecond (10^{-15})
Injection	D*|SC → D^+|SC + e_{cb}^-(SC)	Femtosecond (10^{-15})
Relaxation	D*|SC → D|SC	Picosecond (10^{-12})
Dye Regeneration	D^+|SC + M → D|SC + M^+	Nanosecond (10^{-9})
Recombination	D^+|SC + e_{cb}^-(SC) → D|SC	Micro (10^{-6})to Millisecond (10^{-3})
Electron Recapture	M^+ + e_{cb}^- (SC) → M	Micro (10^{-6})to Millisecond (10^{-3})

Electron transport in DSSCs involves a trap-limited diffusion (random-walk) process. The generation, transport, and collection of electrons are usually modeled using the 1-D continuity equation, Eq. 2.1:

$$\frac{\partial n\,(x,t)}{\partial x} = \propto I_o e^{-\propto x} + D_n \frac{\partial^2 n(x,t)}{\partial x^2} - k_n[n(x,t) - n_o] \qquad \textit{Eq. 2.1}$$

with the boundary conditions:, (i) $n(0) = n_o e^{\frac{qU}{k_B T}}$ and (ii) $\frac{dn(d)}{dx} = 0$. Here, *n(x,t)* is the density of electrons in the oxide, n_o is the equilibrium (dark) electron concentration, α is the absorption coefficient of the dye-sensitized medium, I_o is the incident photon flux corrected for reflection losses. D_n is the diffusion coefficient of electrons and k_n is the first-order rate constant for back reaction of electrons with the oxidized dye. The lifetime of electrons, τ_n, is given by the reciprocal of k_n. The variables q, U, k_B, and T represent the elementary charge, voltage, Boltzmann constant, and temperature, respectively. The competition between collection and back reaction of electrons can be expressed in terms of the electron diffusion length, L_n, as shown in Eq. 2.2

$$L_n = \sqrt{D_n \tau_n} \qquad \textit{Eq. 2.2}$$

Efficient electron collection is obtained only if the electron diffusion length exceeds the film thickness.[42]

2.3.1 Charge-carrier percolation and collection

When the dye-sensitized solar cell was first introduced, the highly efficient charge transport through the nanocrystalline TiO_2 layer was puzzling. The mesoporous electrodes were different because (i) the inherent conductivity of the film was very low, (ii) the small size of the nanocrystalline particles did not support a built-in electrical field and (iii) the electrolyte penetrated the porous film all the way to the back-contact making the semiconductor/electrolyte interface essentially three-dimensional. Since then, several interpretations based on the Montrol–Scher model for random displacement of charge carriers in disordered solids[43] have been advanced to explain the highly efficient electron transport. For example, the effective electron diffusion coefficient has been found to depend on a number of factors such as trap filling and space charge compensation by ionic motion in the electrolyte. Pulsed laser-induced current transient measurements by Nakade et al.[44] revealed that dye adsorption onto a nanoporous TiO_2 electrode

increases the electron diffusion coefficient compared with a bare surface, due to the decreased number of free surface trap sites.

The migration of electrons within the TiO_2 conduction band to the current collector involves charge percolation over the nanoparticle network.[45] Electrons travel randomly through the network, hopping from particle to particle until they reach the collecting electrode or recombine with either oxidized species in the electrolyte or the oxidized dye molecules. If the particle network is not sufficiently cross-linked, it is plausible that electrons may wander through the porous structure for an extended period of time. Thus, an important parameter in percolation theory is the critical particle concentration, p_c. Below this concentration of particles, there is insufficient material present to form a continuous cluster that spans a sample from one end to the other, and macroscopic transport stops completely. Near p_c many physical properties, X (e.g., X may signify a diffusion coefficient, a heat transport coefficient, or a tensile strength) exhibit a power-law dependence on the difference between a concentration p and the critical particle concentration, p_c (Eq. 2.3):

$$X \propto |p - p_c|^{\gamma} = |P - P_c|^{\gamma} \qquad \textit{Eq. 2.3}$$

where, p_c is the critical particle concentration (or percolation threshold) and γ is a nonzero constant that can have either a positive or a negative value. The respective concentrations p and p_c are related to film porosity, P, and critical porosity, P_c. by the relations given in Eq. 2.4a and 2.4b:[46]

$$P = 1 - p \qquad \textit{Eq. 2.4a}$$

$$P_c = 1 - p_c \qquad \textit{Eq. 2.4b}$$

2.3.2 Back reaction of injected electrons

There are two loss mechanisms that compete with electron collection: (1) recapture of the electrons by the oxidized dye, and (2) reduction of the tri-iodide ions in the electrolyte present within the mesoporous network ($I_3^- + 2e_{cb}^- \rightarrow 3I^-$). The latter reaction can be directly followed by measuring the dark current of the dye-loaded film under forward bias (see Chapter 3 from more details). It is commonly assumed that electron transfer via the FTO substrate is negligible since the I_3^-/I^- exchange current density is very small. Hence, electron loss via the FTO is neglected under short-circuit conditions because the Fermi level in the FTO is close to the redox Fermi level. However, the Fermi level in the TiO_2 electrode under illumination rises rapidly with distance from the substrate. As a result, the driving force for the back reaction from the TiO_2 electrode to the electrolyte is much greater in the bulk of the sensitized layer than close to the FTO substrate. In contrast, the driving force for electron loss to the electrolyte under open circuit illumination conditions is about 0.7 eV higher. Thus, the back reaction with the electrolyte is no longer negligible, and the flux of electrons across the TiO_2-FTO interface is balanced by the flux of electrons across the FTO-electrolyte interface.

The contact between the FTO substrate, the TiO_2 electrode, and the electrolyte is significant because it must allow electrons to be extracted from the TiO_2, but prevent the transfer of electrons to the electrolyte. This three phase contact becomes especially important if the I^-/I_3^- redox couple is replaced by a one-electron couple.[47] In such a system, electrons are lost by back reaction both from the FTO substrate and from the TiO_2 electrode. In such cells, a blocking layer of TiO_2 is deposited on the substrate to eliminate one of the paths of electron recombination.

2.3.3 DSSCs Working in Indoor Lighting Conditions

A major advantage of DSSCs is that peak solar efficiency remains relatively unchanged in low-light conditions such as diffuse sunlight or indoor lighting. Due to their favorable electrochemical kinetics, DSSCs do not share the same cutoff point as other solar cells in terms of charge carrier mobility and recombination. Figure 2.5 shows the area-normalized rates at the maximum power point. The graph emphasizes the point that in its most efficient configuration, the DSSC has comparatively little kinetic redundancy, i.e., competing electron transfer reactions have sufficiently separated timelines.[48]

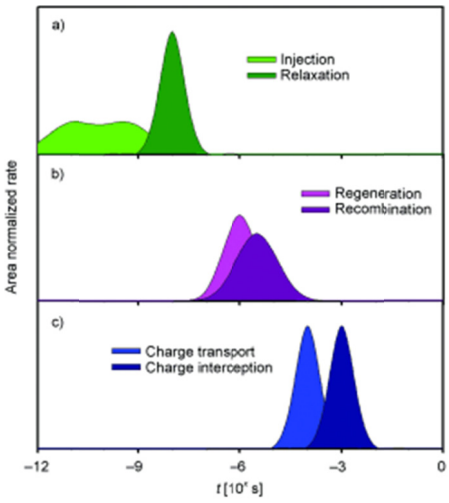

Figure 2.5 Area normalized rates for charge dynamics in direct kinetic competition at the maximum power point.[48]

2.4 Influence of Network Geometry

The large-scale structure, or network geometry, of the TiO_2 film is defined by how the particles are arranged in a network. The earliest photoelectrochemical cells had a flat smooth layer of semiconductor material. Drawing from the experiences of silicon photovoltaics, the rationale was that a rough surface would enhance recombination of photogenerated electrons. However, the efficiency of these initial cell configurations was too low to be used in practical applications. Studies showed that the light harvesting capacity of a dye monolayer on the surface of a flat oxide

film had the fundamental problem of the limited light-capture cross-section (cm^2/mol), which is related to the molar extinction coefficient ε by Eq. 2.5:

$$\sigma = \frac{\varepsilon * 1000}{N_A} \qquad \textit{Eq 2.5}$$

Typical ε values for dyes lie between 10^4 and $5*10^5$ M^{-1} cm^{-1} yielding light-capture cross-section values between 0.0016 and 0.08 nm^2. By comparison, the dye molecule occupies a much larger surface of the supporting oxide, e.g., about 1-2 nm^2. Hence, at most a few percent of the incident light can be absorbed. By introducing high surface area films consisting of nanocrystalline oxide particles, where the real surface area is 100-1000 times larger than the apparent one, the problem of light absorption is solved. This increase in available area allows for the capture of the incoming photons efficiently despite the fact that the oxide is only covered by a monolayer of dye. When light penetrates the dye-covered oxide "sponge", it crosses hundreds of adsorbed dye monolayers. Thereby, photons with energy close to the absorption maximum of the dye are completely absorbed.

Despite the adequate performance of nanoparticle films in conventional DSSCs, this photoanode geometry has several disadvantages such as low porosity, tedious particle synthesis, high surface trap density, and the extraordinarily small apparent diffusion coefficient, D_n. In response, research has been directed towards synthesizing structures with a higher degree of order than the random assembly of nanoparticles. A desirable morphology for the films would have mesoporous channels or nanorods aligned in parallel to each other and vertically with respect to the TCO glass current collector. This geometry would facilitate charge diffusion in the pores and the mesoporous film, give easier access to the film surface, avoid grain boundaries, and allow the junction to be formed under better control. One approach to fabricate such oxide structures is based on surfactant template-assisted preparation of TiO_2 nanotubes as described in a paper by Adachi et al.[49]

However, such 1D nanostructures have a lower surface area compared to the mesoporous analog, resulting in lower photocurrent and efficiency. Very recently, a simple approach to prepare oriented nanobrushes of TiO_2 on titanium supports has been published.[50] The work of Alivisatos and coworkers[51] on hybrid solar cells consisting of blends of CdSe nanoparticles with polythiophene has confirmed the superior photovoltaic performance of nanorod films when compared to random networks of spherical particles.

Three-dimensionally ordered macroporous (3DOM) electrode structures, also known as "inverse opals", studied in this Thesis combine the advantage of higher interfacial area with the connectivity of the 1D nanostructured arrays. The thin shell of the inverse opal structures plays a similar role as the 1D nanostructures in providing fast electron transport paths, while the high degree of porosity allows the redox pairs to diffuse unimpeded.

2.5 Chapter Summary

The DSSC has four components that work hand-in-hand – a porous semiconductor, a dye, an electrolyte, and a counter electrode. The dye, which is adsorbed onto the semiconductor, absorbs photons from solar irradiation and starts the electron movement within the cell. These photogenerated electrons diffuse through the porous semiconductor and make their way to the external circuit. The circuit is completed by the counter electrode and the electrolyte. The electrons from the external circuit collect at the counter electrode and reduce the redox couple presents in the electrolyte. The choice of these individual components plays a role in the overall energy conversion efficiency of the DSSC. In the most efficient cell, the Fermi level of each component matches up in a way that the electron movement is thermodynamically favored.

The most efficient configuration of the DSSC operates at 12% efficiency (AM 1.5) and uses the I^-/I_3^- redox pair dissolved in an organic solvent. The notoriously slow kinetics of heterogeneous electron transfer of the I^-/I_3^- redox pair is partly responsible for this high efficiency, because it

enhances charge separation by separating the timescales of electron recombination and dye regeneration. However, the organic electrolyte has proven to be a roadblock when it comes to commercialization of DSSCs. Iodide has a tendency to degrade the silver contacts, which serve as current collectors, and acetonitrile is too volatile and toxic leading to sealing and environmental problems. To circumvent these issues, current research is geared toward replacing the electrolyte with more viscous analogs. In light of this trend, the mesoporous nature of the TiO_2 electrode is problematic since it hinders the diffusion of ions. In addition to slower ionic diffusion, incomplete wetting of the viscous electrolytes to the TiO_2 electrode is a cause for diminished performance. Replacing the mesoporous electrode with an inverse opal electrode could be the key to improving both ionic diffusion and electrolyte wettability, since inverse opals have large, ordered, and interconnected pores.

A DSSC with a mesoporous electrode has a large number of traps. These traps can aid or hinder electron transport depending on the surrounding electrolyte. Electrolyte alternatives tend to have a larger size and quicker kinetics, which combined with the large number of traps, have delivered lower efficiencies. With inverse opals, we can control the number of surface traps since their surface area is controlled by the size of the template particles used during synthesis. The market niche for immediate DSSC commercialization is indoor applications. A mesoporous electrode with many traps that would remain empty at low illumination would be adversely affected when used indoors. With this reasoning in mind, the following chapters will describe general optical and electrochemical characterization methods (Chapter 3), and the synthesis (Chapter 4), characterization (Chapter 5) and use (Chapter 6) of inverse opal TiO_2 electrodes

.

3 Structural, Electrochemical, and Photoelectrochemical Characterization

This chapter introduces the structural, electrochemical, and photoelectrochemical characterization methods used throughout this Thesis work and their relevant theoretical background.

3.1 Structural Characterization of TiO_2 Electrode

The structural characterization of the titania layer is important as it determines the electrodes structural quality, i.e., stability, and enables the interpretation and comparison of electrochemical data in electrodes of various pore sizes. Parameters such as porosity, crystalline structure, and internal structure are some of the structural characteristics needed for interpretation of electrode resistance, capacitance, and charge density.

3.1.1 Microscopic Analysis

Optical Microscopy (OM) and Scanning Electron Microscopy (SEM) are the two chosen methods of large-scale structural characterization. Since regularity of the pores is a goal of the synthesis, OM and SEM are employed to discover defects on the surface of the structure and stacking faults when cross sections are viewed.

3.1.2 Fast Fourier Transform (FFT)

The Fourier Transform is an image processing tool that is used to decompose an image into its sine and cosine components. It transforms an image from the spatial domain to the frequency domain. FFT is the sampled Fourier Transform and therefore does not contain all frequencies

forming an image. Instead, only a set of samples that is large enough to fully describe the spatial domain image is considered. The FFT is defined by equation 3.1:

$$X_k = \sum_{n=0}^{N-1} x_n e^{-i2\pi k \frac{n}{N}} \qquad \textit{Eq. 3.1}$$

where x_n is the image in the spatial domain and the exponential term is the basis function corresponding to each point X_k in the Fourier space. The FFT algorithm evaluates this definition N $logN$ times.

The Fourier Transform is especially useful to access the geometric characteristics of a spatial domain image, e.g., the periodicity of ordered structures such as inverse opals. The advantage of the FFT analysis method is that it is a cost-effective way to quantify the crystallinity of an ordered structure from an SEM or optical micrograph in the absence of other tools such as XRD or spectroscopy. The analysis of reciprocal space compresses the information of real space images by looking at the spatial periodicities. As a result, it gives quantitative information on domain distribution, size, and orientation as well as defect density and distribution, all of which are often difficult to judge accurately from SEM images. One caveat of Fourier analysis performed on 2D images is that it does not include information about the entire 3D structure of the sample, as could be obtained by conventional diffraction methods.[52]

3.2 Characterization of Electron Transport in TiO_2 Electrode

The electronic transport properties of nanostructured electrodes vary strongly depending on the individual properties of the nanoparticles, the extent of contacting or electronic coupling between the particles, and the overall geometrical configuration of the assembly. When such electrodes are permeated with a conductive phase, i.e., an electrolyte, the ability to accumulate a large number of injected electron charges in the solid matrix is achieved. Under these conditions,

the electron Fermi level, E_{Fn}, within the semiconductor network can be controlled by variation of the electron density through photoinjection or a potentiostat.

In addition, in nanostructured semiconductors the large ratio of surface-to-volume usually produces a large amount of surface states in the bandgap. Therefore the influence of traps on the transport must be considered. The simplest approach to take trapping into account is the classical multiple trapping (MT) framework.[53] In this approach transport through extended states is slowed down by trapping-detrapping events, while direct hopping between localized states is neglected. The mobility decreases rapidly below a certain value of energy defining the transport states, so that the motion of a bound electron is limited by the rate of thermal excitations to $E > E_c$.

Detailed information on the physical parameters related to transport in DSSCs has been obtained using small perturbation techniques at a fixed steady state such as electrochemical impedance spectroscopy (EIS). In addition, large perturbation methods such as cyclic voltammetry (CV) and choronoamperometry (CA) help to characterize surface trap densities both qualitatively and quantitatively.

The three-electrode setup, consisting of a reference electrode, a counter, and a working electrode, is the experimental setup used for most electrochemical tests on single electrodes. The three electrodes are placed in an electrolyte, which ensures the conductivity of charges between them. The potentiostat applies a potential between the working and reference electrodes, while measuring the current flow between the working and counter electrodes. For this Thesis, all the experiments have TiO_2 as the working electrode, standard calomel ($Hg/HgCl_2$, Gamry®) as the reference electrode, and the counter electrode is fluorine-doped tin oxide (FTO) deposited on a glass substrate (Pilkington TEC 7, 10 Ω/sq). The electrodes are connected to a Gamry® potentiostat and a computer with Gamry® data analysis software. In the following, the three methods used for

electrochemical characterization are introduced in more general terms, whereas more specific details on measurements are given in Chapter 5.

3.2.1 Cyclic Voltammetry (CV)

In cyclic voltammetry, the potential of the working electrode (WE) with respect to the reference electrode is changed linearly with time. This ramping is known as the experimental scan rate, υ, expressed as V/s. Usually the potential is varied with scan rates υ ranging from 10 mV/s to about 1 V/s with conventional electrodes. The data is reported as a current (I [=] A or A/cm^2) versus potential (E) plot. As shown in Figure 3.1, the forward scan (A → C) produces a peak (anodic) current for any analyte that is oxidized. If the scan is started at a potential well positive of E^0 for oxidation, only non-faradaic currents flow for a while. When the electrode potential approaches the E^0 value oxidation begins and current starts to flow. As the potential continues to grow more positive, the analyte concentration in the electrode's vicinity must drop, hence the flux to the surface and the current increase. As the potential moves past E^0, the surface concentration drops nearly to zero and mass transfer of the analyte to the electrode is maximized. Finally, the current drops as the depletion effect sets in. When the potential scan is reversed (C → D), there is a large

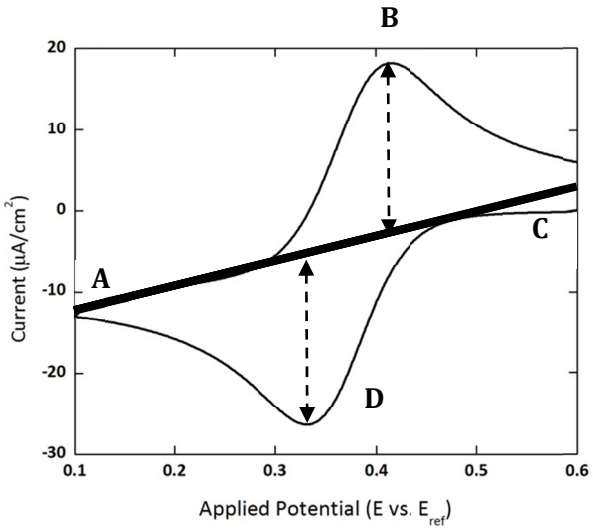

Figure 3.1 Cyclic Voltammogram of Ferrocyanide

concentration of reducible material in the vicinity of the electrode. The above process is repeated and a mirror image of the initial curve is obtained. Two measured parameters of interest on these *I-E* curves are the ratio of peak currents, i_{pa}/i_{pc}, and the separation of peak potentials, $E_{pa} - E_{pc}$. For a completely reversible redox reaction, the curve is a Nernstian wave with $i_{pa}/i_{pc} = 1$ regardless of scan rate, switching potential, and diffusion coefficients.[54]

The characteristics of a cyclic voltammogram depend on (i) the scan rate, (ii) the electron transfer rate, and (iii) the chemical reactivity of the electroactive species. Figure 3.2A[55] illustrates that increasing the scan rate increases the peak current recorded during the cathodic and anodic phases of the potential scan. Decreasing the scan rate increases the time required to record a cyclic voltammogram. Therefore, the size of the diffusion layer above the electrode will grow much further from the electrode compared to a fast scan. Thus, the flux of analyte to the electrode surface decreases leading to a decrease in current. Another point of interest is that the current peak occurs at the same potential regardless of the scan rate. This behavior indicates that the electron transfer reaction is faster than the voltage scan rate. These rapid processes are classified as being reversible electron transfer reactions. In such cases, the Nernst equation, Eq. 3.2, predicts the equilibrium relationship between the voltage, chemical reactivity of the electroactive species, and their

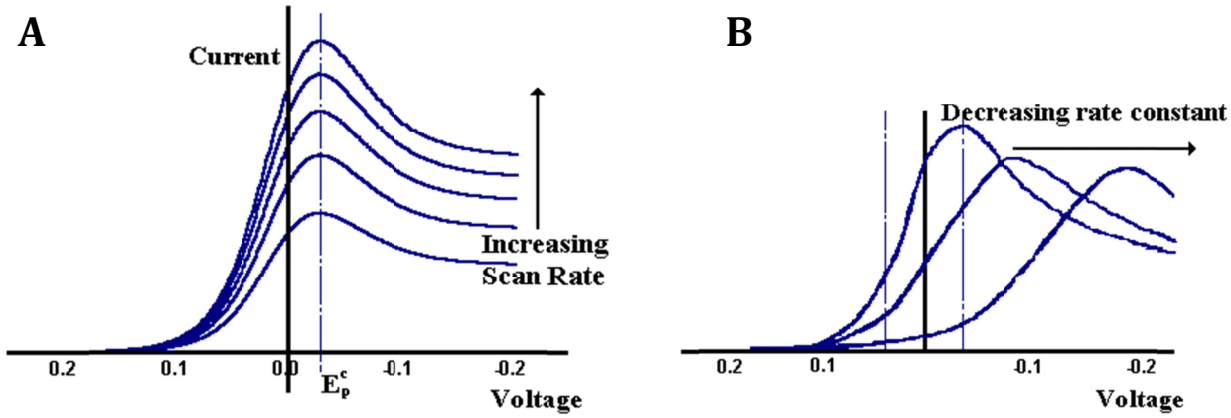

Figure 3.2 (A) Characteristic voltammograms recorded with increasing scan rate. (B) Voltammograms recorded at single scan rate. The changing peak is reflective of non-Nernstian kinetics.[55]

concentration.

$$E = E^o + \frac{RT}{nF} ln \frac{a_{red}}{a_{ox}} \quad \textit{Eq. 3.2}$$

Figure 3.2B shows the instance when the electron transfer kinetics is slower than the voltage scan rate. These processes are classified as being quasi-reversible or irreversible electron transfer reactions. The voltammograms shown are recorded at a single scan rate. In this situation, the voltage applied will not generate analyte concentrations predicted by the Nernst equation, which is only valid at equilibrium. Due to the slow kinetics, equilibrium is not established fast enough with respect to the scan rate, and the current takes more time to respond to the applied voltage. As a result, the current peak shifts depending on the kinetic rate constant.

3.2.1.1 CV Analysis of DSSCs

Cyclic voltammetry is a classic diagnostic tool for electrochemical systems. In DSSCs, it provides a quick way to investigate the process of trap filling. During the scanning of the potential, an electron charging/discharging process occurs at the electrode/electrolyte interface, thus allowing the state of the prepared films to be estimated. At a given scan rate, the dominant electron activity can be determined. A basically symmetric CV, where the current increases exponentially with voltage, directly records the intrinsic film capacitance. The presence of a series resistance (e.g., viscous electrolyte) distorts the symmetric capacitive shape in proportion to the current. Under these conditions, a large positive peak is observed corresponding to the discharge of the charge accumulated when the current was negative. If the charge transfer resistance is dominant, then charge accumulation is hindered and the positive peak disappears.

3.2.2 Electrochemical Impedance Spectroscopy (EIS)

Unlike cyclic voltammetry, which measures transient responses while imposing large perturbations on the system, EIS measures the steady state impedance responses to an alternating

signal of much smaller magnitude. EIS is capable of measuring the influence of the governing physical and chemical phenomena within an electrochemical cell. In recent years, EIS has found widespread application in the field of materials characterization. It is routinely used in the characterization of coatings, batteries, and common corrosion phenomena. It is gaining popularity in the study of ionic diffusion across membranes and toward semiconductor interfaces. [56,57]

The concept of impedance is very similar to that of resistance, i.e., it is defined as the opposition to the flow of current. However, a resistor is an idealized circuit element whose response does not depend on the frequency of the excitation signal. Ohm's law (Eq. 3.3) states:

$$R = \frac{E}{I} \qquad \textit{Eq. 3.3}$$

On the other hand, impedance is a generalized version of resistance. It displays a dependence on the frequency of the excitation signal. For example, applying a sinusoidal potential excitation signal to a linear system yields a phase-shifted sinusoidal current signal as shown in Figure 3.3.

In EIS, a small AC signal is superimposed on a background DC excitation potential. The amplitude of the AC signal must be small in order to mimic a linear electrochemical system. This

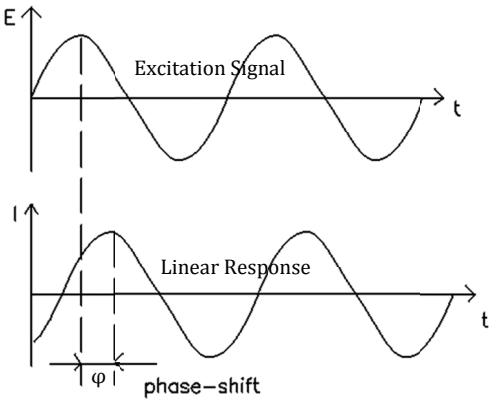

Excitation signal: $E_t = E_o \sin \omega t$

Linear Response: $I_t = I_o \sin t\ (\omega t + \varphi)$

where, $\omega = = 2\pi f$ =radial frequency, and φ = phase shift.

$$Z = \frac{E_t}{I_t} = \frac{E_0 \sin \omega t}{I_0 \sin(\omega t + \varphi} = Z_0 \frac{\sin \omega t}{\sin(\omega t + \varphi)}$$

COMPLEX NUMBER REPRESENTATION:

$$Z = \frac{E}{I} = Z_o \exp(j\varphi) = Z_o(\cos\varphi + j\sin\varphi) = Z_{Re} - Z_{Im}$$

Figure 3.3 EIS signal, response, and mathematical representation.

need arises from the fact that the current–overpotential relationship is linear for very small overpotentials. The Butler-Volmer equation, Eq. 3.4, is the standard model used to describe the current-overpotential relation for an electrode at a specified temperature, pressure, and redox concentration.

$$i = i_o \left[exp \frac{\alpha_a F}{RT} \eta_s - exp \frac{\alpha_c F}{RT} \eta_s \right] \qquad \textit{Eq. 3.4}$$

where, $\eta_s = E - E_o$. At very low overpotentials, the above expression simplifies to the linear equation 3.5.

$$i = i_o \frac{(\alpha_a + \alpha_c)F}{RT} \eta_s \qquad \textit{Eq. 3.5}$$

A Nyquist plot or a Bode plot is used to represent EIS data graphically (Fig. 3.4). On Bode plots (Fig.3.4A), the impedance is plotted with log frequency on the X-axis and the absolute values of the impedance (*|Z|*) and the phase-shift (φ) on the Y-axis. The Nyquist graph (Fig. 3.4B) plots the real and imaginary components of the impedance on the X- and Y-axes, respectively. One disadvantage of the Nyquist representation is the lack of frequency information.

The characterization of electrochemical systems with impedance spectroscopy requires the interpretation of the data with the help of suitable models. These models can be divided into two

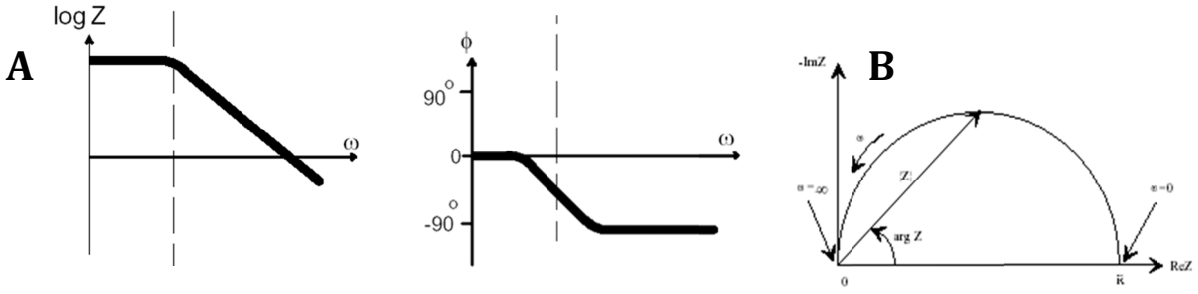

Figure 3.4 (A) Bode plot. Impedance and phase lag at each frequency is displayed. (B) Nyquist plot. Imaginary vs. Real component of impedance is shown. This plot is useful for distinguishing different interfaces in the electrochemical cell.

broad categories: equivalent circuit models and process models. The models are regressed to experimental data to estimate parameters that can be used to predict the behavior of the system under various conditions. Equivalent circuit models are most commonly used to interpret impedance data. These models are built with the help of well-known passive elements such as resistors, capacitors, and inductors and distributed elements such as the constant phase element and the Warburg impedance. Table 3.1 summarizes the impedances associated with each circuit element. The elements can be combined in series and parallel to give complex equivalent circuits. A certain physical meaning is then assigned to the various elements of the equivalent circuit.

Table 3.1 Impedance definitions of standard circuit elements

Circuit Element	***Impedance***
Resistance	$Z = R$
Capacitance	$Z_C = \frac{1}{j\omega C}$
Constant Phase Element (CPE)	$Z_{CPE} = \frac{1}{Y_0(j\omega)^n}$ when n=1, CPE behaves as a pure capacitor n=0, CPE behaves as a pure resistor n=0.5, CPE behaves similar to a Warburg element
Warburg Impedance	*Infinite Diffusion Layer* $Z_{war} = \frac{1}{Y_0\sqrt{j\omega}}$ *Finite Diffusion Layer* $Z_{war} = \frac{1}{Y_0}\tanh B\sqrt{j\omega}$, where $B = \frac{\delta}{D}$ δ = diffusion layer thickness D = diffusion coefficient
Inductance	$Z_L = j\omega L$

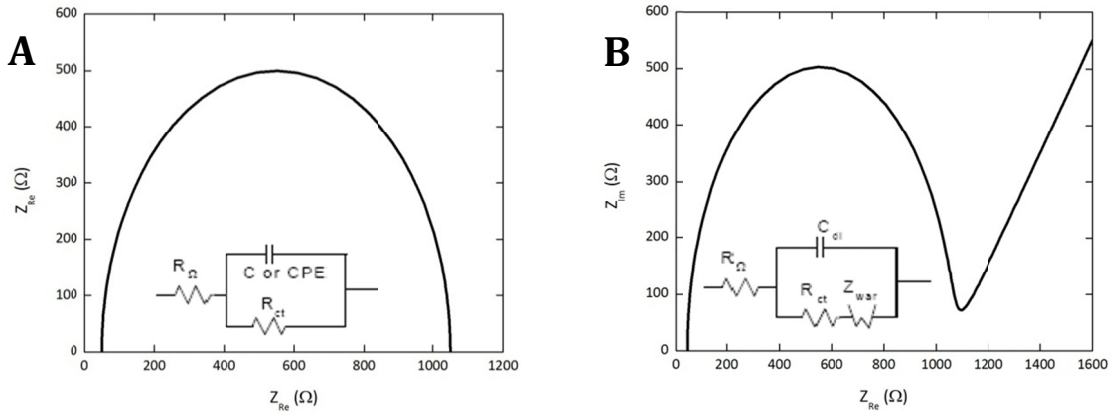

Figure 3.5 Nyquist plot of inset equivalent circuit. (A) Randles circuit. (B) modified circuit to show the effect of an infinite diffusion element.

One of the most common equivalent circuits is the simplified Randles circuit shown in Figure 3.5A. It includes a solution resistance (R_Ω), a double layer capacitor (C) or a CPE, and a polarization resistance (R_{ct}). This combination of elements can accurately describe electron transfer at an electrode, and it is often used as a starting point for more complex models. A more complex version (Fig.3.5B) of the Randles circuit models a cell, in which polarization is due to a combination of kinetic (R_{ct}) and diffusion (Z_{war}) processes. The addition of a Warburg element to the Randles circuit model can describe diffusion-limited electron transfer.

Since the equivalent circuit is built based on the data, there can be many different combinations that yield the same data. Hence, one cannot automatically assume that an equivalent circuit that produces a good fit to a data set represents an accurate physical model of the cell. Prior knowledge or complementary experiments must be done to determine and/or confirm the appropriate model for the data. This difficulty is one of the limitations of impedance spectroscopy.[54]

3.2.2.1 EIS Analysis of DSSCs

Bisquert used an infinite transmission line description to model electron transport processes within a nanostructured electrode.[58] In his approach, the mesoscopic film is thought to be composed of a string of oxide nanoparticles. The equivalent electrical circuit, shown in the lower

part of Figure 3.6, treats each particle as a resistive element coupled to the electrolyte through the interface. The latter is presented by the electric double-layer capacitor (C) connected in parallel with the resistance (r_{ct}) for interfacial electron transfer. The red dots denote electrolyte cations.

It is clear from Figure 3.6 that the movement of electrons in the conduction band of the mesoscopic films must be accompanied by the diffusion of charge-compensating cations in the electrolyte layer close to the nanoparticle surface. The cations screen the Coulomb potential of the electrons avoiding the formation of uncompensated local space charges, which would impair the electron's motion through the film. This situation justifies using an "ambipolar" or effective diffusion coefficient, which contains both contributions from the electrons and charge-compensating cations to describe charge transport in such mesoscopic interpenetrating network solar cells.[58,59]

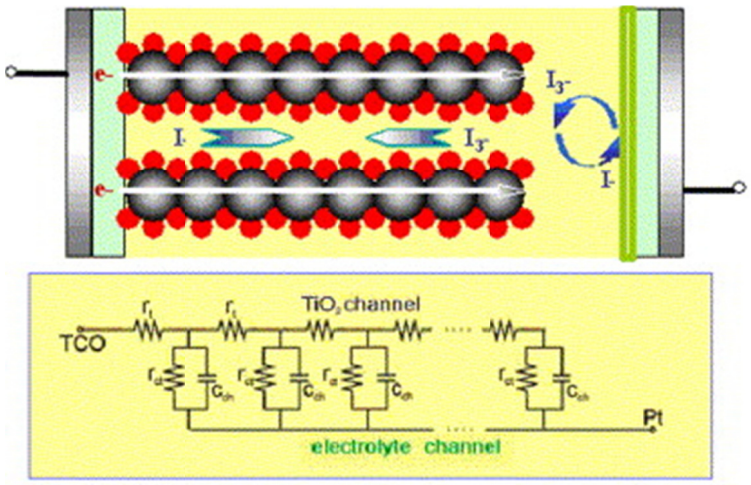

Figure 3.6 Equivalent circuit of DSSC[58]

3.2.3 Chronoamperometry

In chronoamperometry, the potential of the working electrode is stepped, and the resulting current from faradaic processes is monitored as a function of time. The potential difference between the working and reference electrodes starts out at zero, where no redox reaction occurs.

The voltage then jumps on the working electrode, such that a redox reaction is induced. The redox reaction immediately depletes the oxidant in the vicinity of the electrode, while increasing the reductant. The resultant concentration gradient leads to a flux of oxidant toward the electrode and reductant away from the electrode. This moving charge can be measured by an ammeter and is called the diffusion current. The current response to this sweep in potential is characterized by an immediate jump in current which drops off as the oxidant is depleted (Fig. 3.7). The diffusion current, *i(t)*, can then be related to the analyte concentration, *C*, and its diffusion coefficient, *D*, by the Cottrell equation, Eq. 3.6:

$$i(t) = nFAC\sqrt{\frac{D}{\pi t}} \qquad \textit{Eq. 3.6}$$

where *n* is the number of moles and *A* is the area of the electrode.[54]

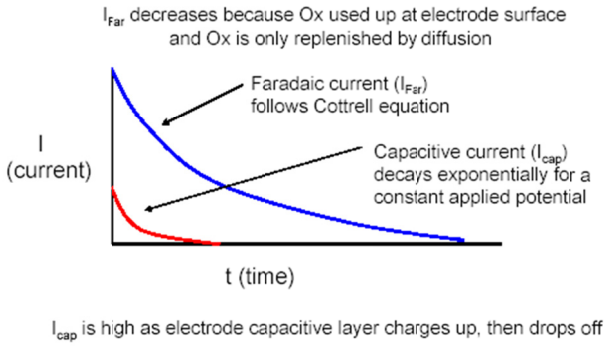

Figure 3.7 Chronoamperometric response in the presence (blue) and absence (red) of a redox couple.

3.2.3.1 CA Analysis of DSSCs

A transient current is measured following a potential step in the working electrode. At short times, the current consists of a large non-faradaic component due to charging of the double-layer. This capacitive current, i_c, decays exponentially with a time constant, RC_d, where *R* is the electrode

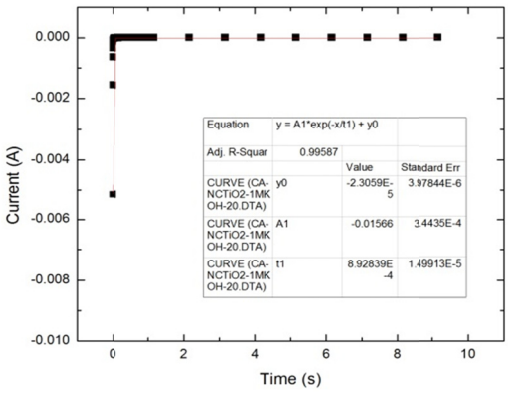

Figure 3.8 Example of a fitted decay of a transient current to determine RC_d.

resistance and C_d is the double-layer capacitance. The transient current, as shown in Figure 3.8, is fitted with the expression given in Eq. 3.7:

$$i_c = \frac{\Delta\varphi}{R} e^{-t/RC_d} = A1e^{-x/t1} \qquad \textit{Eq. 3.7}$$

The time constant, RC_d, determines the shortest time required to conduct the chronoamperometry experiment. In order to ensure the reliability of results presented in this Thesis, measurements were performed for much longer times (>5RC_d) than RC_d. Provided the final potential following the step change is positive of the flatband potential, the measured capacitive current is a good indicator of the surface traps present on the electrode.

3.3 Photoelectrochemical Characterization

Testing the prepared inverse opal TiO_2 electrodes in the photoelectrochemical mode is the final step of characterization and reveals the symbiotic relationship of the different parts of the DSSC. Unlike electrochemical tests which are used to investigate singular electrodes (and hence require a reference electrode), photoelectrochemical tests are used to characterize the performance of the entire electrochemical cell. Hence, these experiments are done using an electrochemical cell comprising a working electrode and a counter electrode.

3.3.1 Photocurrent – Voltage measurements

The standard characterization techniques of solar cells include the DC current-voltage response under white light illumination at different intensities and the determination of the photocurrent under low intensity monochromatic light. The photocurrent–voltage curves can be obtained by applying a potential scan, from 0 V (short-circuit conditions) to open-circuit potential,

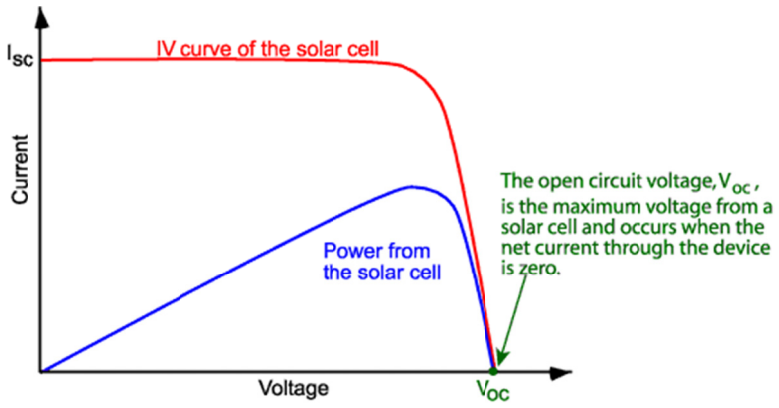

Figure 3.9 Typical IV curve of a solar cell.[60]

under constant illumination. Figure 3.9[60] shows a typical IV curve at a single light intensity. As the light intensity increases, the maximum short-circuit, I_{sc} (or current density, J_{SC}), and the open circuit voltage, V_{oc}, increase. From the photocurrent-voltage curves, the following parameters can be obtained: [61-63]

- ***Short-circuit current, I_{SC}***: The cell current measured at an applied potential of 0 V. I_{SC} is a function of the illumination intensity
- ***Open circuit voltage, V_{OC}***: The cell potential measured when the current is 0 A.
- ***Maximum Power Output, P_{max}***: For a given bias voltage the power output of the cell is the product of the measured cell current and the voltage. $P(V) = I * V$. I_{max} and V_{max} are the coordinates of the maximum in the P(V) curve. The maximum power corresponds visually to the area of the largest rectangle that can fit inside the current voltage curve.
- ***Fill Factor, FF***: The ratio of the maximum power to the short and open circuit values, Eq. 3.8.

$$FF = \frac{I_{max} * V_{max}}{I_{SC} * V_{OC}} \qquad \textit{Eq. 3.8}$$

- ***Efficiency, η:*** The ratio of the maximum electric power extracted to the radiation power incident on the solar cell surface as depicted in Eq. 3.9.

$$\eta = \frac{P_{max}}{P_{in}} = \frac{I_{SC}*V_{OC}*FF}{P_{in}} \qquad \textit{Eq. 3.9}$$

3.3.2 Open Circuit Voltage Decay

Electron transfer kinetics play a major role in determining the energy conversion efficiency of DSSCs. Open Circuit Voltage Decay (OCVD) is a powerful tool to study the electron lifetime as a function of the photovoltage (V_{OC}). This technique has certain advantages over frequency or steady-state based methods: (i) it provides a continuous reading of the lifetime as a function of V_{OC} at high-voltage resolution, (ii) it is experimentally less difficult, and (iii) the data treatment is also straightforward.

When the cell is illuminated at open circuit, the free electron density in the TiO_2 is affected by two main processes: (i) electron photogeneration and (ii) electron recombination. Electron photogeneration is achieved by electron injection from the attached photoexcited dye molecules into the conduction band of the TiO_2. The dye molecules are accordingly oxidized. The photogeneration process can be maintained at a stationary rate because the reduced electrolyte species are able to regenerate the oxidized dye molecules. The recombination of the photogenerated electrons occurs by reaction with the electrolyte-oxidized species and is thought to be predominant in comparison with electron capture by the oxidized dye.[17]

3.3.3 Cyclic Voltammetry at Low Scan Rates

Diffusion-limited currents within the electrochemical cell can be determined by measurement of a cyclic voltammogram using a slow scan rate (5 – 10 mV/s). Steady-state conditions can be achieved and demonstrated by a very small hysteresis. The diffusion-limited current density, j_{lim}, measured is proportional to the diffusion constant of I_3^-, $D(I_3^-)$, as given in Eq. 3.10.

$$j_{lim} = \frac{2ne_oD_{I_3^-}c_{I_3^-}N_A}{l} \qquad \textit{Eq. 3.10}$$

Due to the large excess of I^- in the electrolyte, only the diffusion of I_3^- limits the current. Diffusion constants can also be determined by measurement of the Nernst impedance. However, due to its small effect on the impedance spectrum, this method is less reliable than the determination from diffusion-limited currents. Especially for solvents with a low diffusion constant, EIS is not suitable, because then the effect of diffusion takes place in the very low frequency range, or it is masked by other impedance features.[41]

3.4 Chapter Summary

OM and SEM in combination with FFT are used to determine the structure of the inverse opal electrodes, while CV, EIS, and CA give insight into the electrochemical characteristics of the TiO_2 electrodes such as surface trap density, trap filling, and recombination kinetics, as a function of their pore size. Last but not least, photocurrent-voltage curves, open circuit voltage decay, and CV at slow scan rates are used to characterize the performance of inverse opal electrode based DSSCs. In the following three chapters, first the electrode structure is investigated (Chapter 4), followed by results from electrochemical testing (Chapter 5), and concluded by photoelectrochemical tests in functional DSSCs (Chapter 6).

4 Titania Photoanodes with Inverse Opal Network Geometry

In this chapter, we report on inverse opal TiO_2 electrode fabrication from templating particles ranging in size from 0.5 to 10 μm using a set of six regularly employed colloidal assembly methods. Only the method of and the particle size used for opal assembly are varied, while the colloidal particles, infiltration material, and conditions for infiltration are kept the same. Our results identify specific methods for each particle size leading to inverse opal TiO_2 electrodes with pore sizes ranging from the submicron to micron range with comparable structural quality.

4.1 Advantage of Inverse Opal Structured DSSC Electrodes

There are several potential advantages associated with the use of inverse opals as the anode in DSSCs. First, the inverse opal structure is the closest packing of spherical voids arranged in a face-centered cubic array, which leads to the highest spherical surface area per unit volume available for dye adsorption. Second, the ordered and continuous thin shell of the inverse opal structure serves as a fast electron transport path. Ofir et. al[64] found that the internal connectivity of the nanoparticulate network has an important influence over the rate of electron diffusion. An unbroken lattice of thin shells can enhance electron transport due to geometric confinement and a reduction in degrees of freedom of movement. Third, the highly ordered structure of the inverse opal reduces the mass transfer resistances of electrolyte transport and dye-impregnation within the regularly connected spherical voids and thus results in efficient electrolyte-dye interactions. It also reduces tortuosity in the electron transport paths, thus favoring electron transport.

Aside from improving the absorption spectrum of the dye[65] and using nanostructured electrodes, another avenue for DSSC efficiency improvement is to increase the open-circuit voltage, V_{OC}, which is determined by the difference between the electron quasi-Fermi level of the electrode under illumination and the redox level of the electrolyte.[66] Strategies to increase the V_{OC} involve either (a) moving the redox level of the electrolyte by changing the electrolyte, or (b) inhibiting the recombination rate, i.e., electron transfer to the oxidized dye molecule. Once again, inverse opals, exhibit a high surface area and internal accessibility, which can accommodate new, generally more viscous electrolytes. Alternative electrolytes that have received recent attention include cobalt polypyridine complexes[67] in a 60:40 mixture of ethylene carbonate and acetonitrile as well as solid-hole conductors such as spiro-OMeTAD in chlorobenzene.[68] The solvent mixtures used for these alternative redox couples are more viscous than acetonitrile ($\eta_{acetonitrile}$ = 0.369 mPa·s at 25°C[69] vs. $\eta_{ethylene\ carbonate}$ = 1.925 mPa.s at 40°C[70]and $\eta_{chlorobenzene}$ = 0.753 mPa.s at 25°C[69]), which is used in the traditional DSSC configuration. In this case, the open, porous structure of the inverse opal enables enhanced diffusion of electrolyte ions in the cell. Another advantage of the inverse opal over the nanoporous electrode is the accessibility of its internal structure. The infiltration of a viscous electrolyte into a nanoporous structure can be problematic due to incomplete wetting of the structure, which may increase recombination as a result of reduced electrode-electrolyte interface. In addition to having a large surface area per unit volume, the periodicity of the inverse opal electrode also lends itself to trapping of light within the DSSC, thus improving photon capture.[71] However, inverse opal electrodes have a smaller surface area in comparison with the nanoporous electrodes. In order to balance the advantages of high surface area and accessibility to the electrode surface for more viscous electrolytes, a systematic study of pore-size dependent electrochemical properties, such as electron diffusion, electron lifetime, and trap density, is of interest. Such a study requires electrodes of uniform structure and varying pore size, which are accessible via colloidal templating methods.

4.2 Synthesis of Inverse Opal TiO_2 Electrodes

Inverse opal synthesis via colloidal crystal templating is most attractive because of its low cost and versatility. The general recipe for making these porous structures consists of three sequential steps: (a) self-assembly of monodisperse colloidal particles into a crystalline (usually face-centered cubic, hexagonal close-packed, or a blend) template, (b) infiltration and deposition of the desired inverse opal material or its precursor into the pores, and (c) removal of the template to yield the inverse opal structure.[72] From a survey of the literature,[73-79] it is clear that many colloidal templating methods have been developed, but that there is no single colloidal templating method that can be consistently used to yield pore sizes spanning the submicron to micron length scale. Most colloidal self-assembly methods rely on gravitational, buoyancy, convective/immersion, and/or electrophoretic forces to form large arrays of close-packed (74%) spheres. Accordingly, we have chosen sedimentation (S) [80-82] and interfacial assembly (IA)[83] to study the particle-size dependent effects of gravitational and buoyancy forces, respectively. Electrophoretic deposition (EPD)[84] is used to study the impact of electrophoretic forces on particle-size dependent assembly. The particle-size dependent effects of convective/immersion forces are studied in horizontal and vertical geometry in convective assembly (CA)[85] and liquid phase deposition (LPD),[86,87] respectively. A more recently developed method, so-called co-assembly (CoA),[88] combines the opal formation and infiltration steps and its particle-size dependence is therefore also considered here.

Materials: Opals were prepared from colloidal suspensions of sulfate-terminated polystyrene particles (PS) purchased from Invitrogen (IDC Latex). Table 4.1 summarizes the particle sizes and standard deviations provided by Invitrogen. With exception of the 10 μm particles, the variability in the diameter of the particles was below the 5-8% threshold, and can therefore be classified as monodisperse.[89] The inverse opal replicas were prepared by filling the opal pores with a titania precursor solution of a known recipe:[90] titanium (IV) isopropoxide (Fisher Scientific), 1-butanol, acetylacetone (Sigma Aldrich), para-toluenesulfonic acid, and Millipore deionized water. Titanium

(IV) bis-ammonium lactate dihydroxide (Ti-BALDH, 50% aqueous solution) (Sigma-Aldrich) was used as the precursor for the co-assembly method. All samples were deposited on 1"×1" fluorine-doped tin oxide (FTO, Pilkington TEC7, 10 ohms/sq) substrates. Three samples were prepared per particle size and assembly method.

Table 4.1 Average size of polystyrene sulfate latex particles.

PS [μm]	Size Distribution[a]	Pore Size [μm]	% difference
0.5	0.5 ± 0.011	0.27 ± 0.070	-24%
1.0	1.0 ± 0.014	0.76 ± 0.048	-24%
2.4	2.3 ± 0.120	1.43 ± 0.110	-38%
5.0	5.0 ± 0.060	3.10 ± 0.290	-38%
10.0	9.5 ± 0.930	4.73 ± 0.549	-50%

[a] Numbers reported by Invitrogen

Substrate Orientation		Method		Aqueous Stock Solution [PSS]	Aqueous Stock Solution Solvent	Experimental Conditions	Reference
Horizontal	A	Sedimentation (S)		8% vol.	Water	Ambient	Ref. [78-80]
	B	Interfacial Assembly (IA)		8% vol.	Ethylene Glycol / Water (0.22 mol. frac.)	55±5°C	Ref. [81]
	C	Convective Assembly (CA)	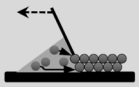	8% vol.	Water	Ambient	Ref. [83]
Vertical	D	Electrophoretic Deposition (EPD)	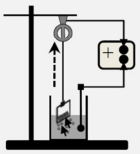	0.1% vol.	Water, Ethanol, Ammonium Hydroxide (1:2:0.044 by volume)	6V (0.5 & 1.0 μm) 7V (2.4 μm)	Ref. [82]
	E	Liquid Phase Deposition (LPD)	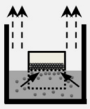	0.2% vol.	Water	55±5°C	Ref. [84,85]
		Co-Assembly (CoA)		0.1% vol.	Water, 0.07% Ti-BALDH	55±5°C	Ref. [86]

Figure 4.1 Experimental details for Opal Fabrication Methods. (A) Sedimentation, (B) IA, (C) CA, (D) EPD, (E) Liquid Phase Deposition/CoA. Solid arrows indicate direction of prominent assembly forces. Dashed arrows indicate evaporation flux or direction of moving parts (see text for details).

Opal Fabrication: Figure 4.1 summarizes the experimental setup and materials used for the six methods studied. Based on the position of the substrate during opal assembly, the different methods are divided into two categories: horizontal (Fig. 4.1A - C) and vertical deposition (Fig. 4.1 D -E) methods. The thickness and uniformity of the opals were controlled by experimental parameters such as the volume of suspension, colloidal concentration, and withdrawal or evaporation rates. The substrate was washed using isopropanol, acetone, and DI water prior to use. The polystyrene (PS) solution was assembled into a well of dimensions 1.6 cm × 0.8 cm. The well molds, an acrylic film with adhesive backing, were made using a paper punch of the same dimensions. Further details for each method can be obtained from the references listed in the rightmost column of Figure 4.1.

Inverse Opal Fabrication: Each opal sample, which was left leaning on a larger glass slide, was dipped in a bath of the titanium dioxide precursor.[91] The concentration of TiO_x in the Ti-isopropoxide precursor was ~12.5 % in butanol and that of the Ti-BALDH (used for co-assembly) was ~10 % in water. The precursor infiltrated via capillary action. The slanted position of the substrate prevented the formation of an overlayer. After ~15 minutes of infiltration time, the slide was removed and allowed to air dry vertically for 15 minutes. This procedure was repeated three times. In the later treatments, a top slide was added to help the liquid climb to the top of the sample to ensure complete infiltration. Finally, the samples were sintered in a temperature-controlled furnace (Barnstead Thermolyne 1400) at 450 °C. Note that the pores are on average 31 % smaller than the polystyrene template particles used (see Table 4.1) due to the conversion of the amorphous TiO_2 precursor to the anatase crystal structure, in good agreement with values reported for sol-gel methods.[92-94] The mechanical stress caused by this reduction in crystal lattice spacing leads inevitably to crack formation in TiO_2 inverse opals (see below).

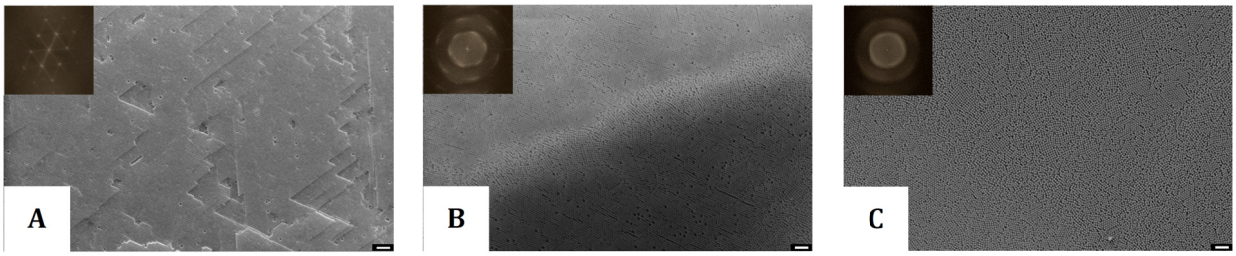

Figure 4.2 Fast Fourier Transform(FFT) of scanning electron micrographs (SEM). (A) SEM image of opal made from 0.5 μm particles by liquid phase deposition. Inset: High degree of order in the opal is reflected by the pronounced hexagonal pattern in the FFT. (B) SEM image of opal made from 0.5 μm particles by CA. Inset: Polycrystallinity of the opal is apparent from the appearance of diffuse spots in the FFT. (C) SEM image of opal made from 0.5 μm particles by CA. Inset: Amorphous nature of the close-packed particles is shown by the ill-defined halo in the FFT. Scale bar in micrographs is 10 μm.

Characterization: All opal and inverse opal samples were imaged using a Zeiss EVO 40 Scanning Electron Microscope (SEM) in high-vacuum mode. SEM images of each sample were taken at four (1250×, 522×, 200×, and 100×) magnifications. The magnification of the images used for comparison were chosen to show a similar number of particles (10^4 particles) for each particle size: 0.5 μm (1250x), 1.0 μm (522x), 2.4 μm (522x), 5.0 μm (200x), and 10.0 μm (200x).

The quality of the opals and inverse opals obtained from each method was analyzed via Fast Fourier Transforms (FFT) of the respective SEM images.[52,95,96] Both opal and inverse opal structures are highly periodic in nature, and any structural defects that lead to a break in the periodicity are detected in the reciprocal of the actual image. Applying FFT to an image transforms it from the spatial domain to reciprocal space (see Chapter 3 for details). Fig. 4.2 shows exemplary FFTs for opals made from 0.5 μm particles. FFT images show spots for single crystals (Fig. 4.2 A) or diffuse spots or rings for polycrystalline samples (Fig. 4.2 B) and contain information on lattice periodicity. Crystal defects such as dislocations and stacking faults appear as randomly distributed points grouped along crystallographic directions. For amorphous materials, the FFT images consist of ill-defined diffuse halos (Fig. 4.2 C). The presence of structural defects affects the power spectrum by decreasing the spot intensities and increasing the diffuse background. [95]

The FFT analysis of the images (1023×767 pixel area) was done using NIH ImageJ 1.45i. The scale bar determined by the SEM software was used as the calibration standard for spatial dimensions. A square grid was superimposed over an SEM image to assist in the measurement of the single-crystal domain size. The grid size was chosen such that areas of apparent single-crystal domains were contained within the grid windows, while avoiding grain boundaries. The numbers reported for the opals reflect the largest contiguous single-crystal domain with identical FFT, i.e., when the FFT of two neighboring squares were identical they were counted towards the same single crystal domain.

The inverse opal FFT analysis is more delicate due to the presence of cracks. Although cracks break up the inverse microstructure, the orientation of the pores in the "cracked domains" remains unchanged. However, FFT analysis is sensitive to such defects and translates cracks as diffuse halos, and ultimately masks the order shown by the pores on either side of the crack. As a result, single-crystal domains of the inverse opals are measured across cracks, while excluding the crack itself.

4.3 Comparison of Inverse Opal Electrode Quality as a Function of Pore Size and Preparation Method

Sedimentation (S), interfacial assembly (IA), convective assembly (CA), electrophoretic deposition (EPD), liquid-phase deposition (LPD), and co-assembly (CoA) have been used to prepare opal structures from templating particles ranging in size from 0.5 to 5 μm. Opals were subsequently infiltrated with a titania precursor and calcined leading to the formation of inverse opal structures. Both opal and inverse opal structures were analyzed using scanning electrode microscopy (SEM) and Fast Fourier transform (FFT). Note 10 μm particles did not yield close-packed opals with any of the six methods due to their polydisperisty and therefore were excluded from detailed analysis.

Figs.4 3 and 4.4 present representative SEM images of opals and inverse opals, respectively, for each method (rows) and particle size (columns) allowing for a quick qualitative comparison of the opal and inverse opal structures with respect to their quality, number of cracks, and apparent domain size. Figs. 4.3 F and 4.4 F depict a digital image of an opal and an inverse opal electrode revealing their long-range order through opalescent colors.

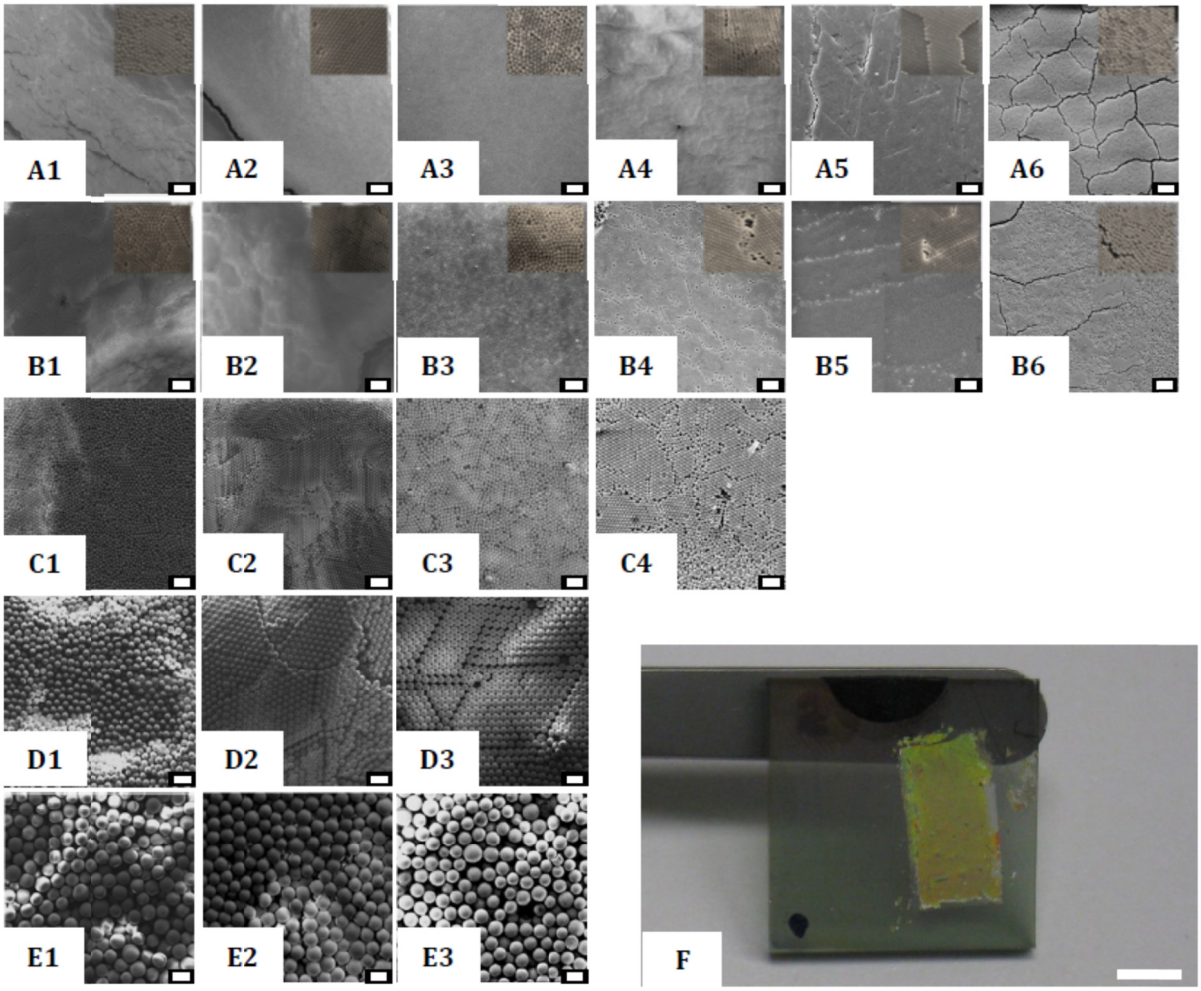

Figure 4.3 SEM images of PS opals. Rows represent particle sizes—(a) 0.5 µm, (b) 1.0 µm, (c) 2.4 µm, (d) 5.0 µm, and (e) 10.0 µm. Columns represent methods—(1) Sedimentation, (2) IA, (3) CA, (4) EPD, (5) Liquid Phase Deposition, and (6) CoA. Scale bars are 10 µm. Areas of larger magnification (4× for 0.5 µm, 2× for 1.0 µm) are included as insets for opals made from particles with 0.5 and 1.0 µm diameters (top two rows). (F) Photograph of opal prepared from 1.0 µm particles by sedimentation showing typical iridescent appearance. Scale bar is 6 mm.

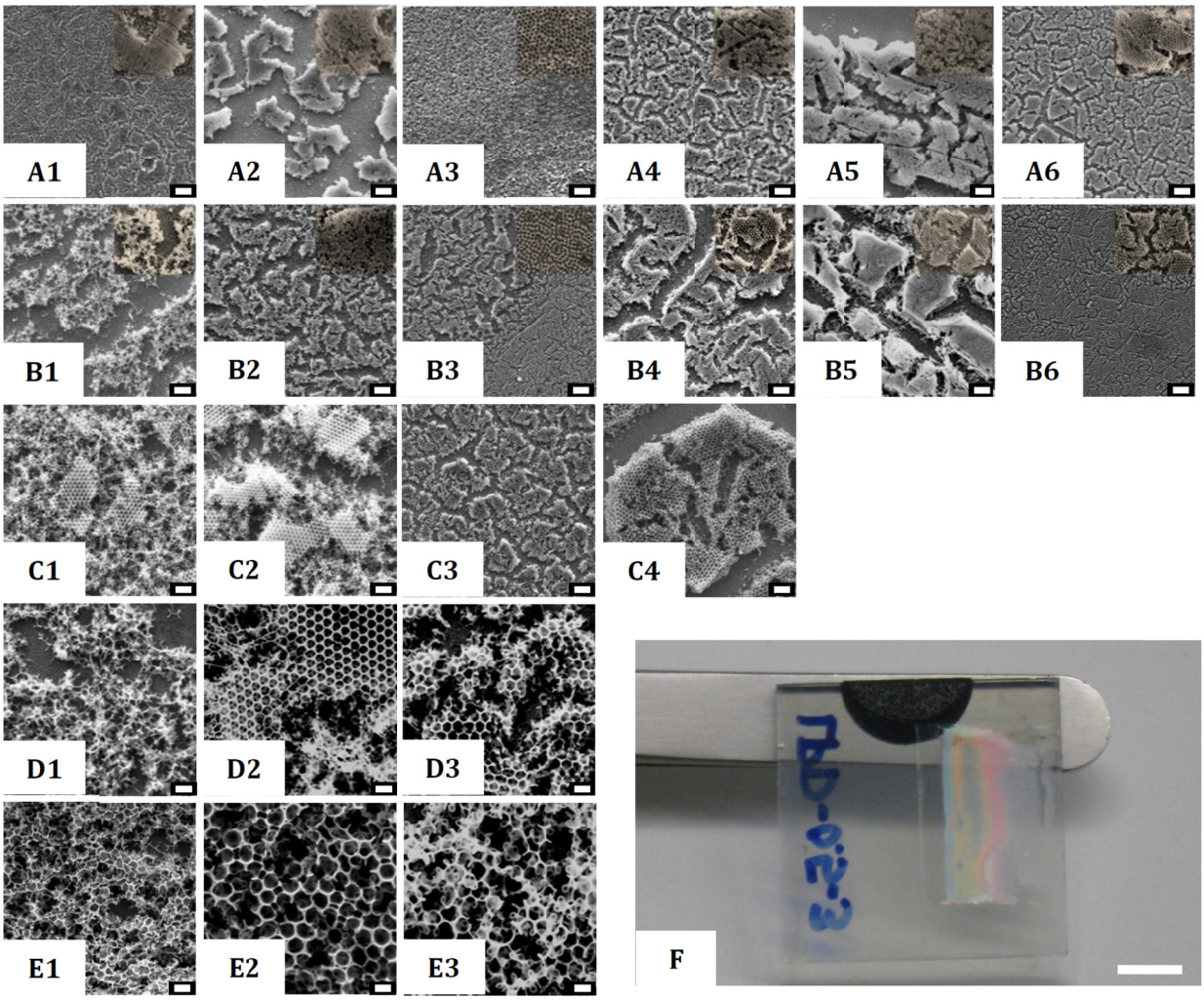

Figure 4.4 SEM images of titania inverse opals. Rows represent particle sizes—(A) 0.5 μm, (B) 1.0 μm, (C) 2.4 μm, (D) 5.0 μm, and (E) 10.0 μm. Columns represent methods used for opal template formation—(1) Sedimentation, (2) IA, (3) CA, (4) EPD, (5) Liquid Phase Deposition, and (6) CoA. Scale bars are 10 μm. Areas of larger magnification (4× for 0.5 μm, 2× for 1.0 μm) are included as insets for inverse opals made from opals with 0.5 and 1.0 μm diameter particles. (F) Photograph of inverse opal prepared from 0.5 μm

Subsequently, quantitative comparison of domain sizes is performed by analyzing the SEM images using FFT yielding the size of single-crystalline areas (Fig. 4.5). The typical domain size for each method and particle size is generally smaller than the area displayed at the magnification chosen for FFT analysis. Hence, each image contains at least two complete domains. Reported domain size values are averaged over results from at least three images from three independently prepared samples. Figure 4.5 shows the trends for the largest single crystal domain found for the

opals (Fig. 4.5A) and inverse opals (Fig. 4.5B), respectively, as prepared by the various assembly methods.

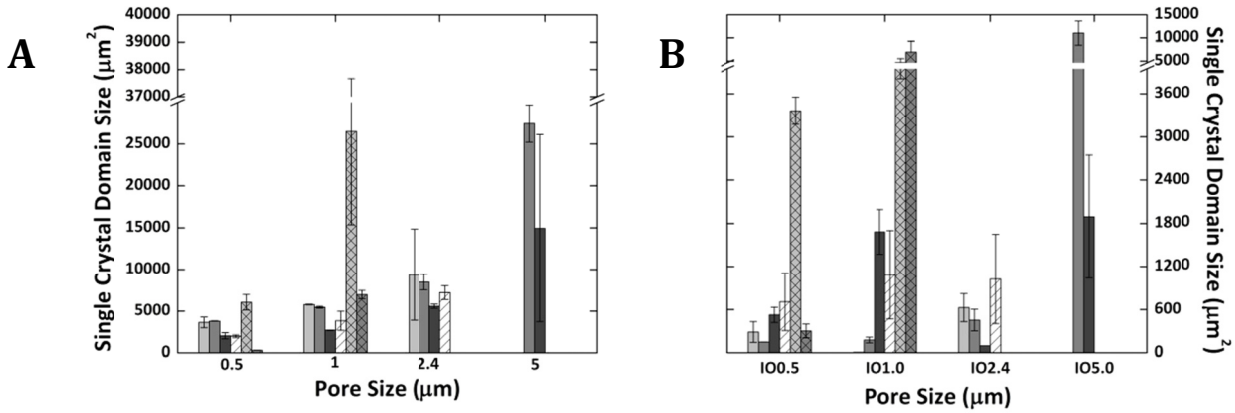

Figure 4.5 Domain size in μm² obtained from FFT analysis for (a) opals and (b) inverse opals with particles ranging from 0.5 to 5 μm. Patterns and shades indicate the six assembly methods: sedimentation—light gray, IA—dark gray, CA—black, EPD—white hatched, liquid phase deposition—white, cross-hatched, and CoA—dark gray, crosshatched..

From Figure 4.5, it can be concluded that 0.5 and 1.0 μm particles show a clear preference for vertical deposition methods (hatched), whereas the larger particles (2.4 and 5.0 μm) prefer the horizontal deposition methods (solid). Convective Assembly (CA, black) shows the smallest single crystal domains regardless of particle size. The preference of the smaller particles (0.5 and 1.0 μm) for liquid phase deposition (LPD, crosshatched) translates to their inverse opal structures. On the contrary, the preferred opal assembly method of each of the larger particles (2.4 and 5.0 μm) does not translate to their inverse opals structures. Comparison of Figures 4.5 A and 4.5 B reveals an overall decrease of 66% in single-crystal domain size from opals to inverse opals in good agreement with the 31% reduction in pore size due to densification of the TiO_2 precursor during calcination (Table 4.1) and the qualitative differences apparent from the SEM images displayed in Figs. 4.3 and 4.4.

4.4 Choosing an optimum method for Inverse Opal fabrication

The aim of our study has been the preparation of TiO_2 inverse opal electrode structures of comparable quality and domain size with varying pore sizes and minimal grain boundaries, which can then be employed for the elucidation of particle size dependent trends in electrochemical studies with viscous electrolytes. An inverse opal electrode, when fabricated under optimum conditions, is a structure with a predictable pore size and porosity. Accordingly, these electrodes are especially apt when the intent is to systematically study pore-size dependent electrochemical properties. In a traditional DSSC, the TiO_2 electrode is comprised of a random network of interconnected ~20 nm TiO_2 nanoparticles that are sintered together. This configuration has a distribution of cracks and grain boundaries that vary from one electrode to the next. Electrochemical properties of such an electrode would depend on the method of fabrication of the TiO_2 nanoparticle as well as the electrode itself. On the other hand, an inverse opal electrode when synthesized by a single method has reproducible qualities. In this section, we show that comparison of inverse opals over a wide range of pore sizes is possible despite the use of different methods. Here, the common factor across the methods is the single-crystal domain size of the resulting inverse opal structure (Fig. 4.5). Using FFT analysis, we show that the inverse opals from LPD for templating particles with sizes ≤ 1μm, from EPD for particles ranging in size from above 1 μm and below 5 μm, and from IA for particles with sizes ≥5 μm, all have comparable domain sizes.

4.4.1 Quality of FFT Analysis

The advantage of the FFT analysis method used for Figure 4.5 is that it is a cost-effective way to quantify the crystallinity of an ordered structure from an SEM or optical micrograph in the absence of other tools such as XRD or spectroscopy. The analysis of reciprocal space compresses the information of real space images by looking at the spatial periodicities. As a result, it gives quantitative information on domain distribution, size, and orientation as well as defect density and distribution, all of which are often difficult to judge accurately from SEM images. One caveat of

Fourier analysis performed on 2D images is that it does not include information about the entire 3D structure of the sample, as could be obtained by conventional diffraction methods.[52] However, our analysis of the opals and inverse opals shows that there is a correlation between ordering on the surface and order underneath with the exception of the IA method. Vertical assembly methods, which yield inverse opals with large domains, have less stacking faults compared to the horizontal methods that yield inverse opals with comparatively smaller domains. Overall, we conclude that surface FFT analysis in conjunction with observations on stacking faults is a simple and straightforward diagnostic tool for quantitative evaluation of the quality of multi-layered opals and inverse opals.

4.4.2 Choosing a Method based on Particle Size

Regardless of particle size, the selection criteria for selecting an optimum method for inverse opal fabrication are the same: substrate orientation, particle volume fraction, and colloidal assembly forces. Provided that the template spheres are monodisperse, the success of a colloidal assembly method to yield good opals depends on the balance that it affords for the competing assembly forces that are at play in each method. Our FFT analysis shows that there is a method of choice for each particle size range (Fig. 4.5)

Submicron particles: For particle sizes ≤ 1.0 μm, liquid phase deposition (LPD, Fig. 4.4, A5 and B5) yields the best opals and inverse opals. Considering the similarity in particle assembly conditions between LPD and CoA, their results were expected to be similar. However, co-assembly inverse opals did not have the six-point FFT of their LPD counterparts. Careful analysis of the images revealed that the particles were trapped in a pre-crystallization stage. Most likely, a too high evaporation rate at T = 55±5° arrested the particles in mid-formation. Nonetheless, scrutiny of the co-assembly (CoA) inverse opals shown here revealed that they have the narrowest cracks in comparison to all the inverse opals (Fig. 4.4 E1 - E2). However, higher quality inverse opals were

obtained (not shown) when the particle-to-precursor concentration was optimized.[31] The salient reasons for the success of the LPD method are as follows:

(a) Evaporation of the solvent over long times leads to convection as the major driving force of the LPD assembly process. Owing to their size, submicron particles stay mobile longer as they experience Brownian motion and hence have more time to self-organize into the FCC crystal arrangement.

(b) Upon comparing the results for sedimentation (S) and interfacial assembly (IA) with LPD in Figures 4.5A and 4.5B, it becomes apparent that substrate orientation has an impact, i.e., vertical orientation leads to a larger single-crystal domain size. The vertical orientation in LPD wins out mainly because the convective assembly forces acting on the particles remain uniform throughout the opal assembly process. The convective forces acting in LPD move the particles to the meniscus between the solvent and the substrate, and the substrate is covered with the opaline array as the liquid level falls due to solvent evaporation.[28] In the case of the horizontal sedimentation and IA methods, forces at play for the formation of the initial layer are different from those involved in the formation of successive layers. In sedimentation, for example, gravitational forces push the particles toward the substrate. Short-ranged particle-substrate interactions determine the crystallinity of the first layer and the quality of successive layers. In contrast, in IA, the formation of the initial layer is affected by buoyancy and flotation forces, while subsequent layers are affected mainly by buoyancy forces. The impact of the differences in formation of initial and subsequent layers can be mitigated but not eliminated by very slow evaporation rates (i.e., days instead of hours). However, regardless of the extent of the assembly period, the changing forces for particle assembly result in a structure that is either initially well-packed but prone to stacking faults in subsequent layers (i.e., IA) or initially disordered and more ordered in

subsequent layers (i.e., S). The impact of the stacking faults become evident post-infiltration in form of catastrophically broken inverse opal structures.

(c) In two of the six methods under review, i.e., convective assembly (CA) and electrophoretic deposition (EPD), the magnitude of the force driving the assembly process can be controlled externally. In CA, evaporation-induced convection hastens the particles to the meniscus. Brownian motion, which predominates the motion of submicron particles, leads to an unbalanced crystal growth, resulting in stacking faults. These faults weaken the multilayered inverse opal microstructure, causing cracks to appear with higher spatial frequency. Similarly in EPD, a higher applied voltage causes an increase in the electrophoretic force acting on the particles leading to faster nucleation and crystallization on the substrate. As a result, assembly time is shortened and opal quality is compromised.

Particle sizes above 1 μm and below 5 μm: The FFT results show that EPD is best for particles with diameters in the range from $1 < d < 5$ μm. A comparison of Figure 4.5A with Figure 4.5B suggests that this size range represents the boundary of particle sizes that are strongly affected by gravitational forces. Though particles in this size range show larger single-crystal domains with the horizontal deposition methods for opal formation, the inverse opals of these particle sizes are best formed by electrophoretic deposition. Hence, the decision for substrate orientation can vary with the end goal of opal or inverse opal fabrication. Since Figure 4.5 shows the absolute domain size with respect to particle size, it is notable that the domain sizes of the 2.4 μm particles are smaller in comparison to the 1 μm particles. This discrepancy is a result of the higher degree of polydispersity of the opal template particles: ~5% for 2.4 μm compared to <2% for 0.5 and 1 μm particles. The salient reasons for the success of the EPD method are as follows:

(a) The size of the template particles is an important factor that affects the presence of stacking faults. Gravitational forces acting on particles become significant in this particle size range.

The electric field in EPD lengthens the timescale for nucleation and crystallization by counteracting the effect of gravitational forces and thereby improves the quality of the opals and inverse opals. In contrast, the convective forces in CA in conjunction with the sedimentation tendency of particles in this size range lead to an opal structure that is rife with stacking faults. This disadvantage translates to the inverse opal structure as seen in Figure 4.4 C3 - E3.

(b) Although the interfacial assembly method is optimized for the high-particle volume fraction of 8%, it is the inverse opals from EPD that prove to be more robust as evidenced by the larger domain size.

Particles ≥ 5 μm: Particle sizes ≥5.0 μm are best assembled into opals by the action of buoyancy forces occurring in interfacial assembly. Owing to their size and weight, these particles require more energy to stay mobile in the solution, such as density matching and/or ultrasonication. It has been shown that enhanced (20%) ordering of colloid particles can be achieved via particle settling under ultrasonication.[97] However, the inverse opal counterparts do not fare as well. In Figure 4.4 D2 and E2, the top of the structure is intact while the layers underneath are broken. The reason for the poor inverse opal quality is likely the mismatch between the packing of the initial layer and subsequent layers (see above). This discrepancy is exacerbated during precursor infiltration and additionally due to shrinkage during calcination. EPD with a density-matched electrolyte or a horizontal substrate orientation are other options for assembly of particles with d ≥ 5.0 μm.

Figure 4.5B can be used for the preparation of either (i) inverse opal electrode structures of constant pore size, but varying single-domain size or (ii) electrodes with comparable single-domain size, but varying pore size. As a result, the effect of single-domain size and pore size on electron diffusion, electron lifetime, and trap density can be studied independently, leading to a better understanding of the factors influencing cell efficiency in the presence of electrolytes of varying

viscosity. As long as polystyrene particles are used as templating particles, the trends displayed in Figure 4.5 should be applicable to other infiltrating precursors such as ZnO and MnO_2.

4.5 Chapter Summary

The effect of particle size on inverse opal TiO_2 electrode quality is studied, using a selection of methods that employ gravitational, buoyancy, convective/immersion, and electrophoretic forces. Our study shows that inverse-opal TiO_2 electrodes with pore sizes ranging from the submicron to the micron range can be prepared and compared despite the use of different colloidal assembly methods, opening up the systematic electrochemical study of such electrodes.

Using the same fabrication materials (polystyrene latex, titania precursor) and conditions (aqueous stock solutions), only parameters such the particle size and assembly method are varied. The experimental parameters themselves allow comparison based on changes in particle volume fraction, temperature, and precursor viscosity. The resulting opals and inverse opals are optically characterized by scanning electron microscopy. Fast Fourier transforms of the micrographs provide quantitative measurements of the quality of both the opals and the inverse opals.

Our analysis shows that in addition to monodispersity and slow crystal growth,[78,87] assembly forces and particle size are important for selecting a method for fabricating high quality inverse opals. Our FFT results identify the methods that can yield comparable domain sizes with variable pore sizes. In the case of particle sizes ≤ 1.0 μm, our results confirm what is generally reported in the literature, i.e., good quality opals yield large-area defect-free inverse opals. Among the methods studied, liquid phase deposition (LPD) is the best for particles sizes ≤ 1.0 μm. The results also show that inverse opals by co-assembly (CoA) could potentially be better than inverse opals by LPD, provided the particle-to-precursor ratio and temperature are optimized. For particles sizes >1.0 μm, the probability of a mismatch in the orientation of successive layers is

higher. Consequently, the best inverse opals are made from opals with the least stacking faults. Electrophoretic deposition (EPD) is the best method for assembling particles ranging from above 1.0 μm to below 5.0 μm. Our results further show that interfacial assembly coupled with ultrasonication is the best way to make monolayers of particles ≥ 5.0 μm. Electrophoretic deposition or co-assembly, coupled with density matching emerges as a potential method for fabricating multilayered opals from particles with d ≥ 5.0 μm. Using the data summarized in Figure 4.5, one can start to explore the electrochemical properties of inverse opal TiO_2 electrodes as discussed in Chapter 5.

5. Electrochemical Investigation of Titania Inverse Opal Electrodes

While the interconnected porosity of the inverse opal architecture has its advantages, the distribution and density of surface traps in these structures have not been characterized. In this Chapter, we use chronoamperometry (CA) to determine the density of surface traps in TiO_2 electrodes, both with inverse opal (IO) and nanoparticle (NP) structures. TiO_2 is chosen as the electrode material because it is a prototypical metal oxide that has been explored in most electrochemical cells as discussed in Chapter 2. Furthermore, electrochemical impedance spectroscopy (EIS) is used to determine the effect of the surface traps on electrode performance. The results presented below show that both the ordered structure and the pore size of the inverse opals have an effect on electron transport through the TiO_2 electrode. The information provided by this study will allow the intelligent design of new electrodes that can be utilized in a variety of electrochemical cells.

5.1 Introduction

Electrochemical systems, such as batteries,[98] fuel cells,[99] capacitors,[69,100] and dye-sensitized solar cells (DSSCs),[66,101-103] are intensely studied nowadays because of their potential in energy storage and energy generation. Porous electrodes are especially beneficial for such systems because they provide a large contact area between the electrode and the electrolyte, thus reducing the kinetic and mass-transfer resistances to electron transfer. Conventional porous electrodes consist of a disordered network of nanoparticles that are sintered together. Nanoporous electrodes are preferred because of their large internal surface area and their easy fabrication. Often, synthesis only involves spreading a mixture of crystalline nanoparticles and a binder upon the

desired substrate. However, there is a downside to these nanoparticle systems in that they display a significant number of surface states. These surface states, formed due to the abrupt termination of the crystal, are dangling bonds that are electronically-active. Depending on their density and energy distribution, these active sites tend to affect electron transfer reactions that occur at the particle surface.[104-107] The presence of surface states in electrochemical systems is important as they are involved in charge trapping and recombination processes, both of which affect the efficiency of the electrochemical cell.

The inverse opals studied in this Thesis have an ordered structure that displays high porosity (74%) due to the close-packed arrangement of pores. Fabrication of these structures is often more time and labor-intensive (see Chapter 4). Despite the more complex fabrication requirements, inverse opal electrodes surpass nanoporous electrodes in terms of electrolyte accessibility. In nanoporous electrodes, ionic diffusion often becomes the rate-limiting step among the electron transfer processes due to hindrance by the electrode's nanoporosity and tortuosity. Kim et al.[100] has shown that the inverse opal structure enables better charge-discharge capability compared to a disordered porous matrix as a result of better ionic conduction. The interest in alternative electrolytes for DSSCs, that are more viscous and less volatile,[68] has also led to a renewed interest in inverse opal electrode structures. Once again, the open, porous structure of the inverse opal enables enhanced diffusion of electrolyte ions into the electrode. The infiltration of a viscous electrolyte into a nanoparticle structure can be problematic due to incomplete wetting of the structure, which may increase recombination due to a reduced electrode-electrolyte interface.

5.2 Experimental Details

Materials: Inverse opals of three sizes are prepared from colloidal suspensions of sulfate-terminated polystyrene particles (PS) purchased from Invitrogen (IDC Latex). The co-assembly[88] method schematically shown in Figure 5.1A has been shown to be best for fabricating inverse opals

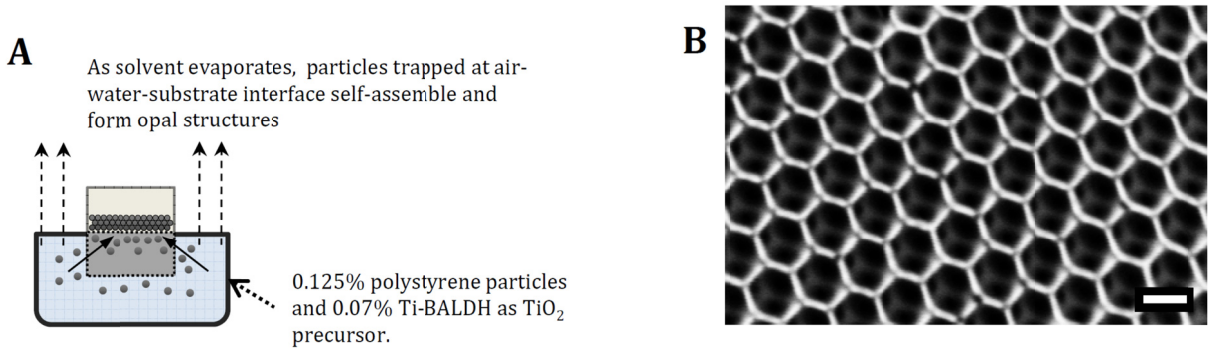

Figure 5.1 (A) Schematic of inverse opal fabrication by co-assembly. (B) SEM image of inverse opal prepared by co-assembly with a template size of 500 nm. Scale bar is 300 nm.

of comparable size and quality, from particles less than 1 μm in size (see Chapter 4).[108] Accordingly, inverse opals with pore sizes in the range of 100 nm to 1.0 μm (IO0.1, IO0.5, and IO1.0) are fabricated using a 10% aqueous solution of titanium (IV) bis-ammonium lactate dihydroxide (Ti-BALDH, 50% aqueous solution, Sigma-Aldrich) as the precursor. Figure 5.1B shows an SEM image of an inverse opal prepared via co-assembly using a 0.5 μm template. The nanoparticle (NP) electrode is prepared by doctor-blading a mixture of polyethylene glycol and Degussa P25 TiO_2 powder (25 nm) onto the substrate. All samples are prepared on 1"×1" fluorine-doped tin oxide (FTO, Pilkington TEC7, 10 ohms/sq.) substrates. Finally, the infiltrated opal templates and the nanoporous electrode are sintered in a temperature-controlled furnace (Barnstead Thermolyne 1400) at 450 °C overnight.

The surface area of the inverse opal electrodes is calculated assuming close-packed pores (74% porosity), with the pore size ~30% smaller than the template PS particles.[92-94] The surface area of the nanoporous electrode is calculated based on a particle size of 25 nm (Degussa P25) and 55% porosity.[109] The thickness of the electrodes is measured using SEM. The characteristic values of all electrodes under study are summarized in Table 5.1.

Table 5.1 Characteristic values of porous TiO2 electrodes with inverse opal (IO) and nanoparticle (NP) structure.

	Polystyrene Particle Diameter[a] *d*	**Film Thickness[b] *t***	**Geometric Surface Area[c] *A***	**Approx. Porosity[d] *ν***	**Electrode-Electrolyte Interfacial Surface Area,[e] *SA***	**Surface Area / Volume**
	[μm]	[μm]	[cm^2]	[%]	[cm^2]	[cm^{-1}]
IO0.1	0.1	0.4±0.1	1.70	74	45.29	6×10^5
IO0.5	0.5	2.1±0.05	1.12	74	29.84	1×10^5
IO1.0	1.0	8.4±0.03	1.56	74	83.12	6×10^4
NP	--	50.0±0.10	2.89	55	15606	1×10^6

a. As reported by Invitrogen (<5% size distribution).
b. determined using SEM.
c. length × width of sample.
d. Close-packing (74%) assumed for IO samples. NP Porosity from literature (see text).
e. $A = \frac{3*Vtotal*(1-\nu)}{\text{particle radius}}$, V_{total}=Pore Volume. ν=porosity

Methods: All electrochemical data is generated using a Gamry Reference 600. Chrono-amperometry (CA) experiments are done to study the surface trap distribution in the TiO_2 electrodes. Each sample is analyzed in a three-electrode setup, with a blank FTO electrode as the counter electrode and saturated calomel (SCE) as the reference electrode. The distance between the three electrodes is kept constant in all experiments at 0.5 mm. The electrolyte is partially deionized water (resistivity of 1 MΩ) , adjusted to a pH of 1.9 ± 0.1 by addition of H_2SO_4 (Fisher Scientific). Prior to each potential step, the TiO_2 electrode is held at 1 V (vs. SCE) for five minutes to equilibrate the conditions at the electrode/electrolyte interface. The potential is stepped from 0.5 to –0.5 V, which is the flatband potential within nanostructured TiO_2 in an aqueous pH 2 electrolyte.[110] The temporal trends of the transient current following a potential step are measured thrice for each electrode.

Electrochemical Impedance Spectroscopy (EIS) is done to probe each electrode's ability to transport electrons. A 10 mV AC perturbation is superimposed over a DC signal, which is varied in

the range of 0.5 to −0.5V. The electrode is allowed to equilibrate for 5 minutes at the chosen DC potential before application of the perturbation. Measurements are repeated thrice for each electrode.

Characterization: The charge accumulated on each electrode is calculated by integrating the area under the transient current curves obtained by CA for each potential step. The capacitive current, i_c, involved in the accumulation at the surface follows the discharging characteristic of a common RC circuit, Eq. 5.1:

$$i_c = \frac{\Delta\varphi}{R} e^{-t/RC_d} \qquad \textit{Eq. 5.1}$$

where $\Delta\varphi$ is the step change in potential, R is the electrode resistance, t is time period over which charges accumulate at the electrode surface, and C_d is the double-layer capacitance. The response time, $\tau = RC_d$, is estimated by fitting the CA plots using Eq. 5.1 (Chapter 3, Fig. 3.8). Typically, it takes as long as 5τ to completely (>99%) discharge a capacitor. Using this information, the time period of the CA experiment was set to 10 s, which is much longer than 0.01 s ($=5\tau$) determined from the RC_d numbers.

Chronoamperometry measures the charge accumulated at the electrode-electrolyte interface. With each step change in the potential, electrons are injected into the TiO_2 electrode leading to a change in the Fermi level. The flatband potential (V_{FB}) of a nanocrystalline TiO_2 electrode is known to be dependent on the pH of the aqueous electrolyte that is used (Eq. 5.2):[111]

$$V_{FB} = -- 0.400 - 0.06pH \text{ (V vs. SCE)} \qquad \textit{Eq.5.2}$$

By this equation, the flatband potential of the TiO_2 electrodes in this study is -0.52V.[110] The varying amount of charge in the bulk of the porous structure must obey the local electroneutrality constraint, i.e., the electrons accumulated in the TiO_2 electrodes are mirrored by H^+ ions in the

electrolyte. Hence, the transient current observed with each potential jump positive of V_{FB} corresponds to filling a slice of surface traps at this energy.[103] An exponential dependence of charge density (C_μ^{traps}) on the applied potential (E), is commonly observed, and has been interpreted as evidence of electron trapping, Eq. 5.3.[53]

$$C_\mu^{traps} = \frac{N_L q^2}{k_B T_0} \exp\left[\frac{E - E_C}{k_B T_0}\right] \qquad \text{Eq. 5.3}$$

The EIS Bode plots are fitted with equivalent circuits using the Simplex algorithm provided by Gamry software. Impedance data for a blank FTO electrode is modeled using the equivalent circuit shown in Figure 5.2A, and is used to determine the extent of charge accumulation (unencumbered by TiO_2 presence) at the FTO electrode and any other uncompensated resistances in the cell. The equivalent circuit in Figure 5.2A describes the FTO/electrolyte interface with a resistor-constant phase element ($R_p2||Q_o2$) combination (dashed line), which is in series with the uncompensated resistance (R_u). The fit of this equivalent circuit (Appendix A, Table A.1) shows that the exponent ($a2$) of the constant phase element (CPE) is close to 1, which implies that it behaves as a true

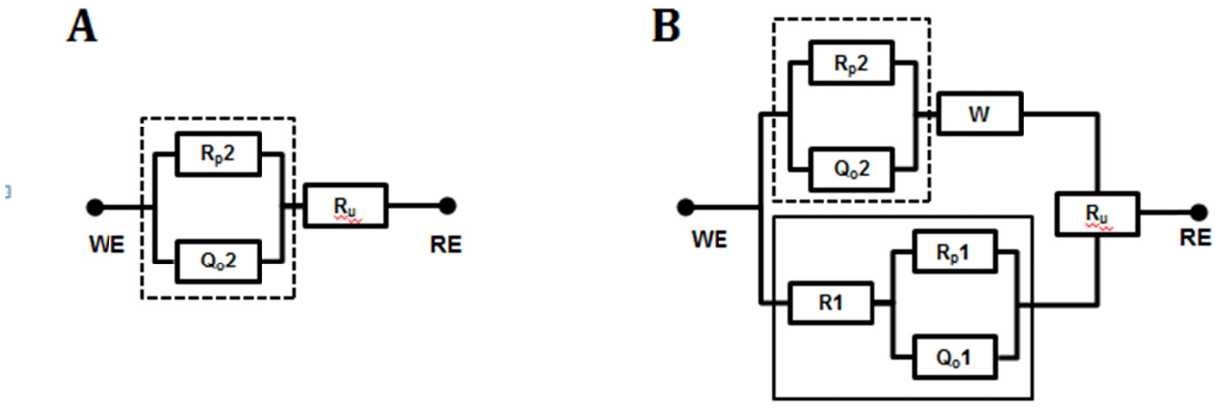

Figure 5.2 Equivalent Circuits for (A) bare FTO electrode, and (B) inverse opal and nanoparticle TiO2 electrodes. Circuits represent the electrochemical cell between the working electrode (WE) and the reference electrode (RE, Satd. Calomel). Ru = resistance from the solution and other electrical contacts. R_p2 = charge-transfer resistance. Q_o2 = capacitance of solution ions at FTO electrode. Parallel combination of R_p2 and Q_o2 [dashed line] represents the FTO/electrolyte interface. $R1$ = TiO_2 network resistance. R_p1 = charge transfer resistance. Q_o1 = capacitance at TiO_2 surface. Parallel combination of R_p1 and Q_o1 [solid line] represents the TiO_2/electrolyte interface.

capacitor (CPE Impedance: $Z = Q_o(j\omega)^{a2}$ = Capacitor Impedance, if $a2 = 1$) The TiO_2-coated FTO electrodes are modeled using the modified equivalent circuit shown in Figure 5.2B, where the FTO/electrolyte interface (dashed line) and the TiO_2/electrolyte interface (solid line) are placed in parallel since the electrolyte has access to both interfaces. The FTO/electrolyte interface, $R_p2||Q_o2$, is placed in series with a diffusion element (W) to describe the ionic diffusion through the porous TiO_2 network to the bare FTO electrode. The TiO_2-electrolyte circuit part comprises a resistor ($R1$) in series with another $R_p1||Q_o1$ combination (solid line). This equivalent circuit section is chosen to describe electron transport in the TiO_2 network ($R1$) and electron transfer at the TiO_2/electrolyte interface ($R_p1||Q_o1$). Fitting parameters for all four TiO_2 electrodes are provided in Appendix A (Table A.1).

5.3 Results

In this section, the electrochemical behavior of three inverse opal electrodes (IO0.1, IO0.5, and IO1.0) is analyzed as a function of pore size and subsequently compared to that of a porous

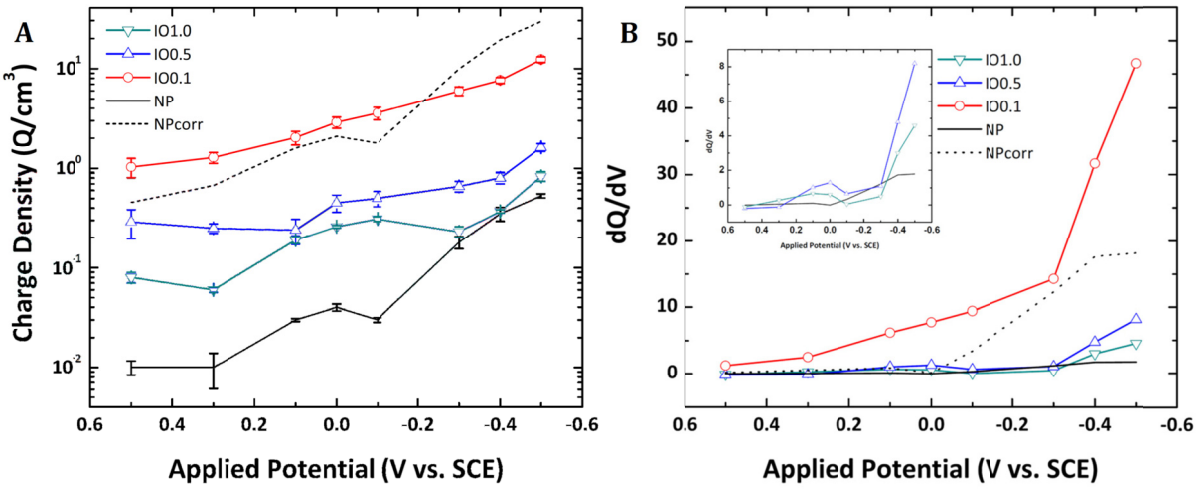

Figure 5.3 Chronoamperometry (CA) measurements for IO0.1[○], IO0.5[Δ], IO1.0 [∇], and NP [––] measured at pH = 1.9 ± 0.1. NPcorr [---] represents interface-corrected NP measurements (see text). (A) Charge density as a function of applied potential. Error bars represent average of three measurements from each electrode. (B) Surface Trap Density computed from the derivative of charge density, dQ/dV. (Inset) Expanded view of IO0.5, IO1.0, and NP surface trap densities.

electrode comprised of a randomly-connected network of TiO_2 nanoparticles (NP) through characterization with chronoamperometry (CA) for trap density determination and electrochemical impedance spectroscopy (EIS) for elucidation of the electron transport behavior.

Figure 5.3 summarizes the results of the CA measurements by plotting charge accumulation (Q/cm^3) and surface trap density as a function of the applied potential for the three inverse opals and the nanoporous electrode. Figure 5.3A shows that the charge density increases exponentially with an increase in the negative applied potential for all four electrodes. Among the inverse opals, IO0.1 (∇) shows the largest charge density, with the charge density decreasing as the pore size increases. The NP electrode (solid line) exhibits the lowest charge density of all electrodes. NPcorr (dotted line) represents the charge density of the NP electrode that is adjusted by a factor of 1/55 to reflect the decreased accessibility of the electrolyte to the NP electrode. Figure 5.3B plots the surface trap density as a function of applied potential for the four electrodes. It is calculated as the derivative of the charge density shown in Figure 5.3A. Among the inverse opals, the majority of the traps lie in the potential region more negative than −0.3 V. An additional small peak near 0 V is seen for the inverse opal electrodes and is most discernible in the 0.5 and 1.0 μm samples (Fig. 5.3B, inset). The majority of the traps in the NP electrode lies in the potential region of 0 to −0.4 V, and remains constant beyond −0.4 V (Fig. 5.3B, inset). Additional CA experiments shown in Figure 5.4, performed at a pH of 13 for IO0.1, IO0.5, IO1.0, and NP as well as two

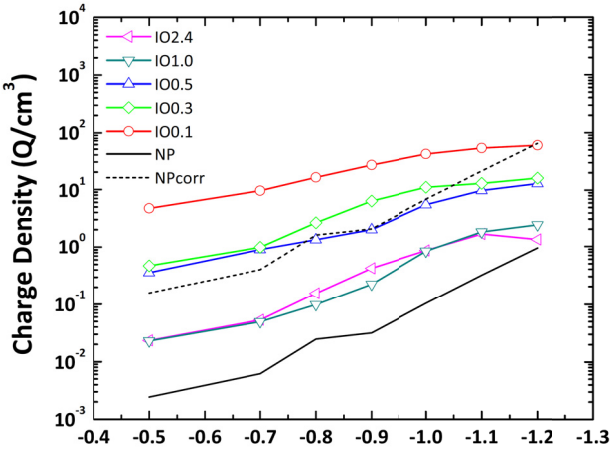

Figure 5.4 Charge density as a function of applied potential for IO0.1[○], IO0.5[Δ], IO1.0 [∇], and NP [–] measured at pH = 13. NPcorr [---] represents interface-corrected NP measurements (see text).

additional IO electrodes (IO0.3 and IO2.4) reveal that their surface trap density trends mimic those observed at pH 2.

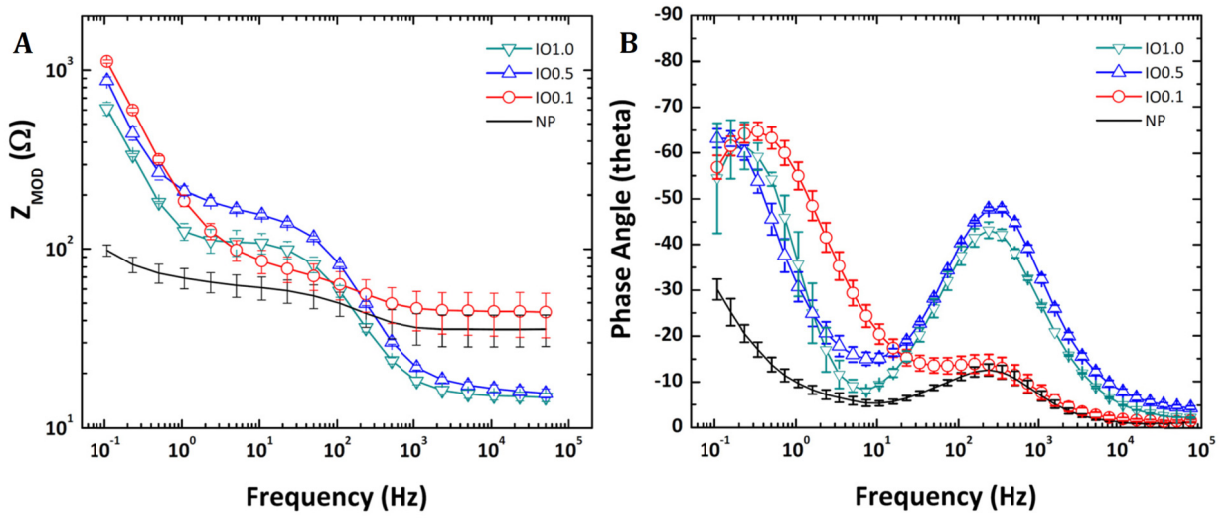

Figure 5.5 Electrochemical Impedance Spectroscopy (EIS) measurements for IO0.1 [○], IO0.5 [Δ], IO1.0 [∇], and NP [––] at VDC = -0.5V. (A) Bode Impedance Plot showing Zmod (impedance, Ω) versus frequency (Hz). (B) Bode phase plot graphing phase lag versus frequency. Error bars represent one standard deviation obtained from three measurements of each electrode.

Electrochemical impedance spectroscopy is a well-established technique for characterizing electrochemical systems.[42,56,101,112] The Bode impedance plot (Fig. 5.5A) reveals the relationship between frequency and electrode impedance, and helps to separate the coupled kinetics of various electron transfer reactions that occur during the experiment. In the case of the nanostructured electrodes, several simultaneous processes contribute to the response to the AC perturbation: (i) electron transport in the TiO_2 (*R1*), which is influenced by free electron density and surface trap density, (ii) the transfer of electrons to redox species (R_p1) in the electrolyte, (iii) charging of the FTO/electrolyte interface (Q_o2, *W*), and (iv) charging of the TiO_2/electrolyte interface (Q_o1). EIS measurements are interpreted through fitting with the equivalent circuits shown in Figure 5.2.

Figure 5.5 depicts the Bode impedance, Z_{MOD}, (Fig. 5.5A) and phase angle (Fig.5.5B) plots obtained from EIS experiments at a DC voltage of −0.5V. Similar plots are observed at other

potentials in the range tested (0.5 to −0.5 V). The Bode plot depicts the impedance over a wide frequency range (10^{-1}-10^{5}), whereas the phase angle plot represents the lag in current response to the AC perturbation for the same frequency range. Impedance at the high frequencies (>10^{4} Hz) is associated with the series resistance of the electrolyte (R_u) and electric contacts (*R1*) in an electrochemical cell (Fig. 5.2). The phase angle plot (Fig. 5.5B) provides confirmation of this fact with a phase angle of 0° at high frequencies. With decreasing frequency (10^{1}-10^{4} Hz), the resistor-CPE combinations ($R_p1||Q_o1$ and $R_p2||Q_o2$) increasingly contribute to the overall impedance. At the lowest frequencies (<10^{1} Hz), the impedance due to ionic accumulation (*W*, Q_o1, and Q_o2) at the surface is the largest contributor to the impedance, and the influence of the circuit's resistors (*R1*, R_p1, and R_p2) vanishes. The phase angle plot (Fig. 5.5B) corroborates this by showing an angle close to 70° at frequencies below 10^{0} Hz. The phase angle values in the low-frequency range signify ionic diffusion away from the electrode before the AC signal changes direction.

The high-frequency region in Figure 5.5A shows that the impedance (Z_{MOD}) of the inverse opal electrodes decreases with increasing pore size, while the impedance of the NP electrode lies between that of the IO0.1 electrode and the larger electrodes. In the mid-frequency range, where both resistors and capacitors contribute to the impedance, i.e., the charge-transfer region, the inverse opal electrodes show higher impedance than the NP electrode. The peak in the phase angle (Fig. 5.5 B) occurs at almost the same frequency (~250 Hz) for all four electrodes studied, but with different phase angle values. The IO0.5 and IO1.0 electrodes have comparable values (43 vs. 47°), which are higher than the values of the IO0.1 and NP electrodes (~13°). The inverse opal electrodes continue to show higher impedance in the low-frequency region, with a peak in the phase angle at 0.4 (IO0.1), 0.2 (IO0.5), and 0.1 Hz (IO1.0), while that of the NP electrode is below 0.1 Hz. For each electrode, the error bars for the measurements represent one standard deviation calculated from multiple measurements of each electrode.

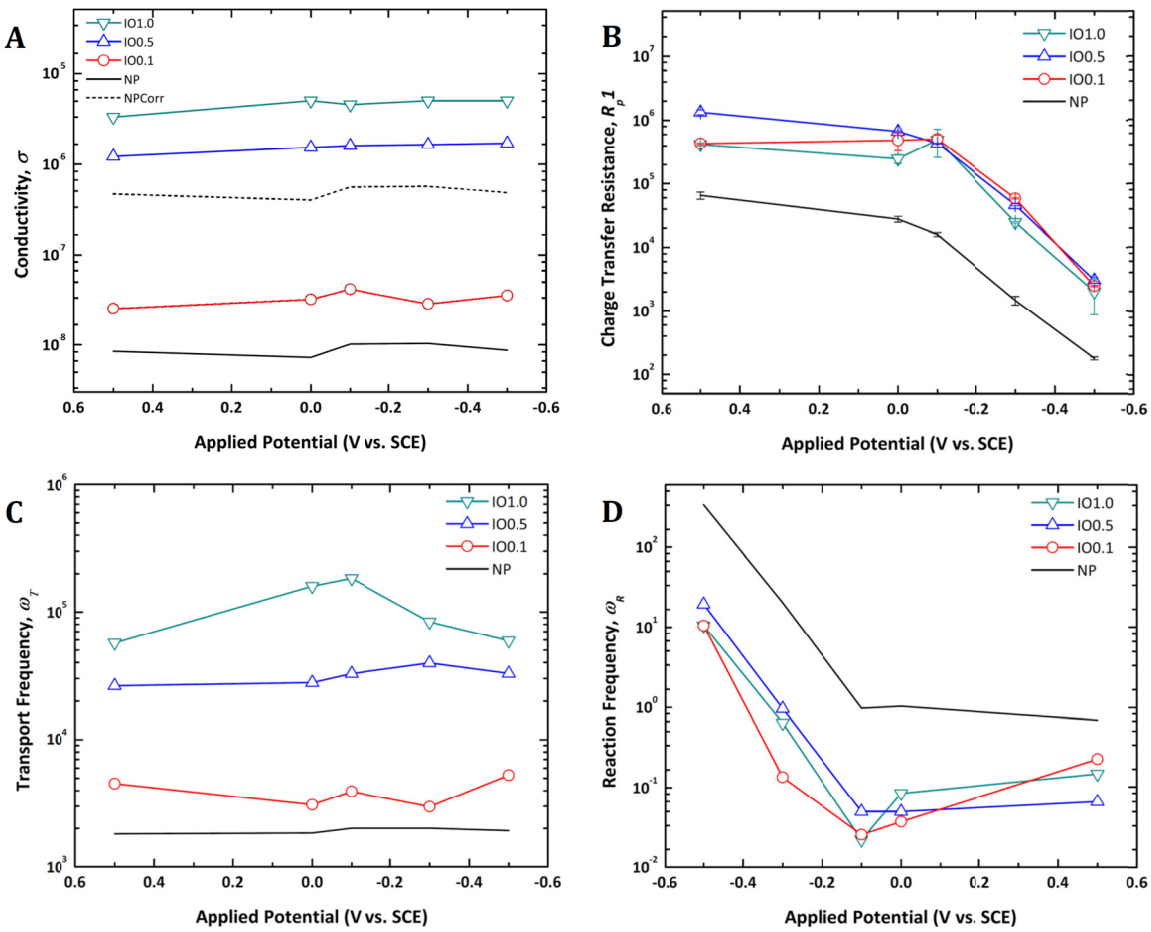

Figure 5.6 Comparison of performance of inverse opal TiO2 electrodes [IO0.1 ○, IO0.5 Δ, IO1.0 ∇] and nanoporous electrode [NP –, NPcorr ---]: (A) Conductivity, σ, (B) Charge-Transfer Resistance, Rp1, (C) Transport Frequency, ω_T, and (D) Reaction Frequency, ω_R, as a function of applied potential.

From the equivalent circuits, three parameters are used to completely define the TiO_2 network and the TiO_2/electrolyte interface: *R1*, R_p1, and Q_o1. Using these parameters, three quantities are calculated as metrics for electrode performance: conductivity (σ), transport frequency (ω_T), and reaction frequency (ω_R). These quantities have been used in the past to describe electron transfer reactions in disordered, nanoparticle TiO_2 electrodes.[57] We use them here to enable a comparison of nanoporous electrodes with ordered, inverse opal electrodes.

The high-frequency impedance of the TiO_2 electrodes reveals the resistance (*R1*) of the interconnected TiO_2 nanoparticle network. The conductivity, σ, is inversely proportional to this

measured resistance, Eq. 5.4, and remains essentially constant over the entire range of applied potentials.

$$\sigma = \frac{L}{R1*A*(1-\nu)} \qquad \textit{Eq. 5.4}$$

Conductivity in the inverse opal electrodes (○ - IO0.1, Δ - IO0.5, and ∇ - IO1.0) is independent of the applied potential, but shows a dependence on the pore size, i.e., conductivity increases with increasing pore size (Fig. 5.6A, Table 5.2). The nanoporous electrode (solid line) shows a lower conductivity than all the IO electrodes. The charge transfer resistance, R_p1 (Fig. 5.6B, Table 5.2), decreases exponentially with increasing negative applied potential, but shows no pore-size dependence. The inverse opal electrodes have a higher charge transfer resistance compared to the NP electrode. The double-layer capacitance, *C1* (Table 5.2) at the TiO_2 surface (determined from Q_o1) depends only weakly on the applied potential. As the potential becomes more negative, the values for the exponent, *a1* (Appendix A, Table A.1), deviate from 1 by as much as 20%. Finally, the effect of electrode morphology on its ability to conduct electrons is determined by computing the transport frequency, ω_T, and the reaction frequency, ω_R, (Figs. 5.6C and 5.6D, Table 5.2). The transport frequency, ω_T, measures the transport of electrons through the interconnected TiO_2 network and is calculated according to Eq. 5.5.

$$\omega_T = \left(\frac{1}{R1*Q_o1}\right)^{1/a1} \qquad \textit{Eq. 5.5}$$

Figure 5.6C shows that (i) ω_T of the inverse opal electrodes increases with increasing pore size, and (ii) the NP electrode has the lowest ω_T. The reaction frequency, ω_R, measures electron transfer across the electrode/electrolyte interface and is calculated using Eq. 5.6.

$$\omega_R = \left(\frac{1}{R_p\ 1 * Q_o 1}\right)^{1/a1} \qquad \textit{Eq. 5.6}$$

The inverse opal electrodes have comparable values for ω_R, which are lower than the value calculated for the NP electrode.

Table 5.2 summarizes the values for the circuit elements (*R1*, R_p1, and *C1*) describing the TiO_2/electrolyte interface (Fig. 5.2, solid line) as determined by fitting of the EIS measurements with the equivalent circuits shown in Figure 5.2 as well as σ, ω_T, and ω_R derived from them (see below) and shown in Figure 5.6. The uncompensated resistance (R_u) is a sum of the solution resistance and the resistance of the FTO electrode. This value, R_u = 14 ± 3 Ω, is determined by measuring the high-frequency impedance of a bare FTO electrode (blank).

Table 5.2 Conductivity (σ), Transport Frequency (ωT), and Reaction Frequency (ωR) for TiO2 electrodes and EIS fitting parameters from which they are derived (R1, Rp1, C1).

	***V* vs. SCE**	***R1***	***R_p1***	***C1***	***σ/ω_T***	***ω_R***
	[V]	**[Ω]**	**[Ω]**	**[μF/ cm²]**		**[Hz]**
IO0.1	0.5	37	433300	0.143	$\sigma = 3.26\times10^{-8}$ S.cm ω_T = 3334 Hz	0.23
	0.0	29	484700	0.775		0.04
	-0.1	22	510400	1.072		0.03
	-0.3	32	58817	1.770		0.13
	-0.5	26	2413	0.902		6.44
IO0.5	0.5	6	1342667	0.048	$\sigma = 1.55\times10^{-6}$ S.cm ω_T = 31868 Hz	0.07
	0.0	5	669400	0.127		0.05
	-0.1	4	434533	0.196		0.05
	-0.3	4	46433	0.095		0.96
	-0.5	4	3056	0.072		19.33
IO1.0	0.5	3	418467	0.012	$\sigma = 4.62\times10^{-6}$ S.cm ω_T = 108762 Hz	0.15
	0.0	2	247900	0.036		0.09
	-0.1	2	492867	0.070		0.02
	-0.3	2	24845	0.048		0.64
	-0.5	2	2014	0.036		10.43
NP	0.5	38	65590	0.002	$\sigma = 9.00\times10^{-9}$ S.cm ω_T = 1923 Hz	0.69
	0.0	44	27927	0.002		1.03
	-0.1	31	15978	0.004		0.97
	-0.3	31	1476	0.002		20.28
	-0.5	37	178	0.001		337.7

5.4 Discussion

The aim of this study is to elucidate the effects of electrode morphology on conductivity of and electron recombination within a TiO_2 electrode. We have synthesized and studied two types of electrode morphologies: (i) an interconnected, ordered 3DOM structure known as inverse opals with uniform pore size (IO0.1, IO0.5, and IO1.0), and (ii) a disordered, random structure comprised of nanoparticles that are sintered together (NP). Inverse opals are unique in that the surface area per unit volume, and consequently the surface trap density can be controlled through the size of the template used. Both types of electrodes contain nanoparticles that are sintered together, and share common features of a large surface area and a high degree of porosity. Due to the large surface area of such nanostructured electrodes, surface traps play a crucial part in the kinetics of electron transfer. In order to gauge the effect of surface traps, we have quantified them by chronoamperometry (CA). Subsequently, the effects on electrode performance, i.e., conductivity and recombination, are studied using electrochemical impedance spectroscopy (EIS). In this section, we discuss CA and EIS results and outline the differences and similarities between inverse opal electrodes and an electrode comprised of nanoparticles.

The trend observed for the inverse opal electrodes is that a smaller pore size translates to a higher surface trap density. These effects of these surface traps on electron movement are reflected by the conductivity, transport frequency, and reaction frequency of the TiO_2 electrodes.

The conductivity of the inverse opal electrodes is inversely proportional to the surface trap density. An electrode with high surface trap density slows down electron transport across the electrode due to a higher incidence of electron trapping. By comparing Equations. 5.4 and 5.5, it is clear that electrode conductivity and transport frequency are related. The transport frequency, ω_T, defines how quickly electrons move within the TiO_2 network. Since electron transport is known to be trap-limited, ω_T is also expected to show a dependence on trap density. Figure 5.6C shows that

the transport frequency of the inverse opal electrodes increases with increasing pore size. Since the trap density (Fig. 5.3B) of the inverse opal electrodes reflects the surface area per unit volume, this trend is expected. Normalized by the geometry of the electrode, Figure 5.6A shows that inverse opals exhibit increasing conductivity with increasing pore size.

The reaction frequency, ω_R, is the performance metric used to assess how quickly electrons that are injected into the TiO_2 matrix are lost to the electrolyte. This parameter is by definition related to recombination. Low ω_R values indicate a low incidence of recombination. Figure 5.6D shows that the reaction frequency of all electrodes decreases with increasing negative applied potential. As the applied potential becomes more negative, a smaller portion of the injected electrons are entrained in surface traps. Consequently, electron transfer into the electrolyte becomes more likely. Eq. 5.6 shows that ω_R is inversely proportional to the charge transfer resistance, R_p1. Further, Figure 5.6D shows that ω_R is constant across the different pore sizes, which implies that it is not a function of surface trap density. By comparing, the ω_R values of the inverse opals and the NP electrode, we can conclude that ω_R is more likely improved due to the higher coordination number, i.e., better contact of the nanoparticles, in the inverse opals. Within the inverse opal morphology, the nanoparticles have a larger coordination number compared to the 55% porous random nanoparticle network (average coordination number = 4).[109]

One point to be noted however is the correlation between trap density and conductivity is different for the NP electrode. The NP electrode has the highest calculated surface area per unit volume (Table 5.1), the lowest charge density (Fig. 5.3A), and the lowest conductivity (Fig. 5.6A) of all four TiO_2 electrodes studied. One would thus expect the nanoporous electrode (with pore size ~14 nm) to have the highest surface trap density and the lowest conductivity. From Figure 5.6A, we see that the NP electrode does indeed have the lowest conductivity. However, Figure 5.3A shows that the NP electrode has the lowest surface trap density as well. It is possible that the NP electrode

has the lowest number of surface traps since it is made from a commercial product, Degussa P25 nanoparticles, which is already crystalline in nature. In contrast, IO electrodes are prepared by sintering a TiO_2 precursor converting it from an amorphous state to a crystalline state. If the sintering conditions are less than optimum, more surface traps may be formed in the IO electrodes. However, since traps interfere with electron mobility within the TiO_2 network, the NP electrode should as a result show the highest conductivity and transport frequency, which it does not. Hence, the reason for this inconsistency must be due to an underestimation of the surface trap density, which is calculated from the accumulated charge (from CA experiments) and the TiO_2/electrolyte interfacial area. The interfacial surface area of the NP electrode is calculated based on the nanoparticle size (25 nm) and the estimated porosity (55%) of the electrode.[109] The abovementioned inconsistency is rectified if we realize that not *all* of this interfacial surface area is actually in contact with the electrolyte. This observation would then explain why CA underestimates the charge density of the NP electrode. The low frequency range in Figure 5B shows that the NP electrode has the lowest phase angle values, and it peaks at the lowest frequency (<0.1 Hz), which further corroborates the decreased accessibility of the NP electrode interior.

Given that that the testing conditions are the same for all of the electrodes, i.e., the ionic concentration of the electrolyte and electrode potential, it is reasonable to assume that charge accumulated per unit area would also be the same. Figure 5.7 shows the charge accumulated over the calculated interfacial surface area of all of the electrodes. The inverse opal electrodes all lie on the same line, while the NP electrode is shown to have much smaller values. The NP electrode comes into line with the inverse opal electrodes, when its interfacial surface area is adjusted by a factor of 1/55 (dotted line). The actual adjustment factor ranges between 1/35 and 1/85. Using the fact that the conductivity is a pore-size dependent feature, a good estimate for the NP electrode correction factor (pore size ~14 nm) would bring its conductivity close to that of the IO0.1 electrode (pore size ~70 nm). Such a shift in conductivity is achieved when the NP electrode

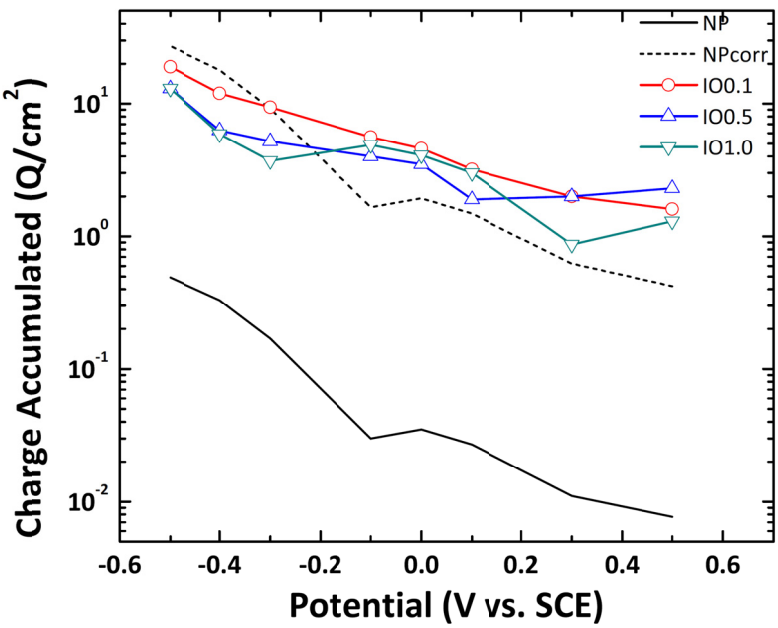

Figure 5.7 Charge accumulated per unit interfacial area. A correction factor of 1/55 adjusts the NP electrode to be in line with the inverse opal electrodes.

electrode/electrolyte interfacial area is adjusted by a factor of 1/55 bringing the two properties of the NP electrode – conductivity and trap density, into agreement with the trends observed for the IO electrodes. The corrected values for the NP electrode, designated NPcorr, are shown in Figures 5.3A and 5.6A (dashed line). Note that R_P1, ω_T, and ω_R plotted in Figures 5.6B-D are obtained from EIS data fitting and do not involve the calculated surface area. A similar correction factor of 1/65 was used for the CA data obtained at pH = 13 (Fig.5.4)

Ionic diffusion has already been shown to be better in inverse opal electrodes.[100] In our system, this advantage is best observed in the Bode phase angle plot (Fig. 5.5B). As discussed above, impedance in the low frequency (<10^1 Hz) region is dominated by diffusion to the less-accessible parts of the electrode. The magnitude of the phase angle (Fig. 5.5B) represents a balance of the diffusion with the RC constant of the electrode. A high phase angle implies that ions travel further away from the interface before the AC signal changes direction. Owing to the openness of the inverse opal structure, these electrodes have a higher phase angle compared to the nanoporous

electrode. The frequency at which the peak in the phase angle appears yields the characteristic timescale (≤ 1 Hz or ≥ 1 s) for ionic diffusion. Figure 5.5B shows that ionic diffusion takes longer in the NP electrode compared to the inverse opal electrodes.

To summarize, inverse opals display higher transport frequency, lower reaction frequency, and enhanced diffusion through the pores. The thick, ordered, and interconnected walls of the inverse opal electrode enables unencumbered movement of electrons. The thicker walls also improve the ion-charge separation at the electrode interface, resulting in reduced incidences of recombination. These two factors, in combination, prove that inverse opals are better electrodes than NP electrodes and offer a pathway for increased electrode efficiency.

The optimum pore size for an electrode is dependent on the application. Electrosorption of ions, or adsorption-related charge, has been shown to be one of the modes of charge storage in electrochemical double layer capacitors (EDLCs).[113] The optimum electrode for this application should have a pore size that is small enough so that the trap density is maximized, but large enough to enable quick charge-discharge cycles. From our data, the optimum pore size would be around 70 nm (IO0.1). The materials chosen to comprise traditional dye-sensitized solar cells enable a near unity photon-to-electron conversion. However, a large part of the photo-injected electrons are lost before being collected by the back electrode. Our results show that inverse opal electrodes are generally less likely to lose their electrons to recombination. Additionally, an inverse opal with large pores has a small trap density, which further diminishes recombination. Inverse opal electrodes with large pores would also be compatible with the newer, more viscous electrolytes due to good contact between electrolyte and electrode and unencumbered ionic diffusion. Most recently, the Braun group[114] reported the successful preparation of inverse opals with a porous backbone, which offers a way to maintain the ordered porosity of the inverse opals and further increase the IO electrode/electrolyte interfacial area.

5.5 Chapter Summary

TiO_2 electrodes with different microstructures are studied to understand its effect on conductivity and recombination. Ordered, well-connected, inverse opal structures are compared with the disordered network of sintered nanoparticles. Chronoamperometry measurements reveal that trap density depends both on the applied potential and on the surface area per unit volume of the TiO_2 electrode. Electrochemical impedance measurements show that the inverse opal electrodes have a higher conductivity, one that is a function of the trap density, and are less likely to lose electrons to recombination. By virtue of their high transport frequency and slow reaction frequency, inverse opals are better electrode structures than nanoporous electrodes. Moreover, an optimum pore size depends strongly on the application the electrode is chosen for.

6. Photoelectrochemical Investigation of Inverse Opal TiO_2 Electrodes

In this chapter, we explore the effect of electrode structure on DSSC performance under indoor lighting conditions. Indoor lighting is less intense and has a mismatched frequency compared to the absorption spectrum of the N719 dye used in commercial DSSCs. The photoelectrochemical characteristics such as open-circuit voltage (V_{OC}), short-circuit current (J_{SC}), and fill factor (FF) as well as the impedance behavior of nanostructured and inverse opal TiO_2 electrodes are determined using photocurrent-voltage, open-circuit voltage decay, and electrochemical impedance spectroscopy measurements as outlined in Chapter 3.

6.1 Introduction

The major benefits of DSSC technology are the use of non-toxic and abundant materials (TiO_2), low capital requirements, and a simpler manufacturing process relative to other PV technologies. These potential benefits have attracted a lot of interest to DSSCs globally. According to market projections by IDTechEx, the market for dye-sensitized solar cells will slowly grow to 290 million dollars by 2023.[14] In order to reach this projection, DSSC technologies have to overcome performance limitations in lifetime and efficiency. On the other hand, the performance gap between DSSCs and amorphous silicon, one of the incumbent technologies, has closed dramatically in recent years, especially with respect to indoor applications. It is thus important to identify the best fitting initial applications for DSSCs, as the ones to target first in order to achieve faster commercialization of DSSCs.

The academic community working in the field of DSSCs has primarily focused on 'efficiency inflation', i.e., reaching the highest efficiency at AM1.5 conditions on tiny cells (~0.3 – 1 cm^2), through the use of wide-spectrum dyes, electrolyte additives, and other improved constituents in the cell.[115] For example the focus of dye-engineering has been to improve absorption in the range above 750 nm to utilize that part of the AM 1.5 spectrum. However, the factors for optimization are different for indoor applications primarily because the indoor light spectrum is less intense (upto 500× less) and very different from that of the outdoors (Fig. 6.1A).[116] Ambient light, primarily fluorescent lighting but also incandescent and LED light, has a significant portion of its spectrum in the 600 nm range and below. Hence, it is possible to use less expensive, easily accessible dyes such as a 1:1:1 mixture of raspberries, hibiscus, and chlorophyll for indoor applications.[117]

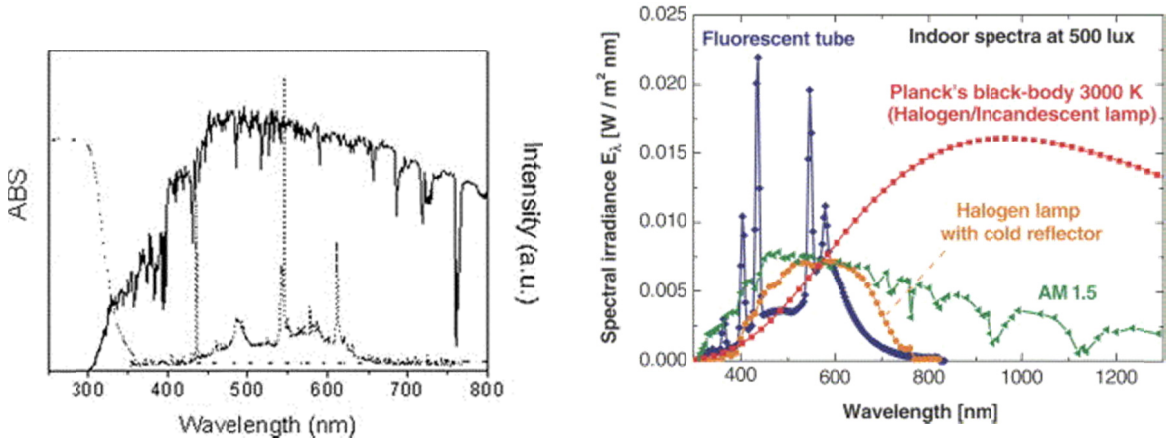

Figure 6.1 (A) Spectra of AM 1.5 light (solid line), fluorescent bulb (dotted line), and absorption spectrum of TiO_2 (dashed line)[116] (B) Measured or simulated spectral distributions at 500 lux of common indoor light sources. Indoor Spectra at 500 lux for different light sources: AM 1.5 (green), Fluorescent tube (blue), Halogen or Incandescent light (red), Halogen lamp with cold reflector (orange).[118]

The indoor performance metric is the power density output (μW/cm^2) of a cell or module at a particular luminance or lux (lumens/m^2) level. There are three categories of indoor lighting: fluorescent, incandescent, and daylight. The fundamental difference between illuminance (lux) and irradiance (W/m^2) is the weighting of the spectral response. Irradiance includes the power from all

wavelengths weighted equally, whereas illuminance weights the power from each wavelength in proportion to the sensitivity of the human eye, which is most sensitive to green light. Figure 6.1B[118] shows the relative spectral irradiance of different indoor light sources at 500 lux. Incandescent lighting matches the AM 1.5 spectrum, while the fluorescent tube spectrum cuts off above 800 nm. Environmental and efficiency considerations have led to the phasing out of incandescent lighting and fluorescent lighting and to a smaller extend LEDs have begun to take its place. Figure 6.2 shows the standard lux values reached at different indoor settings. The typical office lux intensity is between 200-700 lux (3 – 12 W/m^2).

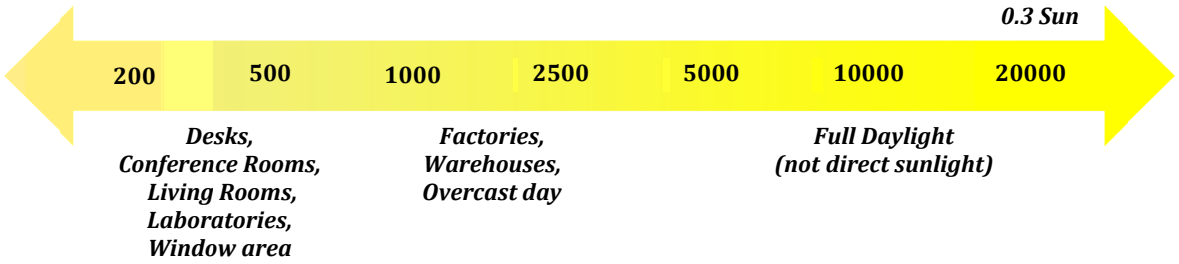

Figure 6.2 Standard lux values of different light settings.

Due to their ability to deliver high efficiencies at low-light conditions, the niche for DSSC technology lies in indoor applications. DSSCs in their current configuration work well in low-daylight conditions mainly because of the I^-/I_3^- redox couple. The electron transfer kinetics for this redox couple is slow, and hence the timescale of recombination is longer and does not compete with dye regeneration. However, in the interest of DSSC commercialization, the I^-/I_3^- redox couple needs to be replaced. If this is done, the kinetic advantage is lost and dye regeneration once again competes with recombination. The high number of traps and low porosity that restrict I_3^- movement may further inhibit progress. In a 2006 paper by Zhu et. al[119] analytic calculations on the effects of surface area on charge transport and recombination in DSSCs showed that the electron diffusion exhibits a power law dependence (corroborated by experiment) on the photoelectron

density. Also it is seen that the electron diffusion coefficient (*D*) decreases with increasing trap density. The calculations predict that for a two-order decrease in photoelectron density, the electron diffusion coefficient decreases by 6 orders of magnitude. This prediction is further supported by the results presented in Chapter 5, which show that the electrode conductivity is dependent on surface-trap density. In other words, an electrode with a high trap density performs poorly in low-light conditions compared to an electrode with a low trap density. The high surface area of the current nanostructured TiO_2 electrode allows the generation of a usable amount of photocurrent. However, the high surface area-to-volume ratio inevitably implies the presence of surface traps, which will remain largely unoccupied at low-light intensities. As was shown in Chapter 5, inverse opal (IO) electrodes have fewer surface traps compared to the nanostructured (NP) electrode and thus are expected to show higher efficiencies at low-light conditions typical for indoor lightening conditions.

6.2 Experimental Details

Materials: Inverse opals of three sizes are prepared from colloidal suspensions of sulfate-terminated polystyrene particles (PS) purchased from Invitrogen (IDC Latex) employing the co-assembly method. [88,108] Accordingly, inverse opals with pore sizes in the range of 100 nm to 1.0 μm (IO0.1, IO0.5, and IO1.0) are fabricated using a 10% aqueous solution of titanium (IV) bis-ammonium lactate dihydroxide (Ti-BALDH, 50% aqueous solution, Sigma-Aldrich) as the precursor. The nanoparticle (NP) electrode is prepared by doctor-blading a mixture of polyethylene glycol and Degussa P25 TiO_2 powder (25 nm) onto the substrate. All samples are prepared on 1"×1" fluorine-doped tin oxide (FTO, Pilkington TEC7, 10 ohms/sq.) substrates. Finally, the infiltrated opal templates and the nanoporous electrode are sintered in a temperature-controlled furnace (Barnstead Thermolyne 1400) at 450 °C overnight. The surface area of the inverse opal electrodes is calculated assuming close-packed pores (74% porosity), with the pore size ~30% smaller than the template PS particles.[92-94] The surface area of the nanoporous electrode is calculated based on a

particle size of 25 nm (Degussa P25) and 55% porosity.[109] The thickness of the electrodes is measured using SEM. The characteristic values of all electrodes under study are summarized in Table 6.1.

Once prepared, the TiO_2 electrodes are placed in a 120°C oven for 30 min to eliminate all traces of water. Following this heat treatment, the electrodes are immersed in a 0.5 mM ethanolic solution of N719 (Di-tetrabutylammonium cis-bis(isothiocyanato)bis(2,2'-bipyridyl-4,4'-dicarboxylato) ruthenium(II), Sigma Aldrich) dye for 24-48 hours, or until the TiO_2 appears completely dyed. Finally, the excess dye is removed via a cursory wash with ethanol.

Table 6.1 Characteristic values of porous TiO_2 electrodes with inverse opal (IO) and nanoparticle (NP) structure.

	Polystyrene Particle Diameter[a] ***d***	Film Thickness[b] ***t***	Geometric Surface Area[c] ***A***	Approx. Porosity[d] ***ν***	Electrode-Electrolyte Interfacial Surface Area,[e] ***SA***
	[μm]	**[μm]**	**[cm²]**	**[%]**	**[cm²]**
IO0.1	0.1	0.8±0.1	2.56	74	136.8
IO0.5	0.5	2.1±0.05	2.56	74	68.2
IO1.0	1.0	4.4±0.03	2.56	74	68.2
NP	--	10.0±0.10	2.56	55	2765

a. As reported by Invitrogen (<5% size distribution).
b. determined using SEM.
c. length × width of sample.
d. Close-packing (74%) assumed for IO samples. NP Porosity from literature (see text).
e. $A = \frac{3*Vtotal*(1-\nu)}{\text{particle radius}}$, V_{total}=Pore Volume. ν=porosity

DSSC-cell: The cell used for photoelectrochemical characterization is a two-electrode cell (Fig.6.3A), where the dyed TiO_2 electrodes (NP and IO) serve as the working electrode and a platinized FTO electrode is the counter electrode. The counter electrode is platinized by depositing 20 nm of platinum using physical vapor deposition, in order to enable the I^-/I_3^- electron transfer between the organic electrolyte (acetonitrile) and the electrode. Fig.6.3B

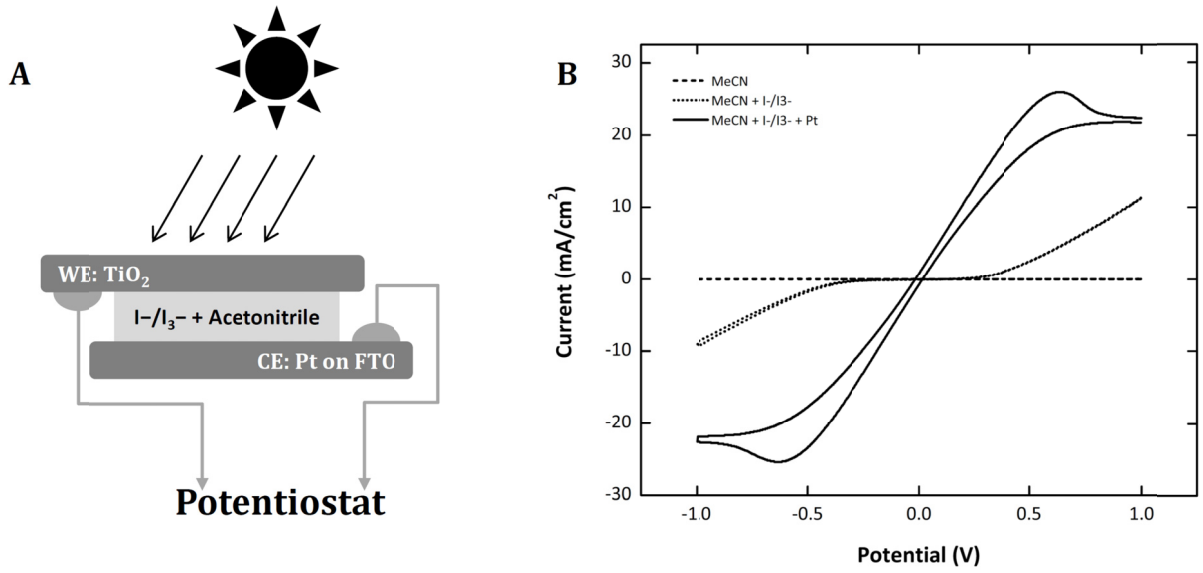

Figure 6.3 Experimental setup for photoelectrochemical tests (A). Cyclic voltammograms showing that Pt enables the I^-/I_3^- electron transfer (B).

shows that the presence of Pt (solid line) increases the current density generated within the electrode. The iodide-triiodide redox pair is dissolved in (0.5/0.05 M) acetonitrile and injected into the space between the two electrodes sealed into a DSSC sandwich cell. Surlyn® (Dupont) is used to seal the cell.

Methods: The DSSC sandwich cell is positioned horizontally as shown in Figure 6.3A with the light source (13 W CFL bulb, 825 lumens) placed at varying distances to modulate the amount of light incident upon the cell. Fluorescent light is chosen since it has been shown that DSSCs effectively absorb it. Another reason is its popularity for home and business use, making it the apt choice to represent indoor illumination. Moreover, the CFL spectrum is very similar to the white LED spectrum, making the experiments reported here relevant for most future types of indoor lighting as well. The performance measurements are carried out inside an opaque box, which allows experiments to be conducted under well-controlled light conditions. The intensity or illuminance of the light source is measured using a lux meter. Photocurrent-voltage (IV) curves are taken at different intensities, and the V_{OC}, J_{SC}, and *FF* are measured. The two electrodes of the assembled

DSSC are connected as follows: TiO_2 electrode is connected to the working electrode lead, Pt-FTO is connected to the counter electrode and reference electrode leads. As the electrolyte leaks from the cell over the course of a week, the cell is refilled with the same solution of electrolyte to maintain uniformity throughout experimentation time period.

Cyclic voltammetry, or its variant Linear Sweep Voltammetry is done to determine the V_{OC}, J_{SC}, and *FF* for each cell. The cell is illuminated for 5 minutes prior to the measurement to allow the cell to stabilize.

The decay of the open circuit voltage is recorded once the illumination is shut off as a way to gauge the recombination trends. The cell is initially illuminated for at least 5 minutes to allow the V_{OC} to stabilize to a constant value. When the illumination is shut off, photoinjected electrons recombine with the I_3^- ions in solution, as it is the only pathway available for relaxation. The V_{OC} is measured until the value equilibrates. Each electrode is tested thrice at each light intensity.

Electrochemical impedance spectroscopy (EIS) is employed to elucidate the electron transfer reactions that occur near the electrode-electrolyte interface. Measurements are done at V_{OC} under various intensities of the CFL bulb by superimposing a 10 mV AC perturbation. The electrodes are allowed to equilibrate for 5 minutes at the V_{OC} before application of the perturbation. Measurements are repeated thrice for each electrode.

6.3 Results

Three inverse opal TiO_2 electrodes of varying pore sizes (0.1, 0.5, and 1.0 μm) and a nanoporous electrode are assembled into the standard DSSC configuration depicted in Figure 6.3A, and illuminated using a 13 W CFL bulb in order to mimic indoor lighting conditions. The physical characteristics of the working electrode for each cell are summarized in Table 6.1. The

photocurrent-voltage curves, electron recombination lifetimes, and interfacial electron dynamics are generated via CV, OCVD, and EIS (see Chapter 3).

Figure 6.4 shows the trends of V_{OC}, J_{SC}, and *FF* of the TiO_2 electrodes at different intensities of indoor lighting. These graphs show a marked difference in their trends at light intensities above 2500 lux. In the following, light intensities less than 2500 lux will be designated as "low-intensity" and intensities higher than 2500 lux are deemed as "high-intensity". The open circuit voltage (Fig. 6.4A) depends on the free electron density (n) within the TiO_2 network according to the equation 6.1,

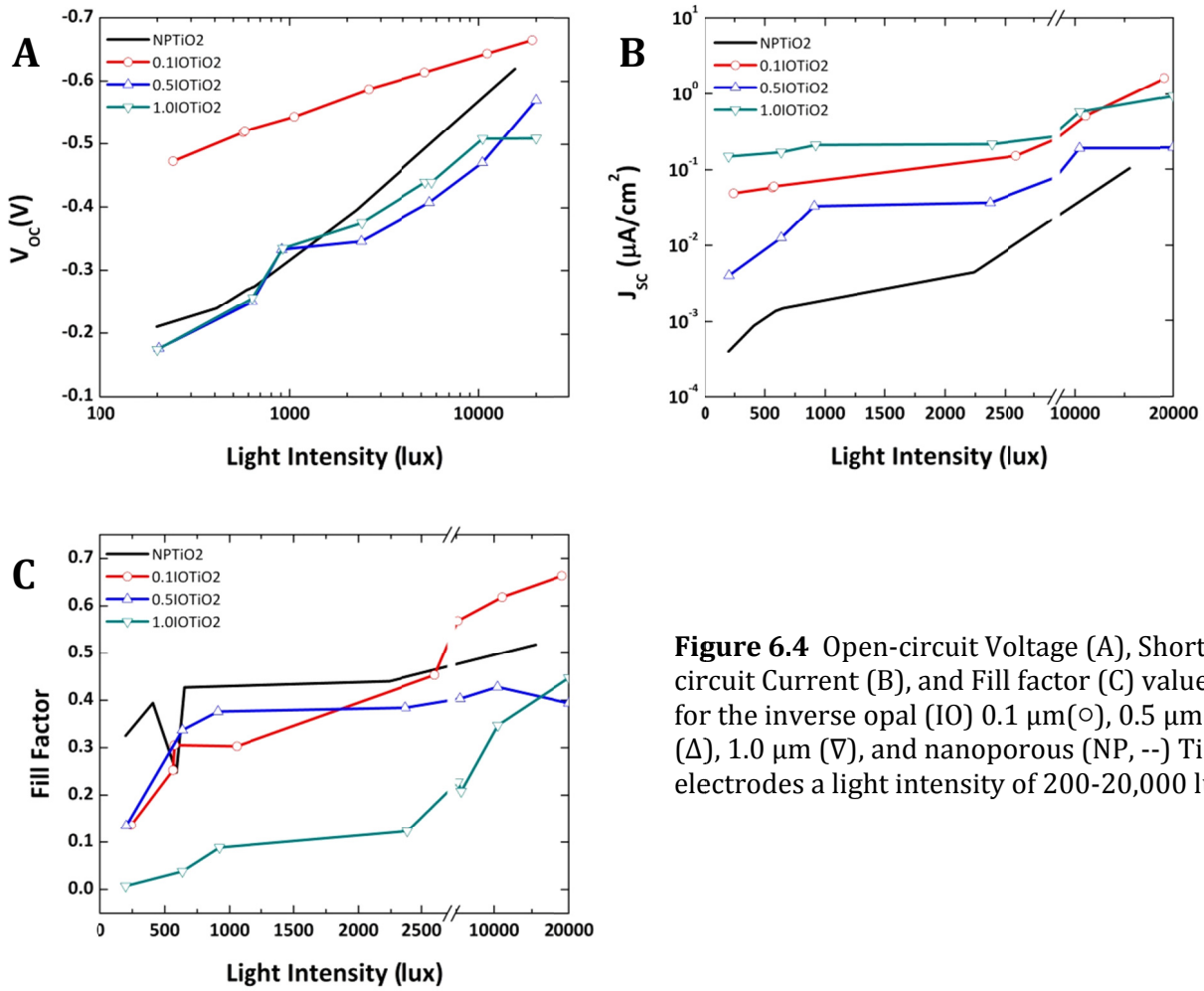

Figure 6.4 Open-circuit Voltage (A), Short-circuit Current (B), and Fill factor (C) values for the inverse opal (IO) 0.1 μm(○), 0.5 μm (Δ), 1.0 μm (∇), and nanoporous (NP, --) TiO_2 electrodes a light intensity of 200-20,000 lux.

$$V_{OC} = \frac{k_B T}{e} \ln\left(\frac{n}{n_0}\right) \qquad \textit{Eq. 6.1}$$

where k_BT is the thermal energy, e is the elementary charge, and n_0 is the electron concentration in the dark. From Eq. 6.1, it is obvious that the recombination rate also has a major impact on the V_{OC} obtained at any light intensity. The semilog plot of Figure 6.4A displays a general monotonic correlation between V_{OC} and light intensity. The 0.1 μm electrode has the highest V_{OC} at any light intensity among all the electrodes. The slope of the curves in this graph, $dV_{OC}/dn = 1/n$, is inversely proportional to the free electron density. Hence, the 0.1 μm electrode has the highest free electron density compared to the larger inverse opals and the nanoporous electrode.

The short-circuit current ($J_{sc} = I_{SC}/cm^2$) shown in Figure 6.4B is proportional to the internal surface area, and is defined as the difference between photogenerated current (J_{PH}) and recombination current (J_R). Figure 6.4B shows that the short-circuit current normalized by the internal surface area increases exponentially with light intensity. The 0.1 μm and 1.0 μm IO electrodes have the highest current density, despite having a comparatively low internal surface area. The NP electrode, which has the largest surface area, has the lowest current density. The rate of increase of J_{SC} is much faster in the low-intensity region compared to the high-intensity region. Even when J_{SC} is normalized by geometric surface area, the inverse opal electrodes have a higher short circuit current density at low-light intensity compared to the nanostructured electrode despite the large difference in their internal surface area (Table 6.1).

Figure 6.4C shows the effect of light intensity on the fill factor of the DSSC. Fill factor (*FF*) is an indication of the quality of the cell, and is defined as the ratio between the maximum power output of the cell and the theoretical maximum ($J_{SC}*V_{OC}$). The inverse opal electrodes show that the *FF* increases exponentially with respect to the light intensity in both the high and low-intensity regions. In the low- intensity region, the inverse opal electrodes have the same rate of increase and

this rate is faster than in the high-intensity region. The nanostructured sample shows virtually the same trend over the entire range of tested light intensities.

Figure 6.5A compares the open circuit voltage decay rates (dV_{OC}/dt) of the IO and NP TiO_2 electrodes at a low-light intensity of 600 lux. The peaks depicted are inversely proportional to the electron lifetime within each electrode as shown in equation 6.2:

$$\tau = -\frac{k_B T}{e}\left(\frac{dV_{OC}}{dt}\right)^{-1} \qquad \textit{Eq. 6.2}$$

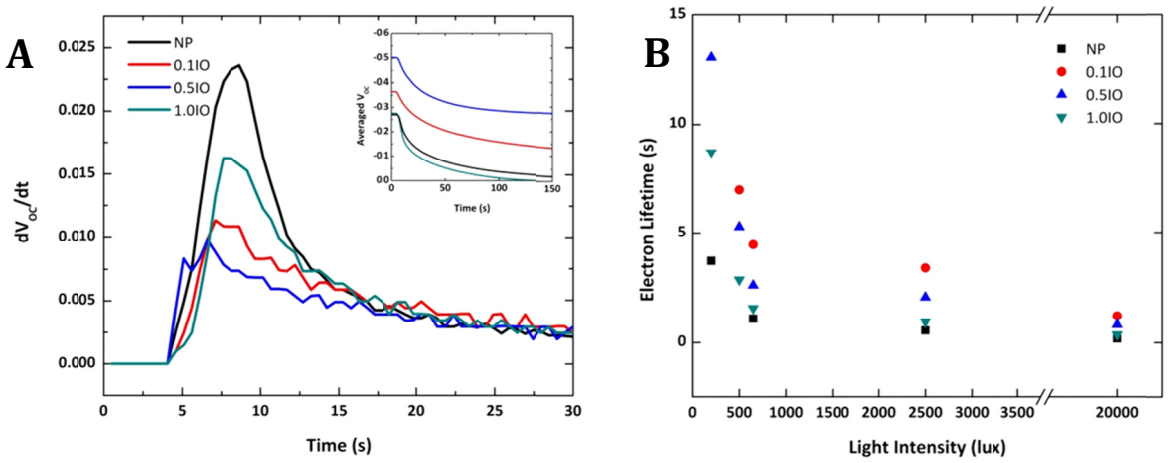

Figure 6.5 Open-circuit Voltage Decay (OCVD): time derivative of V_{OC} is inversely proportional to the electron recombination lifetime within each electrode. (A) dV_{OC}/dt comparison between NP and IO TiO_2 electrodes at ~600 lux. (Inset) Raw OCVD data. (B) Comparison of electron lifetimes of NP and IO TiO_2 electrodes at three different light intensities.

The nanoporous electrode has the highest peak, indicating that electrons within this electrode quickly recombine with the electrolyte. Among the inverse opals, the 1.0μm electrode has the highest peak (i.e., shortest electron lifetime), while the 0.5 μm electrode has the lowest peak (i.e., longest electron lifetime). Figure 6.5B plots the electron lifetime against the light intensity incident upon the cell under evaluation. The electron lifetime decreases as the light intensity increases for all of the electrodes tested.

Figure 6.6 shows the Nyquist and Bode plots for a NP and 0.1 μm TiO_2 electrodes in the 600 lux (Δ), ~2500 lux (○), ~20000 lux (□). The impedance due to electron transfer from the conduction band of the mesoscopic film to the triiodide ions in the electrolyte, presented by the semicircle in the intermediate frequency regime of the Nyquist plot (Fig. 6.6A and C), increases as the light intensity decreases. The frequency of the peak phase angle shown in the Bode plots (Fig. 6.6B and

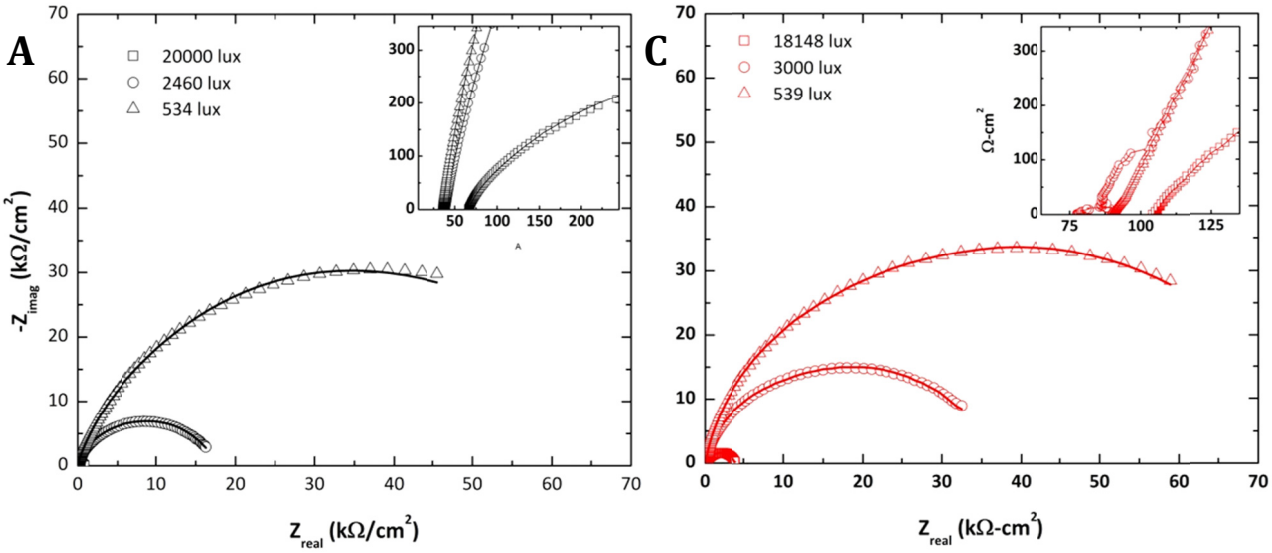

Figure 6.6 EIS Nyquist and Bode plots at ~20000, ~2500, ~600 lux. (A,B) NP electrode. Peak phase angle occurs at 100 Hz (20,000 lux), 32 Hz (2460 lux), and 30 Hz (534 lux). (C,D) 0.1 μm IO electrode. Peak phase angle occurs at 22 Hz (18148 lux), 13 Hz (3000 lux), and 10.5 Hz (539 lux).

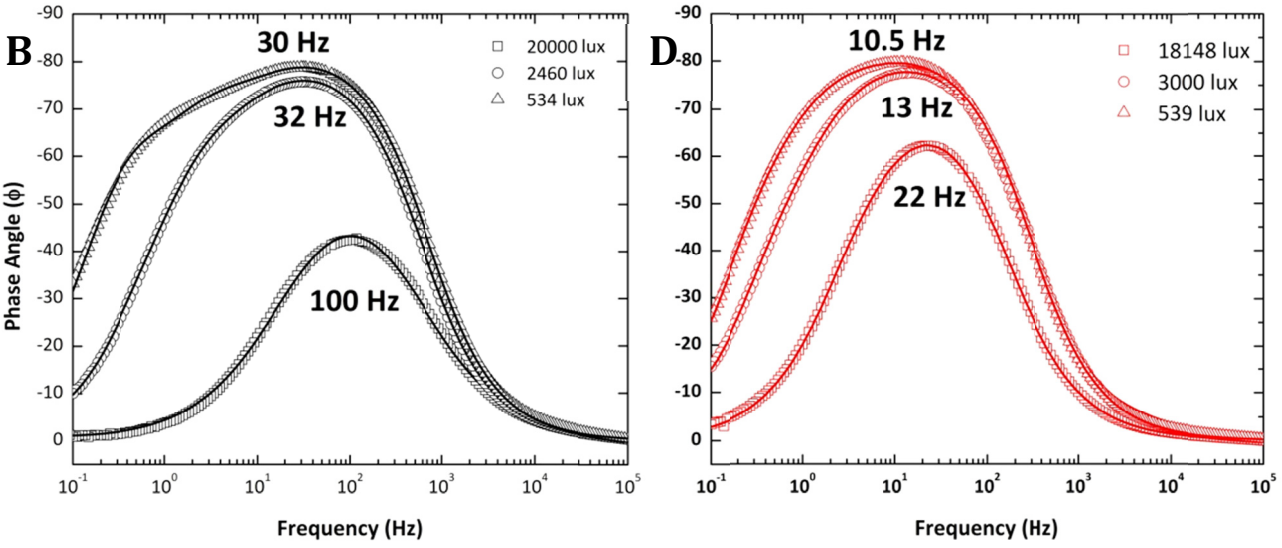

D) is representative of the electron lifetime within the electrode, and appears at a higher frequency in the NP electrode compared to the 0.1 μm electrode for the same light intensity. The spectra are fitted using the equivalent circuit shown in Fig. 6.7, where the R_{pc}—Q_{oc} and R_{pw}—Q_{ow} couples represent the counter electrode and working electrode, respectively; R_u represents the resistances due to contacts; and Z_D represents the resistance due to diffusion of I_3^- between the two electrodes. Fitting data for plots shown in Fig. 6.6 can be found in the Appendix B.

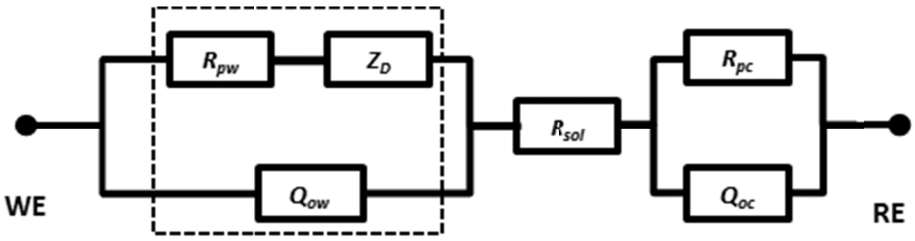

Figure 6.7 Equivalent Circuit of the two-electrode photoelectrochemical cells under review: R_{pc}--Q_{oc} = counter electrode/electrolyte interface, R_{pw}--Q_{ow} = working electrode (IO and NP TiO_2)/electrolyte interface. Z_D=Nernst diffusion of I_3^-, R_u=contact resistances within cell.

6.4 Discussion

Inverse opal TiO_2 electrodes of three different pore sizes are fabricated and evaluated in a two-electrode setup via cyclic voltammetry, open circuit voltage decay, and electrochemical impedance spectroscopy measurements. The results of these experiments show that the inverse opal electrodes perform better at low-light intensities compared to the standard nanostructured electrodes in current DSSCs, as evidenced by the higher J_{SC}, higher charge-transfer resistances (R_{pw}), and longer electron lifetimes (τ).

The photocurrent-voltage curves obtained by cyclic voltammetry tests show that the interconnected network of the inverse opal has a positive impact on the overall efficiency of the DSSC. The efficiency of the prepared solar devices are computed by Equation 6.3,

$$\eta = \frac{V_{OC} * I_{SC} * FF}{P_{in}} \qquad \textit{Eq. 6.3}$$

where P_{in} is the intensity of the light incident upon the cell. Figure 6.8 shows the efficiency ($\mu W/cm^2$) of each assembled DSSC under different light intensities in the range from 200 to 20,000 lux. The 0.1 μm electrode (red bar) is clearly the best DSSC for indoor settings (≤ 2500 lux). Since the different electrodes have a similar *FF* (Fig. 6.4C) in this intensity region, the main reason for the superior performance of the 0.1 μm electrode is the higher V_{OC}. Equation 6.1 shows that V_{OC} depends on $ln(n/n_0)$. n is usually scaled by the excitable surface area of the electrode, and n_0 is determined by crystallographic deficiencies such as internal traps and surface traps. Based on the calculated internal surface area (Table 6.1), the NP electrode would have the highest n, and 0.5 and 1.0 μm would have the lowest n. From Chapter 5, we know that the trap density, and consequently the dark current, scales according to the surface area per unit volume of the electrode. Accordingly, the NP electrode has the highest dark current and the 1.0 μm IO electrode has the lowest dark current. Normalization of n, by the n_0 value for the 1.0 μm IO electrode (Table 6.2) shows that the 0.1 μm IO electrode has the largest absolute value of $ln(n/n_0)$, followed by the 0.5 μm electrode. The NP electrode has similar n/n_0 values to the 1.0 μm electrode. This trend matches the V_{OC} data in

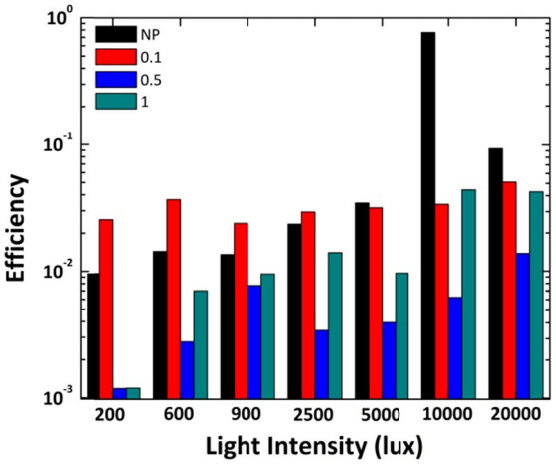

Figure 6.8 Device efficiency at different lux values for inverse opal DSSCs of varying pore sizes

Figure 6.4A, where the NP electrode is similar to the 0.5 and 1.0 μm IO electrodes, while the 0.1 μm IO electrode has the highest V_{OC}.

Table 6.2 Relative trends of V_{OC} of the NP and IO TiO_2 electrodes.

SAMPLE	V_{OC}	n	n_0	(n/n_0)	$\ln(n/n_0)$
NP	-0.21	40	0.78 (*55)	0.93	-0.07
IO0.1	-0.48	2	53	0.04	-3.28
IO0.5	-0.17	1	2	0.5	-0.69
IO1.0	-0.18	1	1	1	0

The high V_{OC} values for the 0.1 μm IO electrode translate into a low recombination current, i.e., the number of surface trap sites is low. Comparison of the J_{SC} values (Fig. 6.4B) of the 0.1 μm IO and NP electrodes, which have comparable pore sizes, shows that the inverse opal electrode supports more photocurrent. Since J_{SC} is the balance between the photogenerated current and the recombination current, a lower J_{SC} value for the NP electrode with the higher surface area, is due to a high recombination current as a result of the high density of surface trap sites.

Both the OCVD tests and the EIS Bode plots confirm that the inverse opal 0.1 μm electrode has a longer electron lifetime compared to the NP electrode. Once again, this feature is attributed to the lower density of surface trap sites in the inverse opal electrode. A comparison of the Nyquist plots for both electrodes reinforces the superiority of the 0.1 μm IO electrode: the charge-transfer resistance represented by the semi-circle in the mid-frequency region is higher in the inverse opal 0.1 μm electrode. In other words, the lower density of surface traps decreases the probability of electron recombination.

Table 6.3 Comparison of Electron Lifetimes in 0.1IO and NP TiO_2 electrode.

Light Intensity (lux)	OCVD (ms)		EIS (ms)	
	0.1	**NP**	**0.1**	**NP**
600	4519	1101	598	209
2500	3447	561	483	196
20000	1023	187	285	62

Table 6.3 provides a comparison of the electron lifetimes within the NP and 0.1 μm electrodes as computed by OCVD tests and EIS. At low light intensities, most of the photogenerated electrons are trapped in surface sites whose energies lie deep in the bandgap. The Fermi level lies mid-bandgap thereby lowering V_{OC} ($E_{Fn} - E_{REDOX}$) and consequently the efficiency. As the light intensity increases, more surface sites are occupied, raising the Fermi level, the associated V_{OC} and finally the efficiency. On the other hand, the increase in the decay rate of the V_{OC} as the incident intensity increases is attributed to the increase in the Fermi level.

There is also a noticeable difference in relative electrode performance in either illuminance range. Below 2500 lux, the 0.1 μm sample has the higher J_{SC} despite having a smaller surface area than the NP sample. Above 2500 lux, the higher surface area of the NP sample wins out as evidenced by higher J_{SC} and V_{OC} values. Once again, the trend in the reaction frequency mentioned in Chapter 5 offers an answer. The NP sample has a reaction frequency that is an order of magnitude higher compared to the inverse opals, which translates to a higher likelihood of electron recombination. Combined with the fact that the NP sample has a higher trap density, the diminished performance is a result of an insufficient number of photogenerated electrons (due to low-light intensity) to occupy the surface traps and thus negate/lessen their effect on J_{SC}. Once the surface traps have been filled, the electrode surface area is the dominant contributor to J_{SC}. The latter is the main reason, why increasing the internal surface area of the TiO_2 electrode is a

commonly adopted way to increase the efficiency of a DSSC. Meanwhile, the results presented here indicate that such an approach would be detrimental to the device efficiency at low-light intensities.

Among the inverse opals, the 1.0 μm electrode has a consistently higher J_{SC} than the 0.5 μm electrode. Since both electrodes have the same surface area, and the same incident light intensity, the reason for the better performance of the 1.0 μm IO electrode rests with any differences in the microstructure, i.e., pore size dependent optical bandgap. It is possible that the optical bandgap of the 0.5 μm electrode lies within the absorption range of the dye, which would result in diminishing the efficiency delivered. At low light intensities, the 0.1 μm IO electrode outperforms the larger inverse opal electrodes. However as the light intensity increases, the 0.1 and 1.0 μm IO electrodes exhibit similar performances. The increase in efficiency comes from the rise in the *FF*. The 1.0 μm electrode has a low *FF* due to the lack of a blocking layer, i.e., a thin TiO_2 layer applied to the FTO electrode prior to IO formation. The available interface between the FTO substrate and the electrolyte is largest in the 1.0 μm IO electrode due to the larger internal pore size, which presents an unwanted recombination pathway for the photogenerated electrons leading to a decrease in the *FF* (Fig. 6.4C). At high lux values, the 1.0 μm IO electrode has the lowest recombination current due to the lowest number of surface traps.

6.5 Chapter Summary

The photoelectrochemical characterization of inverse opal electrodes ranging from 0.1 via 0.5 to 1.0 μm in pore size shows that the interconnected, ordered, porous microstructure is effective at limiting electron recombination, when such electrodes are incorporated in DSSCs. Compared to the standard nanostructured electrode, inverse opal electrodes have a smaller trap density and better inter-particle connections. At low-light intensities common to indoor environments (200 – 700 lux), the inverse opals have a higher (~3×) efficiency. As the light intensity increases to outdoor

conditions, electrode surface area is the limiting factor for efficiency and the NP electrode outperforms the IO electrodes.

Another feature of the inverse opal electrodes, though not explicitly discussed in this chapter, is the close contact between the electrode and the electrolyte. In the instance of replacing the electrolyte with a more viscous option, diffusion impedance is expected to increase. The larger pores of the inverse opal electrodes would enable better infiltration of the electrolyte and easier diffusion of the redox ions during operation. Post-illumination, the oxidized dye molecule obtains an electron from the redox couple in the electrolyte and the resulting anion must then be regenerated at the counter electrode. However, the increased viscosity would slow down this process making the recombination of photogenerated electrons with the anion more likely. Under such conditions, an electrode with lower surface trap density would be beneficial. With the addition of a blocking layer, it is the prediction of this Thesis that the performance enhancement would be even higher in inverse opal DSSCs with viscous electrolytes.

7 Conclusions and Future Work

7.1 Concluding Remarks

The objective of this Thesis has been to study the effect of TiO_2 network geometry on electron transport within the DSSC. In this regard, we chose inverse opals because their porous, ordered, and interconnected network is easily controlled by the size of the templating particle. By assaying several common methods of inverse opal fabrication, we have demonstrated that the combination of particle size and method is an important factor to yield inverse opals of high and comparable quality. Surface traps, known to be Ti^{3+} sites, significantly limit electron movement within this solar device. Since the surface area-to-volume ratio of inverse opals can be controlled, we have been able to study the effect of surface traps on electron movement within the TiO_2 structure. Finally, the inverse opal TiO_2 structured electrodes were incorporated into a standard DSSC configuration and have been shown to perform better than the nanostructured electrode in less intense indoor lighting environments.

The most efficient DSSC cell configuration currently operates at 12% efficiency (AM 1.5), consists of a Titanium dioxide (TiO_2 or titania) photoanode, a ruthenium polypyridyl dye, and an transparent conducting FTO counter electrode, and uses the I^-/I_3^- redox couple dissolved in acetonitrile as an electrolyte. We chose the same cell components as a control for this Thesis work. The most widely tested TiO_2 photoanode has a random, nanoporous network of titania nanoparticles (TiO_2-NP) with an average pore size of ≤10 nm and a porosity of 55%. This TiO_2-NP photoanode shuttles photo-excited electrons from the dye molecules to the external circuit. Electron transport has been shown to be a limiting factor in the performance of these NP

electrodes. The structural disorder at the contact between two TiO_2 nanoparticles leads to enhanced scattering of free electrons, thus reducing electron mobility. Instead, an ordered and strongly interconnected microstructure promotes electron transport, thus leading to higher efficiencies.

The ruthenium complex dye, which is adsorbed onto the TiO_2 photoanode, absorbs photons from the provided external irradiation and starts the electron movement within the cell. The photogenerated electrons diffuse through the nanoporous TiO_2 network and make their way to the external circuit. The circuit is completed by the transparent and conducting FTO counter electrode and the acetonitrile electrolyte. The electrons from the external circuit collect at the FTO counter electrode and reduce the I^-/I_3^- redox couple. The notoriously slow kinetics of the heterogeneous electron transfer of the I^-/I_3^- redox pair is partly responsible for the high efficiency (12%) reported, because it enhances charge separation by separating the timescales of electron recombination and dye regeneration. However, the acetonitrile-based organic electrolyte has proven to be a roadblock when it comes to commercialization of DSSCs. For example, iodide has a tendency to degrade silver contacts, which serve as current collectors, and acetonitrile is too volatile and toxic leading to sealing and environmental problems. To circumvent these issues, current research has focused on replacing the electrolyte with more viscous and environmentally benign analogs. In light of this trend, the mesoporous nature of the TiO_2 NP electrode is problematic since it hinders the diffusion of ions. In addition to slower ionic diffusion, incomplete wetting of the viscous electrolytes to the TiO_2 NP electrode is a cause for diminished performance. Replacing the mesoporous electrode with an inverse opal electrode provides the key to improving both ionic diffusion and electrolyte wettability, since inverse opals have large, ordered, and interconnected pores.

In addition, a DSSC with a mesoporous electrode has a large number of surface traps. These surface traps can aid or hinder electron transport depending on the surrounding electrolyte.

Electrolyte alternatives tend to have a larger size and quicker kinetics, which combined with the large number of traps, have been shown to delivered lower efficiencies. In the case of inverse opal electrodes, we control the number of surface traps since their surface area is controlled by the size of the templating particles used during synthesis. The market niche for immediate DSSC commercialization has been identified as indoor applications. A mesoporous electrode with many traps that would remain empty at low illumination such as the TiO_2 NP electrode would be adversely affected when used indoors.

Based on this analysis, we determined that the investigation of TiO_2 photoanodes with inverse opal structure of varying pore sizes is warranted with the following three goals:

- identify synthetic methods that enable us to prepare inverse opal photoanodes with controlled pores size and comparable quality (Chapter 4),
- characterize the electron transport mechanism and recombination in these photoanodes in comparison with the NP control photoanode (Chapter 5), and
- evaluate the performance of the inverse opal TiO_2 photoanodes in actual DSSC configuration compared to that with a NP-TiO_2 photoanode (Chapter 6).

Optical and scanning electron microscopy in combination with fast Fourier Transform were used to determine the structure of the inverse electrodes, while cyclic voltammetry (CV), electrochemical impedance spectroscopy (EIS), and chronoamperometry (CA) gave insight into the electrochemical characteristics of the TiO_2 electrodes such as surface trap density, trap filling, and recombination kinetics, as a function of their pore size. Last but not least, photocurrent-voltage curves (PV), open circuit voltage decay (OCVD), and CV at slow scan rates were used to characterize the performance of inverse opal electrode based DSSCs.

Colloidal self-assembly is the method that has been adopted for preparing inverse opals with pore sizes ranging from 0.1 to 10 μm used in this Thesis. Firstly, monodisperse polystyrene particles are assembled into close-packed opal structures and then infiltrated with a TiO_2 precursor. The infiltrated opal structures are calcined to eliminate the template spheres, resulting in inverse opal structures. Changing the size of the template particles controlled the inverse opal pore size and consequently the surface area per unit volume. By assaying several common fabrication methods, we demonstrated that particle size is an important parameter to yield inverse opals of high quality. The quality of the prepared inverse opals was determined via Fast Fourier Analysis of the SEM images obtained for each sample. Among the methods studied, liquid phase deposition (LPD) has been identified as the best for particles sizes ≤ 1.0 μm. If the particle-to-precursor ratio and ambient temperature during assembly are optimized, co-assembly (CoA) has been shown to be better than LPD in making inverse opals. For particles sizes >1.0 μm, gravity becomes a factor and an extra impetus is required to keep the particles afloat. Electrophoretic deposition (EPD) has been identified as the best method for assembling particles ranging from above 1.0 μm to below 5.0 μm.

TiO_2 inverse opal structures with pore sizes 0.1, 0.5, and 1.0 μm have been evaluated electrochemically by cyclic voltammetry, chronoamperometry, electrochemical impedance spectroscopy, and open-circuit voltage decay. The electrodes were compared against the standard configuration of a randomly-connected network of nanoparticles. Chronoamperometry measurements revealed that trap density depends both on the applied potential and on the surface area per unit volume of the TiO_2 electrode. Electrochemical impedance measurements showed that the inverse opal electrodes have a higher conductivity, one that is a function of the trap density, and were less likely to lose electrons to recombination. By virtue of their higher transport frequency and slower reaction frequency, the inverse opal structure has been identified to be a better electrode structure than the one comprised of a random network of nanoparticles. These

advantages persisted even when the inverse opals were incorporated into the DSSC configuration. As a result, inverse opal DSSCs showed a 3-fold increase in efficiency in low light indoor settings. However, as the light intensity was increased to outdoor conditions, electrode surface area became the limiting factor for efficiency and the NP TiO_2 photoanode outperformed the IO TiO_2 photoanode.

7.2 Future Work

As mentioned above, both electron transport efficiency and accessibility of the internal surface of the photoanode play a crucial role in current efficiency limitation of DSSCs. A feature of the inverse opal electrodes that needs to be explored in future studies is the close contact between the electrode and the electrolyte. Replacement of the electrolyte with a more viscous option such as an ionic liquid is likely to lead to a diffusion impedance increase. The larger pores of the inverse opal electrodes will enable better infiltration of the electrolyte and easier diffusion of the redox ions during operation. Post-illumination, the oxidized dye molecule obtains an electron from the redox couple in the electrolyte and the resulting anion must then be regenerated at the counter electrode. However, the increased viscosity would slow down this process making the recombination of photogenerated electrons with the anion more likely. Under such conditions, an electrode with lower surface trap density would be beneficial. With the addition of a blocking layer, it is the prediction of this Thesis that the performance enhancement would be even higher in inverse opal DSSCs with viscous electrolytes.

Further, inverse opal electrodes provide a third advantage through the photonic nature of their periodic structure. Future investigations should expand towards characterization of these inverse opal photoanodes with respect to photonic properties and their effect on total photon absorption and surface-enhancement due to the interaction of the dye molecules with the nanostructured surface of the inverse opal backbone using techniques such as surface-enhanced Raman spectroscopy.

The work presented in this Thesis has reinforced that an un-interrupted network of TiO_2 nanoparticles coupled with lower surface trap density is key to reducing the recombination and increasing the photogenerated current, especially in low-light situations. It has also been shown in the literature that nanorods are better able to conduct electrons. Thus a network of nanorods that are joined via highly conducting endcaps might perform better than the nanoparticle network. This approach would open electrode preparation up to field-directed assembly, which is likely less time consuming than inverse opal preparation. Such a dense 3D network would have a large surface area, good contact with the electrolyte, and enable efficient electron transport through the nanorod backbone.

Last but not least, the colloidal assembly techniques discussed and employed in this Thesis lend themselves to the use of precursors other than titanium isopropoxide. For example, a precursor such as zinc hydroxide can be used to make ZnO inverse opal electrodes, which may show improved photon absorption and better coupling between dye and semiconductor phonon modes leading to more efficient photon and electron collection.

Appendix A: EIS Fit Values for Bare TiO_2 Electrodes

Table A.1 shows the fitting parameters obtained when fitting the EIS data such as shown in Figure 5.5 using the equivalent circuits shown in Figure 5.2. Note that Figure 5.5 shows only an exemplary plot at a DC potential of -0.5 V. Parameters listed in Table A.1 are for measurements at DC potentials of V_{DC} = 0.5, 0.0, -0.1, -0.3, and -0.5V.

Table A.1 Values for components of equivalent circuits used to model the blank, the inverse opal, and the nanoporous electrodes.

	FTO-Electrolyte Interface			TiO_2-Electrolyte Interface				Ionic Diffusion in FTO-TiO_2 electrode	
	Q_o2 ($S*s^{a2}$)	a2	R_p2 (Ω)	R1 (Ω)	R_p1 (Ω)	$Q_o1\times10^{-5}$ ($S*s^{a1}$)	a1	$W\times10^{-5}$ ($S*s^{1/2}$)	B ($s^{1/2}$)
					Blank				
0.5	$3.68\times10^{-5}\pm1.41\times10^{-6}$	0.969 ±0.021	---						
0.0			140 ±0.1						
-0.1			156 ±38						
-0.3			131 ±13						
-0.5			140 ±15						
					NPTiO₂				
0.5	$3.12\times10^{-9}\pm6.29\times10^{-10}$	0.988 ±0.025	540 ±254	38 ±27	65590 ±8448	2.17 ±0.03	0.947 ±0.002	2.38 ±0.35	0.115 ±0.020
0.0			200 ±96	44 ±14	27927 ±2913	3.49 ±0.56	0.861 ±0.031	46.48 ±29.98	0.052 ±0.028
-0.1			181 ±13	31 ±11	15978 ±1077	6.41 ±0.34	0.816 ±0.009	47.08 ±13.22	0.056 ±0.017
-0.3			59 ±3	31 ±16	1476 ±229	5.39 ±1.99	0.841 ±0.026	556.63 ±60.35	0.869 ±0.006
-0.5			55 ±13	37 ±13	178 ±10	2.82 ±0.29	0.909 ±0.020	1257.33 ±57.57	0.982 ±0.032

Appendix A continued..

	FTO-Electrolyte Interface			TiO₂-Electrolyte Interface				Ionic Diffusion in FTO-TiO₂ electrode	
	Q_o2 ($S*s^{a2}$)	a2	R_p2 (Ω)	R1 (Ω)	R_p1 (Ω)	$Q_o1\times10^{-5}$ ($S*s^{a1}$)	a1	$W\times10^{-5}$ ($S*s^{1/2}$)	B ($s^{1/2}$)
				0.1 IOTiO₂					
0.5	$3.28\times10^{-9}\pm2.06\times10^{-9}$	0.997 ±0.003	2254 ±257	37 ±6	433300 ±13796	0.94 ±0.02	0.947 ±0.004	2.29 ±0.25	0.115 ±0.020
0.0			553 ±13	29 ±13	484700 ±151147	3.48 ±0.40	0.859 ±0.013	24.00 ±4.72	0.052 ±0.028
-0.1			462 ±37	22 ±9	510400 ±75560	4.26 ±0.07	0.841 ±0.0	47.28 ±13.22	0.056 ±0.017
-0.3			202 ±17	32 ±11	58817 ±1544	7.65 ±0.46	0.750 ±0.0	249.43 ±56.46	0.869 ±0.006
-0.5			71 ±1	26 ±0	2413 ±55	9.69 ±0.26	0.780 ±0.0	1741.00 ±1018.00	0.982 ±0.032
				0.5 IOTiO₂					
0.5	$1.27\times10^{-7}\pm8.96\times10^{-8}$	0.995± 0.013	1358 ±177	6± 0.45	1342667 ±114527	1.00 ±0.03	0.959 ±0.001	2.45 ±1.01	0.098 ±0.023
0.0	$1.16\times10^{-8}\pm1.10\times10^{-9}$		852 ±9	5 ±0.05	669400 ±15839	2.21 ±0.02	0.899 ±0.001	16.36 ±1.04	0.067 ±0.004
-0.1			717 ±6	4 ±0.07	434533 ±5781	3.02 ±0.05	0.859 ±0.0	31.52 ±1.80	0.065 ±0.004
-0.3			265 ±1	4 ±0.17	46433 ±1303	2.22 ±0.03	0.875 ±0.008	228.23 ±44.63	0.062 ±0.012
-0.5			162 ±19	4 ±0.87	3056 ±304	2.35 ±0.76	0.889 ±0.032	441.97 ±239.04	0.339 ±0.164
				1.0 IOTiO₂					
0.5	$7.00\times10^{-6}\pm5.89\times10^{-7}$	0.999 ±1.79 ×10⁻⁴	1184 ±297	3 ±0.94	418467 ±20500	1.38 ±0.12	0.921 ±0.002	31.24 ±14.30	0.008 ±0.006
0.0			737 ±138	2 ±0.0	247900 ±38204	2.98 ±0.14	0.812 ±0.010	110.56 ±4.52	0.009 ±0.001
-0.1			484 ±64	2 ±0.31	492867 ±231157	3.87 ±0.02	0.773 ±0.024	191.23 ±38.97	0.016 ±0.003
-0.3	$2.66\times10^{-7}\pm1.89\times10^{-7}$		184 ±2	2 ±0.0	24845 ±672	5.77 ±0.07	0.800 ±0.0	680.65 ±292.24	0.044 ±0.019
-0.5			111 ±16	2 ±0.0	2014 ±1140	7.16 ±0.38	0.800 ±0.0	3022.50 ±553.66	0.055 ±0.015

Appendix B: EIS Fit Values for IO-DSSCs

Table B.1 shows the fitting parameters obtained when fitting the EIS data such as shown in Figure 6.6 using the equivalent circuits shown in Figure 6.7. Parameters listed below are for measurements of 0.1IO and NP TiO_2 electrodes at light intensities of 20000, 3000, and 500 lux.

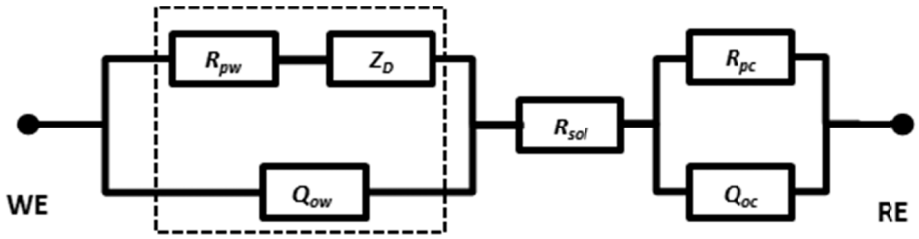

Table B.1 Values for components of equivalent circuits used to model the 0.1 μm inverse opal and the nanoporous electrodes.

		0.1 IOTiO2			NP TiO2		
		20000	**3000**	**500**	**20000**	**3000**	**500**
R_{pw}	ohm*cm²	1.53E+03	2.63E+04	403.7	195.7	1.37E+04	1.99E+04
Q_{ow}	S*s^a/cm²	2.41E-05	1.04E-05	9.85E-06	5.70E-05	1.54E-05	1.17E-05
a_w		0.938	0.934	0.928	0.788	0.930	0.937
R_{sol}	ohm*cm²	104.3	78.89	89.35	65.09	38.73	35.65
R_{pc}	ohm*cm²	1.70E+03	4.454	0.672	523.4	515.1	205.9
Q_{oc}	S*s^a/cm²	7.05E-05	8.17E-06	1.70E-05	3.69E-05	6.31E-05	7.60E-05
a_c		0.856	0.991	0.929	0.859	0.927	1.000
W	S*s$^{1/2}$/cm²	3.82E-04	9.57E-05	7.09E-07	0.006	3.16E-04	2.11E-05
B	s$^{1/2}$	0.227	0.856	0.052	0.038	0.803	1.01
Z_D	ohm*cm²	5.94E+02	8.94E+03	7.36E+04	6.48	2.55E+03	4.78E+04
Goodness of Fit		1.74E-05	2.67E-04	3.13E-04	1.07E-04	4.47E-05	8.97E-05
X^2		0.42%	1.63%	1.77%	1.03%	0.67%	0.95%

Bibliography

(1) (EIA), U. S. E. I. A., Ed. 2011.

(2) *World Energy Outlook*, International Energy Agency, 2012.

(3) Tester, J. W.; Drake, E. M.; Driscoll, M. J.; Golay, M. W.; Peters, W. A. *Sustainable Energy: Choosing among Options*; 2 ed.; MIT Press, 2012.

(4) Becquerel, E. *Comptes Rendus* **1839**, *9*, 561.

(5) Plummer, J. D.; Deal, M. D.; Griffin, P. B. *Silicon VLSI Technology*; Prentice Hall, 2000.

(6) *Global Trends in Renewable Energy Investment*, Bloomberg New Energy Finance, UNEP SEFI, Frankfurt School, 2011.

(7) Ardani, K.; Margolis, R. *2010 Solar Technologies Market Report*, U.S. Department of Energy, 2011.

(8) Tao, M. *The Electrochemical Society's Interface* **2008**, *17*.

(9) Ohl, R. 1946; Vol. 2,402,662.

(10) Chapin, D.; Fuller, C.; Pearson, G. *Journal of Applied Physics* **1954**, *25*.

(11) NREL Rev. 2012; Vol. 2012.

(12) Kay, A.; Grätzel, M. *The Journal of Physical Chemistry* **1993**, *97*, 6272.

(13) Jean-Claude, T.; Renata, S.; Artur, B.; Thomas, G. *Semiconductor Science and Technology* **2011**, *26*, 045007.

(14) Zervos, H. *Dye Sensitized Solar Cells (DSSC/DSC) 2012-2023: Technologies, Markets, Players*, IDTechEx.com, 2012.

(15) Grätzel, M. *Progress in Photovoltaics: Research and Applications* **2000**, *8*, 171.

(16) Grätzel, M. *Pure and Applied Chemistry* **2001**, *73*, 459.

(17) J. Frank, A.; Kopidakis, N.; Lagemaat, J. v. d. *Coordination Chemistry Reviews* **2004**, *248*, 1165.

(18) Grätzel, M. *Journal of Photochemistry and Photobiology A: Chemistry* **2004**, *164*, 3.

(19) Burnside, S. D.; Shklover, V.; Barbé, C.; Comte, P.; Arendse, F.; Brooks, K.; Grätzel, M. *Chemistry of Materials* **1998**, *10*, 2419.

(20) Polo, A. S.; Itokazu, M. K.; Murakami Iha, N. Y. *Coordination Chemistry Reviews* **2004**, *248*, 1343.

(21) Mishra, A.; Fischer, M. K. R.; Bäuerle, P. *Angewandte Chemie International Edition* **2009**, *48*, 2474.

(22) Smestad, G. P.; Gratzel, M. *Journal of Chemical Education* **1998**, *75*, 752.

(23) Bignozzi, C. A.; Argazzi, R.; Kleverlaan, C. J. *Chemical Society Reviews* **2000**, *29*, 87.

(24) Nazeeruddin, M. K.; De Angelis, F.; Fantacci, S.; Selloni, A.; Viscardi, G.; Liska, P.; Ito, S.; Takeru, B.; Grätzel, M. *Journal of the American Chemical Society* **2005**, *127*, 16835.

(25) Argazzi, R.; Larramona, G.; Contado, C.; Bignozzi, C. A. *Journal of Photochemistry and Photobiology A: Chemistry* **2004**, *164*, 15.

(26) Islam, A.; Sugihara, H.; Hara, K.; Singh, L. P.; Katoh, R.; Yanagida, M.; Takahashi, Y.; Murata, S.; Arakawa, H.; Fujihashi, G. *Inorganic Chemistry* **2001**, *40*, 5371.

(27) Hasselmann, G. M.; Meyer, G. J. *The Journal of Physical Chemistry B* **1999**, *103*, 7671.

(28) Bessho, T.; Constable, E. C.; Graetzel, M.; Hernandez Redondo, A.; Housecroft, C. E.; Kylberg, W.; Nazeeruddin, M. K.; Neuburger, M.; Schaffner, S. *Chemical Communications* **2008**, 3717.

(29) Ferrere, S. *Chemistry of Materials* **2000**, *12*, 1083.

(30) Forneli, A.; Planells, M.; Sarmentero, M. A.; Martinez-Ferrero, E.; O'Regan, B. C.; Ballester, P.; Palomares, E. *Journal of Materials Chemistry* **2008**, *18*, 1652.

(31) Cid, J.-J.; Yum, J.-H.; Jang, S.-R.; Nazeeruddin, M. K.; Martínez-Ferrero, E.; Palomares, E.; Ko, J.; Grätzel, M.; Torres, T. *Angewandte Chemie International Edition* **2007**, *46*, 8358.

(32) Edvinsson, T.; Li, C.; Pschirer, N.; Schöneboom, J.; Eickemeyer, F.; Sens, R.; Boschloo, G.; Herrmann, A.; Müllen, K.; Hagfeldt, A. *The Journal of Physical Chemistry C* **2007**, *111*, 15137.

(33) Yum, J.-H.; Walter, P.; Huber, S.; Rentsch, D.; Geiger, T.; Nüesch, F.; De Angelis, F.; Grätzel, M.; Nazeeruddin, M. K. *Journal of the American Chemical Society* **2007**, *129*, 10320.

(34) Wang, Z.-S.; Cui, Y.; Dan-oh, Y.; Kasada, C.; Shinpo, A.; Hara, K. *The Journal of Physical Chemistry C* **2007**, *111*, 7224.

(35) Bessho, T.; Zakeeruddin, S. M.; Yeh, C.-Y.; Diau, E. W.-G.; Grätzel, M. *Angewandte Chemie International Edition* **2010**, *49*, 6646.

(36) Gao, F. G.; Bard, A. J.; Kispert, L. D. *Journal of Photochemistry and Photobiology A: Chemistry* **2000**, *130*, 49.

(37) École Polytechnique Fédérale de Lausanne: Science Daily, 2 July 2008.

(38) Rossier-Iten, N., École Polytechnique Fédérale de Lausanne, 2006.

(39) Zakeeruddin, S. M.; Grätzel, M. *Advanced Functional Materials* **2009**, *19*, 2187.

(40) Nogueira, A. F.; Longo, C.; De Paoli, M. A. *Coordination Chemistry Reviews* **2004**, *248*, 1455.

(41) Hauch, A.; Georg, A. *Electrochimica Acta* **2001**, *46*, 3457.

(42) Peter, L. *Journal of Electroanalytical Chemistry* **2007**, *599*, 233.

(43) Nelson, J. *Physical Review B* **1999**, *59*, 15374.

(44) Nakade, S.; Saito, Y.; Kubo, W.; Kanzaki, T.; Kitamura, T.; Wada, Y.; Yanagida, S. *Electrochemistry Communications* **2003**, *5*, 804.

(45) Stauffer, D.; Aharony, A. *Introduction of Percolation Theory*; 2nd ed.; Taylor & Francis: London, 1992.

(46) van de Lagemaat, J.; Benkstein, K. D.; Frank, A. J. *The Journal of Physical Chemistry B* **2001**, *105*, 12433.

(47) Gregg, B. A.; Pichot, F.; Ferrere, S.; Fields, C. L. *The Journal of Physical Chemistry B* **2001**, *105*, 1422.

(48) Martinson, A. B. F.; Hamann, T. W.; Pellin, M. J.; Hupp, J. T. *Chemistry – A European Journal* **2008**, *14*, 4458.

(49) Adachi, M.; Murata, Y.; Okada, I.; Yoshikawa, S. *Journal of Electrochemical Society* **2003**, *150*, G488.

(50) Tian, Z. R.; Voigt, J. A.; Liu, J.; McKenzie, B.; Xu, H. *Journal of the American Chemical Society* **2003**, *125*, 12384.

(51) Huynh, W. U.; Dittmer, J. J.; Alivisatos, A. P. *Science* **2002**, *295*, 2425.

(52) Blanford, C. F.; Carter, C. B.; Stein, A. *Journal of Microscopy* **2004**, *216*, 263.

(53) Bisquert, J. *Physical Chemistry Chemical Physics* **2008**, *10*, 49.

(54) Bard, A. J.; Faulkner, L. J. *Electrochemical Methods: Fundamentals and Applications*; 2nd ed.; John Wiley & Sons: New York, 2000.

(55) http://www.cartage.org.lb/en/themes/sciences/Chemistry/Electrochemis/Electro chemical/CyclicVoltammetry/CyclicVoltammetry.htm.

(56) Bisquert, J.; Zaban, A. *Applied Physics A: Materials Science & Processing* **2003**, *77*, 507.

(57) Fabregat-Santiago, F.; Garcia-Belmonte, G.; Bisquert, J.; Zaban, A.; Salvador, P. *The Journal of Physical Chemistry B* **2001**, *106*, 334.

(58) Fabregat-Santiago, F.; Bisquert, J.; Garcia-Belmonte, G.; Boschloo, G.; Hagfeldt, A. *Solar Energy Materials and Solar Cells* **2005**, *87*, 117.

(59) Nakade, S.; Saito, Y.; Kubo, W.; Kitamura, T.; Wada, Y.; Yanagida, S. *The Journal of Physical Chemistry B* **2003**, *107*, 8607.

(60) http://pveducation.org/pvcdrom/solar-cell-operation/short-circuit-current.

(61) Krüger, J., École Polytechnique Fédérale de Lausanne, 2003.

(62) Ponomarev, E. A.; Peter, L. M. *Journal of Electroanalytical Chemistry* **1995**, *397*, 45.

(63) Peter, L. M.; Wijayantha, K. G. U. *Electrochemistry Communications* **1999**, *1*, 576.

(64) Ofir, A.; Dor, S.; Grinis, L.; Zaban, A.; Dittrich, T.; Bisquert, J. *The Journal of Chemical Physics* **2008**, *128*, 064703.

(65) Yum, J.-H.; Baranoff, E.; Wenger, S.; Nazeeruddin, M. K.; Gratzel, M. *Energy & Environmental Science* **2011**, *4*, 842.

(66) Grätzel, M. *Journal of Photochemistry and Photobiology C: Photochemistry Reviews* **2003**, *4*.

(67) Feldt, S. M.; Wang, G.; Boschloo, G.; Hagfeldt, A. *The Journal of Physical Chemistry C* **2011**, *115*, 21500.

(68) Wang, M.; Liu, J.; Cevey-Ha, N.-L.; Moon, S.-J.; Liska, P.; Humphry-Baker, R.; Moser, J.-E.; Grätzel, C.; Wang, P.; Zakeeruddin, S. M.; Grätzel, M. *Nano Today* **2010**, *5*, 169.

(69) Leonard, K. C.; Suyama, W. E.; Anderson, M. A. *Langmuir* **2012**, *28*, 6476.

(70) Lindström, H.; Södergren, S.; Solbrand, A.; Rensmo, H.; Hjelm, J.; Hagfeldt, A.; Lindquist, S.-E. *The Journal of Physical Chemistry B* **1997**, *101*, 7710.

(71) Mihi, A.; Calvo, M. E.; Anta, J. A.; Miguez, H. *The Journal of Physical Chemistry C* **2007**, *112*, 13.

(72) Stein, A. *Microporous and Mesoporous Materials* **2001**, *44-45*, 227.

(73) Velev, O. D.; Kaler, E. W. *Advanced Materials* **2000**, *12*, 531.

(74) Xia, Y.; Gates, B.; Yin, Y.; Lu, Y. *Advanced Materials* **2000**, *12*, 693.

(75) Colvin, V. L. *MRS Bulletin* **2001**, 637.

(76) Meseguer, F.; Blanco, A.; Miguez, H.; Garcia-Santamaria, F.; Ibisate, M.; Lopez, C. *Colloids and Surfaces A: Physicochemical and Engineering Aspects* **2002**, *202*, 281.

(77) Bozhko, S. I.; Chaika, A. N.; Emelchenko, G. A.; Masalov, V. M.; Ionov, A. M.; Gruzintsev, A. N.; Mikhailov, G. M.; Medvedev, B. K. *Applied Surface Science* **2004**, *234*, 93.

(78) Goncalves, M. C.; Bras, J.; Almeida, R. M. *Journal of Sol-Gel Science & Technology* **2007**, *42*, 135.

(79) Waterhouse, G. I. N.; Waterland, M. R. *Polyhedron* **2007**, *26*, 356.

(80) Whitmore, R. L. *British Journal of Applied Physics* **1955**, *6*, 239.

(81) Maude, A. D.; Whitmore, R. L. *British Journal of Applied Physics* **1958**, *9*, 477.

(82) Mayoral, R.; Requena, J.; Moya, J. S.; López, C.; Cintas, A.; Miguez, H.; Meseguer, F.; Vázquez, L.; Holgado, M.; Blanco, A. *Advanced Materials* **1997**, *9*, 257.

(83) Liu, Y.; Wang, S.; Lee, J. W.; Kotov, N. A. *Chemistry of Materials* **2005**, *17*, 4918.

(84) Rogach, A. L.; Kotov, N. A.; Koktysh, D. S.; Ostrander, J. W.; Ragoisha, G. A. *Chemistry of Materials* **2000**, *12*, 2721.

(85) Prevo, B. G.; Velev, O. D. *Langmuir* **2004**, *20*, 2099.

(86) Jiang, P.; Bertone, J. F.; Hwang, K. S.; Colvin, V. L. *Chemistry of Materials* **1999**, *11*, 2132.

(87) Wong, S.; Kitaev, V.; Ozin, G. *Journal of American Chemical Society* **2003**, *125*, 15589.

(88) Hatton, B.; Mishchenko, L.; Davis, S.; Sandhage, K. H.; Aizenberg, J. *PNAS* **2010**, *107*, 10354.

(89) Murray, C. B.; Kagan, C. R.; Bawendi, M. G. *Annual Review of Materials Research* **2000**, *30*, 545.

(90) Scolan, E.; Sanchez, C. *Chemistry of Materials* **1998**, *10*, 3217.

(91) Liu, W.; Zou, B.; Zhao, J.; Cui, H. *Thin Solid Films* **2010**, *518*, 4923.

(92) Imhof, A.; Pine, D. J. *Nature* **1997**, *389*.

(93) Holland, B. T.; Blanford, C. F.; Stein, A. *Science* **1998**, *281*.

(94) Wijnhoven, J. E. G. J.; Vos, W. L. *Science* **1998**, *281*.

(95) Palacios-Lidon, E.; Juárez, B. H.; Castillo-Martinez, E.; Lópex, C. *Journal of Applied Physics* **2005**, *97*, 063502.

(96) Sinitskii, A.; Abramova, V.; Laptinskaya, T.; Tretyakov, Y. D. *Physics Letters A* **2007**, *366*, 516.

(97) Vickreva, O.; Kalinina, O.; Kumacheva, E. *Advanced Materials* **2000**, *12*, 110.

(98) Douglas, D. L.; Birk, J. R. *Annual Review of Energy* **1980**, *5*.

(99) Srinivasan, S.; Mosdale, R.; Stevens, P.; Yang, C. *Annual Review of Energy and Environment* **1999**, *24*.

(100) Kim, J.-H.; Kang, S. H.; Zhu, K.; Kim, J. Y.; Neale, N. R.; Frank, A. J. *Chemical Communications* **2011**, *47*, 5214.

(101) Fabregat-Santiago, F.; Bisquert, J.; Garcia-Belmonte, G.; Boschloo, G.; Hagfeldt, A. *Sol. Energ. Mat. Sol. C.* **2005**, *87*, 117.

(102) Shin, J.-H.; Kang, J.-H.; Jin, W.-M.; Park, J. H.; Cho, Y.-S.; Moon, J. H. *Langmuir* **2010**, *27*, 856.

(103) Swierk, J. R.; Mallouk, T. E. *Chemical Society Reviews* **2013**.

(104) Monllor-Satoca, D.; Lana-Villarreal, T.; Gómez, R. *Langmuir* **2011**, *27*, 15312.

(105) Miyake, M.; Torimoto, T.; Nishizawa, M.; Sakata, T.; Mori, H.; Yoneyama, H. *Langmuir* **1999**, *15*, 2714.

(106) Zaban, A.; Mićić, O. I.; Gregg, B. A.; Nozik, A. J. *Langmuir* **1998**, *14*, 3153.

(107) Halverson, A. F.; Zhu, K.; Erslev, P. T.; Kim, J. Y.; Neale, N. R.; Frank, A. J. *Nano Letters* **2012**, *12*, 2112.

(108) Mathew, S.; Ma, S.; Kretzschmar, I. *Journal of Materials Research* **2013**, *28*, 369.

(109) Benkstein, K. D.; Kopidakis, N.; van de Lagemaat, J.; Frank, A. J. *The Journal of Physical Chemistry B* **2003**, *107*, 7759.

(110) Tomkiewicz, M. *Journal of Electrochemical Society* **1979**, *126*, 1505.

(111) Rothenberger, G.; Fitzmaurice, D.; Grätzel, M. *Journal of Physical Chemistry* **1992**, *96*, 5983.

(112) Bisquert, J. *The Journal of Physical Chemistry B* **2001**, *106*, 325.

(113) Sugimoto, W.; Yokoshima, K.; Murakami, Y.; Takasu, Y. *Electrochimica Acta* **2006**, *52*, 1742.

(114) Chae, W.-S.; Van Gough, D.; Ham, S.-K.; Robinson, D. B.; Braun, P. V. *ACS Applied Materials & Interfaces* **2012**.

(115) Kalyanasundaram, K. *Dye-sensitized solar cells*; CRC PressINC, 2010.

(116) Fujishima, A.; Zhang, X. *Comptes Rendus Chimie* **2006**, *9*, 750.

(117) Alhamed, M.; Issa, A. S.; Doubal, A. W. *Journal of Electron Devices* **2012**, *16*, 1370.

(118) Virtuani, A.; Lotter, E.; Powalla, M. *Solar Energy Materials and Solar Cells* **2006**, *90*, 2141.

(119) Zhu, K.; Kopidakis, N.; Neale, N. R.; van de Lagemaat, J.; Frank, A. J. *The Journal of Physical Chemistry B* **2006**, *110*, 25174.